Interleukin-1 receptor antagonist is a conserved early factor for exacerbating tuberculosis susceptibility

Ophelia V. Lee[1], Daisy X. Ji[2], Bruce A. Rosa[3], David L. Jaye[4], Sara Suliman[5], Makedonka Mitreva[3], Cem Gabay[6], Russell E. Vance[7]*, Dmitri I. Kotov[8]**

[1]Divison of Immunology and Molecular Medicine, University of California, Berkeley, Berkeley, CA, 94720, USA; [2]Department of Microbiology, New York University Grossman School of Medicine, New York, NY, 10016, USA; [3]Division of Infectious Diseases, Department of Medicine, Washington University School of Medicine, St. Louis, MO, 63110, USA; [4]Department of Pathology and Laboratory Medicine, Emory University, Atlanta, GA, 30322, USA; [5]Division of Experimental Medicine, Department of Medicine, University of California, San Francisco, San Francisco, CA, 94115, USA; [6]Division of Rheumatology, Department of Medicine, University Hospital of Geneva, Geneva, Switzerland; [7]Divison of Immunology and Molecular Medicine, Howard Hughes Medical Institute, University of California, Berkeley, Berkeley, CA, 94720, USA; [8]Division of Infectious Diseases, Department of Medicine, Andrew M. and Jane M. Bursky Center for Human Immunology and Immunotherapy Programs, Washington University School of Medicine, St. Louis, MO, 63110, USA.
*Correspondence: kotov@wustl.edu, rvance@berkeley.edu

Lead contact: Requests for further information and resources should be directed to and will be fulfilled by the lead contact, Dmitri I. Kotov (kotov@wustl.edu).

Summary

Mycobacterium tuberculosis (*Mtb*) causes 1.25 million deaths a year. However, tuberculosis (TB) pathogenesis remains poorly understood and is not fully recapitulated in standard mouse models. Here we find that gene signatures from three different *Mtb*-susceptible mouse models predict active TB disease in humans significantly better than a signature from resistant C57BL/6 (B6) mice. Conserved among susceptible mice, non-human primates, and humans, but largely absent from B6 mice, was *Mtb*-induced differentiation of macrophages into an *Spp1*$^{+}$ differentiation state. *Spp1*$^{+}$ macrophages expressed high levels of immunosuppressive molecules including IL-1 receptor antagonist (IL-1Ra). IL-1Ra was previously reported to cause *Mtb* susceptibility in one mouse model, but whether IL-1Ra is broadly important remains uncertain. Here we report that enhancement of IL-1 signaling via deletion of IL-Ra promoted bacterial control across three susceptible mouse models. We found IL-1 signaling amplified production of multiple cytokines by lymphoid and stromal cells, providing a multifactorial mechanism for how IL-1 promotes *Mtb* control. Our results indicate that myeloid cell expression of immunosuppressive molecules, in particular IL-1 receptor antagonist, is a conserved early mechanism limiting *Mtb* control in mice, non-human primates, and humans.

Keywords

Innate immunity, tuberculosis, IL-1 receptor antagonist, neutrophil, macrophage, osteopontin, Spp1.

Introduction

Mycobacterium tuberculosis (*Mtb*) causes ~10 million new cases of active tuberculosis (TB) disease and 1.25 million deaths per year, and is the leading cause of mortality from a bacterial pathogen[1]. Unfortunately, TB treatment consists of at least a 4-6 month regimen of antibiotics,

and the only approved vaccine has little to no efficacy in adults[2]. A greater understanding of the infection is essential, but this depends on tractable animal models that appropriately mimic *Mtb* pathogenesis in humans. While mouse models have led to key discoveries such as the critical role of IFN-γ[3,4] and TNF-α[5] in *Mtb* control, mouse models have also been criticized for not recapitulating key aspects of human disease, such as highly structured granuloma formation[6,7]. Further hallmarks of active tuberculosis (TB) disease in humans include expression of type I interferon (IFN) stimulated genes and a heightened neutrophil response[8,9]. The standard, resistant C57BL/6 (B6) mouse model only weakly exhibits these hallmarks[10–13].

We recently described *Sp140*$^{-/-}$ mice as an *Mtb*-susceptible mouse model that mimics the exacerbated type I IFN signature and heightened neutrophil response seen in humans[14,15]. *Sp140* encodes a transcriptional repressor that limits expression of the canonical type I IFN gene *Ifnb1*[16]. Loss of *Sp140* accounts for the excessive type I IFN response and *Mtb*-susceptibility of the previously described *Sst1*^{S} ("Kramink") mice[17–19]. Deletion of the gene encoding the type I IFN receptor (*Ifnar1*) rescues the hypersusceptibility of both *Sst1*^{S} and *Sp140*$^{-/-}$ mice, implying a causal role of type I IFNs in *Mtb* pathogenesis in these models[14,15]. Other *Mtb* susceptible mouse models have been described, such as *Nos2*$^{-/-}$ and *Acod1*$^{-/-}$ mice[20,21], though it remains unclear whether disease in these models is also driven by type I IFN signaling. Nevertheless, we hypothesized that there may be conserved features underlying the susceptibility of diverse mouse models, and that these features may be preserved across susceptible mice, non-human primates, and humans.

Neutrophilic inflammation is a major feature associated with tuberculosis disease across *Sp140*$^{-/-}$, *Nos2*$^{-/-}$, *Acod1*$^{-/-}$ and other susceptible mouse models[13,15,21–24], as well as during non-human primate[25,26] and human TB[27,28]. Depletion of neutrophils enhances bacterial control in diverse *Mtb*-susceptible mouse models, including *Sp140*$^{-/-}$, *Nos2*$^{-/-}$, and *Acod1*$^{-/-}$ mice[13,15,21]. However, the precise role of neutrophils in driving bacterial replication is unclear. One widely held view is that neutrophil necrosis and inflammation creates a replicative niche for the bacteria, including possibly within neutrophils themselves[29,30]. The production of neutrophil extracellular traps (NETs) is also speculated to promote bacterial replication, perhaps by induction of type I IFNs[15,22,31]. In states of chronic inflammation, neutrophils can also play immunosuppressive roles[32], though it remains uncertain if this accounts for neutrophil-driven exacerbation of TB disease[13,15,21].

Signaling induced by interleukin-1 (IL-1, comprising IL-1α and IL-1β) potently recruits neutrophils to sites of inflammation, and IL-1 is expressed at high levels in *Mtb*-susceptible mice[17,33] and humans[34]. Excessive IL-1 has been proposed to enhance bacterial replication[35], particularly in *Nos2*$^{-/-}$ mice[13,33], though the underlying mechanisms remain uncertain. A pro-bacterial function of IL-1 is difficult to reconcile with its clear anti-bacterial functions, as mice deficient in IL-1 signaling are highly susceptible to *Mtb* infection[23,36–40]. Importantly, the levels of IL-1 do not necessarily correlate with its signaling capacity. This is because IL-1 signaling is repressed by a decoy receptor (IL-1R2) and a soluble receptor antagonist (IL-1Ra, encoded by the *Il1rn* gene). Although susceptible *Sst1*^{S} mice express high levels of IL-1α and IL-1β, we previously reported that deficiency in *Il1rn* (resulting in enhanced IL-1 signaling) markedly promotes bacterial control in these mice[17]. These results imply that *Mtb*-susceptibility can arise from a lack of IL-1 signaling, rather than excessive IL-1 signaling, even when IL-1 levels are high. However, disease in *Sst1*^{S} mice may be a unique case since it is driven by an exacerbated type I IFN response[17], and *Il1rn* is an interferon-stimulated gene. Thus, it remains unclear whether impairment of IL-1 signaling by IL-1Ra plays a conserved role in humans or other *Mtb*-susceptible mouse models, especially *Nos2*$^{-/-}$ and *Acod1*$^{-/-}$ mice, in which *Mtb* infection is characterized by high levels of IL-1.

Here, in an effort to identify conserved mechanisms underlying *Mtb* susceptibility, we used single cell RNA sequencing (scRNA-seq) to profile and characterize three different *Mtb*-susceptible mouse strains (*Sp140*$^{-/-}$, *Nos2*$^{-/-}$, *Acod1*$^{-/-}$ mice). Unlike *Sp140*$^{-/-}$ mice, we found

that *Nos2*$^{-/-}$ and *Acod1*$^{-/-}$ mice did not exhibit a strong type I IFN signature and were not rescued by *Ifnar1* deficiency. Despite this, a common feature of *Mtb*-induced genes across all three strains was myeloid cell expression of immunosuppressive genes, such as *Arg1*, *Cd274*, and *Il18bp* (*Il1rn* is not in the *Mtb*-induced gene signatures because neutrophils were included in the naïve lung dataset and constitutively express *Il1rn*). In support of the importance of shared features of the *Mtb*-susceptible strains, gene signatures from each of these strains predicted human TB progression better than a signature obtained from resistant B6 mice. Additionally, macrophage differentiation into an *Spp1*$^{+}$ state was conserved across the susceptible mouse strains, *Mtb*-infected non-human primates, and *Mtb*-infected humans. Mouse, non-human primate, and human *Spp1*$^{+}$ macrophages expressed immunosuppressive molecules, including *Il1rn*. Given the importance of IL-1 signaling for *Mtb* control, and the strong expression of IL-1Ra in myeloid cells, we focused on the role of IL-1Ra in *Mtb* susceptibility. Global deletion as well as myeloid-specific deletion of IL-1Ra rescued bacterial control in *Sp140*$^{-/-}$ mice, demonstrating a major role for macrophage expression of this immunosuppressive molecule in driving *Mtb* disease. This contribution was shared across the susceptible mouse models, as global IL-1Ra deletion also enhanced bacterial control in *Nos2*$^{-/-}$ and *Acod1*$^{-/-}$ mice while neutrophil-specific IL-1Ra deletion did not, in line with macrophages being the dominant source of IL-1Ra during *Mtb* infection. Although *IL1RN* has been included in multiple human TB gene signatures[8,41–43], we find it alone was sufficient to strongly predict human TB and was induced early in the human response to TB with elevated levels detectable ~200 days prior to TB diagnosis. Together, these data suggest that immunosuppression by myeloid cells is a conserved feature of *Mtb* susceptibility across mice and humans, with some immunosuppressive pathways, such as IL-1 inhibition via IL-1Ra, being a shared early mechanism aggravating TB.

Results

Mtb-susceptible mice more accurately model human infection than B6 mice

Human *Mtb* infection presents as a highly diverse spectrum of diseased and non-diseased states. The best characterized hallmarks of active disease include induction of type I interferon (IFN) genes and a myeloid cell inflammatory response, especially by neutrophils[8]. We previously demonstrated that *Sp140*$^{-/-}$ mice exhibit both hallmarks, and that these hallmarks drive susceptibility in these mice[14,15]. Neutrophil trafficking to the lungs also promotes *Mtb* susceptibility in other mouse models[22,44–46], including *Nos2*$^{-/-}$ and *Acod1*$^{-/-}$ mice[13,21]. We sought to explore the use of different susceptible mouse models as a way to mimic the diversity of human TB disease. To start, we characterized the myeloid cell response in *Sp140*$^{-/-}$, *Nos2*$^{-/-}$, and *Acod1*$^{-/-}$ mice. We focused on ~4 weeks post-infection since it was an early timepoint where there were clear differences between resistant and susceptible strains. Although there are also major differences between strains at later timepoints, our rationale was to focus on earlier events to try to identify more proximal causes of susceptibility rather than indirect downstream consequences.

In line with previous reports, we observed a ~5-fold increase in lung neutrophils and a ~2-4-fold increase in lung monocytes and interstitial macrophages (IMs) in *Mtb*-susceptible mice 25 days after *Mtb* infection in each of the three mouse models (**Fig. 1A**). We sought to explore myeloid function in promoting *Mtb* susceptibility by first examining myeloid cell trafficking in *Mtb*-infected lungs from B6 and *Sp140*$^{-/-}$ mice (**Fig. 1B**). Diseased tissue within the lung was defined by the presence of *Mtb* and high cellularity. These features were largely absent from healthy portions of the lung. Diseased areas of the lungs had more macrophages (SIRPα^{+} cells) and neutrophils (Ly6G^{+} cells) than the healthy tissue of the same lungs (**Fig. 1C**). To confirm that this enrichment was not unique to *Sp140*$^{-/-}$ mice, we also compared macrophage and neutrophil

154 trafficking in B6, *Nos2*$^{-/-}$, and *Acod1*$^{-/-}$ mice (**Fig. 1D**). Similar to *Sp140*$^{-/-}$ mice, neutrophils
155 were significantly enriched, and macrophages trended toward greater numbers in diseased
156 relative to healthy tissue in all tested genotypes (**Fig. 1E**). Interestingly, while similar numbers of
157 macrophages and neutrophils were recruited to the diseased portions of susceptible mouse
158 lungs, macrophages were significantly closer to *Mtb* in B6, *Sp140*$^{-/-}$, *Nos2*$^{-/-}$, and *Acod1*$^{-/-}$ mice,
159 as compared to neutrophils, which were more spatially segregated from *Mtb* (**Fig. 1F**). These
160 data indicate that myeloid cells are more abundant in *Mtb*-infected lungs and preferentially traffic
161 to sites of disease within those lungs, with macrophages residing closer to *Mtb* within the
162 infected lung tissue.
163 As the heightened myeloid response was conserved across the *Mtb*-susceptible mouse
164 models, we sought to test whether *Nos2*$^{-/-}$ and *Acod1*$^{-/-}$ mice share other attributes of the
165 susceptibility of *Sp140*$^{-/-}$ mice, including type I IFN-driven disease. As myeloid cells are the
166 primary reservoir of *Mtb*, we used our previously described single cell RNA-sequencing (scRNA-
167 seq) workflow[15] to profile myeloid cells in *Mtb*-infected and naïve *Nos2*$^{-/-}$ and *Acod1*$^{-/-}$ mice.
168 Infection with a fluorescent (wasabi^{+}) *Mtb* strain allowed us to distinguish infected and bystander
169 cells in infected mice. The resulting datasets were integrated with our previously published B6
170 and *Sp140*$^{-/-}$ myeloid cell datasets[15] using the R package Seurat[47] (**Fig. 2A**). B6 mice were
171 used as a control rather than *Sp140*$^{-/-}$ *Ifnar1*$^{-/-}$ mice because we previously demonstrated there
172 is no difference in bacterial burden between these two genotypes 25 days post-infection (the
173 timepoint of the scRNA-seq experiment)[14]. As these are CITE-seq[48] datasets, mRNA and
174 protein expression of lineage and activation markers were implemented for the annotation of cell
175 clusters (**Supplementary Fig. 1**). Comparing the myeloid cells from naïve lungs of B6, *Sp140*$^{-/-}$,
176 *Nos2*$^{-/-}$, and *Acod1*$^{-/-}$ mice revealed very few differentially expressed genes between the mouse
177 lines, suggesting that each genotype had a similar inflammatory state prior to infection
178 (**Supplementary Fig. 1**). Therefore, differences between genotypes in *Mtb*-infected mice were
179 likely induced in response to the infection rather than the result of pre-existing inflammation.
180 Analysis of the myeloid cell clusters within the integrated dataset showed that the dominant
181 myeloid cell populations (monocytes, macrophages, and neutrophils) are present in each
182 genotype.
183 Given that the increase in neutrophils exhibited by *Mtb*-susceptible mouse models is a
184 hallmark of human *Mtb* disease progression[27], we hypothesized that susceptible mouse models
185 might mimic additional conserved hallmarks of active human disease, in which case they could
186 be a useful tool to study *Mtb* pathogenesis. To test this hypothesis, we identified lung myeloid
187 gene signatures consisting of genes induced at least 8-fold in *Mtb*-infected susceptible mice
188 relative to naïve lungs (**Supplementary Figure 2**). The ability of these genes to discriminate
189 *Mtb* cases from healthy controls in the TANDEM cohort[49] was quantified by calculating the area
190 under the curve (AUC) for receiver operating characteristic (ROC) curves, with values closer to
191 1 indicating better classifiers of human disease (**Fig. 1B**). While there was no major difference
192 in the ability of the signatures derived from the three susceptible mouse models to discern
193 human disease, all the susceptible models considerably out-performed the signature derived
194 from B6 mice, suggesting the susceptible mouse models better recapitulate characteristics of
195 active human disease than B6 mice. We also tested the ability of these signatures to
196 discriminate between active TB and latent TB-infected (LTBI) individuals in the Berry South
197 Africa cohort[50], and similarly observed that the three susceptible mouse model signatures out-
198 performed the B6 mouse signature, in line with the hypothesis that susceptible mouse models
199 better recapitulate active human disease (**Fig. 1B**). The goal of this analysis was just to
200 compare the immune response between mouse and human *Mtb* infection and was not to
201 identify potential biomarkers of human *Mtb* infection. However, we also observed that the
202 mouse signatures discriminated active TB infection from lung cancer and pneumonia in the
203 Bloom et al. cohort[51], suggesting the similarity in immune responses between mice and humans

204 captured by these gene signatures does not solely reflect general inflammation
205 (**Supplementary Figure 2**).
206 Next, we sought to better understand why the susceptible models were all able to
207 discriminate between *Mtb* cases and healthy controls by assessing whether the type I IFN
208 response present in humans[8] and *Sp140*$^{-/-}$ mice[14,15] was also present in *Nos2*$^{-/-}$ and *Acod1*$^{-/-}$
209 animals. Using our previously published gene signatures that distinguish between type I IFN
210 and IFN-γ signaling[15], we classified cells as responding to type I IFN and/or IFN-γ in our myeloid
211 scRNA-seq dataset. As expected, very few cells from naïve lungs were positive for either the
212 type I or II IFN signature (**Fig. 2C**). Conversely, at least some *Mtb*-infected cells from every
213 genotype had strong IFN-γ signaling, especially in monocytes and macrophages (**Fig. 2C, 2D**).
214 However, the type I IFN response was notable only in the *Sp140*$^{-/-}$ mice, with strong type I IFN
215 signaling in the neutrophils and interstitial macrophages (IMs) of these mice.
216 We experimentally tested whether type I IFN signaling plays a causative role in disease
217 progression in each *Mtb*-susceptible mouse model by examining lung bacterial burden in *Ifnar1*-
218 deficient *Sp140*$^{-/-}$, *Nos2*$^{-/-}$, and *Acod1*$^{-/-}$ mice 25 days after *Mtb* infection. As reported
219 previously, global *Ifnar1*-deficiency fully rescued the susceptibility of *Sp140*$^{-/-}$ mice,
220 phenocopying the *Mtb* restriction of B6 mice[14,15]; however, *Ifnar1*-deficiency only slightly
221 reduced bacterial burdens in *Acod1*$^{-/-}$ mice and even modestly but not statistically significantly
222 increased bacterial burdens in *Nos2*$^{-/-}$ mice (**Fig. 2E, 2F, 2G**). Together, these data suggest that
223 while all three models recapitulate key aspects of human disease, there are major differences in
224 the drivers of susceptibility between these mouse models.
225
226 *Myeloid cell production of IL-1Ra is a conserved hallmark of Mtb susceptibility*
227
228 As a strong type I IFN response was not shared among the three *Mtb*-susceptible mouse
229 models, we analyzed our scRNA-seq to identify common features that may contribute to the
230 elevated bacterial burdens present in these animals. We observed that *Mtb*-infection resulted in
231 activation of the IMs, driving them to adopt either a proinflammatory *Trem2*$^{+}$ or an alternative
232 *Spp1*$^{+}$ activation state[52–54] (**Fig. 3A, 3B**). A shift to *Spp1*$^{+}$ macrophage differentiation was
233 recently associated with human tumor progression[54] and elevated plasma SPP1 levels correlate
234 with active TB disease in humans[55]. Additionally, SPP1^{+} macrophages were present at an
235 elevated frequency in bronchial alveolar lavage fluid from TB patients relative to LTBI individuals
236 and healthy controls[56], and SPP1^{+} macrophages have been identified around granulomas in
237 human lungs[57]. We therefore examined whether *Spp1*$^{+}$ macrophage differentiation correlated
238 with *Mtb* susceptibility. Indeed, *Spp1*$^{+}$ macrophages were the dominant monocyte-derived
239 macrophage population in the *Mtb*-susceptible *Sp140*$^{-/-}$, *Nos2*$^{-/-}$, and *Acod1*$^{-/-}$ mice, while being
240 largely absent in *Mtb*-restrictive B6 mice (**Fig. 3C, 3D**). The *Spp1*$^{+}$ state was distinguished from
241 the *Trem2*$^{+}$ state by the elevated expression of immunosuppressive molecules, including *Il1rn*
242 (encoding IL-1Ra) which we previously demonstrated contributes to loss of bacterial control in
243 *Mtb*-susceptible *Sst1*^{S} mice[17] (**Fig. 3E**). Alongside neutrophils, which constitutively express
244 *Il1rn*[58], *Spp1*$^{+}$ IMs were the dominant source of *Il1rn* among myeloid cells and *Spp1*$^{+}$ IM *Il1rn*
245 expression was elevated in all three susceptible strains relative to B6 mice (**Fig. 3F**).
246 Reanalysis, including re-annotation, of a published scRNA-seq dataset of non-human primate
247 *Mtb* granulomas indicated this expression pattern was conserved across species[59]
248 (**Supplementary Figure 3**). SPP1^{+} macrophages were present in non-human primate *Mtb*
249 granulomas, and the SPP1^{+} macrophages had higher expression levels of immunosuppressive
250 molecules such as IDO1, CD274, IL18BP, and IL1RN than TREM2^{+} macrophages (**Fig. 3F,**
251 **3G**). Reanalysis and re-annotation of a scRNA-seq dataset of resected lungs from *Mtb*-infected
252 humans also identified SPP1^{+} IMs with elevated expression of immunosuppressive molecules
253 relative to TREM2^{+} IMs, including increased expression of IDO1, TGFβ, IL-10, IL-27, CD274,
254 IL1RN, and the IL-1 decoy receptor IL1R2 (**Fig. 3I, 3J**). Additionally, SPP1^{+} IMs were a

255 dominant source of IL1RN among myeloid cells in the human lungs with the IL1RN-expressing
256 SPP1$^+$ IMs present in metabolically active (FDG high signal) and metabolically inactive (FDG
257 low signal) portions of *Mtb*-infected human lungs (**Fig. 3K**). Further examining the conserved
258 nature of *Spp1*$^+$ macrophages, we identified a core *Spp1*$^+$ gene signature consisting of genes
259 upregulated in *Spp1*$^+$ relative to *Trem2*$^+$ IMs in the three susceptible mouse models as well as in
260 human *Mtb*-infected lungs. This core signature includes *IL1RN,* highlighting the strong
261 association between *Spp1*$^+$ IM differentiation and *IL1RN* expression across species
262 (**Supplementary Figure 4**).
263 Given the conserved nature of IL-1Ra expression, we tested whether *IL1RN* expression
264 could discriminate between active *Mtb* cases and healthy controls in RNA-seq of PBMCs from
265 the TANDEM cohort[49]. We observed high sensitivity and specificity for *IL1RN* alone (AUC=0.84)
266 (**Fig. 3I**), which was only slightly improved by including *IL1RN* in a gene signature containing
267 additional known immunosuppressive molecules, such as *IL18BP*[60], *CD274*[61], and *IL10*[62]
268 (**Supplementary Fig. 5**). *IL1RN* alone was also highly discriminatory when discerning active TB
269 versus LTBI cases when applied to the Berry South Africa dataset[50] (AUC=0.869; **Fig. 3M**). The
270 high performance of *IL1RN* is consistent with prior work, as multiple published human TB
271 signatures include *IL1RN*[8,41–43]. Analysis of *IL1RN* expression in the progressor population of
272 the Adolescent Cohort Study[63] identified that increased *IL1RN* expression was detectable ~200
273 days before clinical TB diagnosis, in line with our hypothesis that IL-1Ra is an early mechanism
274 of disease exacerbation (**Supplementary Fig. 5**). It is important to note that IFN response was
275 the earliest detected transcriptional change in the Adolescent Cohort Study (observed ~12-18
276 months before diagnosis)[64], suggesting that other factors initiate loss of bacterial control which
277 may then be amplified by immunosuppressive molecules including IL-1Ra. As IL-1 signaling is
278 regulated by both IL-1Ra and the decoy IL-1R2 receptor, we also examined *Il1r2* expression in
279 our scRNA-seq datasets and found lower *Il1r2* expression in *Mtb*-infected animals relative to
280 naïve controls, suggesting *Il1r2* does not contribute to *Mtb* susceptibility (**Supplementary Fig.
281 5**). Taken together, our results indicate that myeloid cell expression of IL-1Ra is an important
282 hallmark of early TB disease that is conserved across mice, non-human primates, and humans.
283
284 *Spp1*$^+$ *IM differentiation is unrelated to the M1 vs M2 macrophage differentiation paradigm*
285
286 Given the strong correlation between *Spp1*$^+$ macrophage differentiation, IL-1Ra expression, and
287 *Mtb* disease progression, we sought to further examine the *Spp1*$^+$ IM response to *Mtb* infection,
288 particularly in the case of the *Mtb*-susceptible *Sp140*$^{-/-}$, *Nos2*$^{-/-}$, and *Acod1*$^{-/-}$ mice. Our myeloid
289 cell scRNA-seq dataset was used to determine potential markers for flow cytometric
290 identification of *Spp1*$^+$ IMs and *Trem2*$^+$ IMs in infected mice. We found that *Itgax* (encoding
291 CD11c) was upregulated on mature IMs, *Cd63* was preferentially expressed on *Trem2*$^+$ IMs,
292 and *Cd9* was preferentially expressed by *Spp1*$^+$ IMs and was part of the core mouse *Spp1*$^+$
293 signature (**Fig. 4A, Supplementary Figure 4**). CD166, also known as Alcam, was recently
294 identified as a marker of human *SPP1*$^+$ lung macrophages[65], while Trem2 and C1q are
295 preferentially expressed by *TREM2*$^+$ lung macrophages in mice, non-human primates, and
296 humans by scRNA-seq (**Fig. 3E, 3H, 3J**). Using a gating strategy to distinguish IMs from AMs,
297 we then gated on the mature PD-L1^{hi} CD11c^{hi} IMs and used CD9 and CD63 as markers for
298 *Spp1*$^+$ and *Trem2*$^+$ IMs, respectively (**Fig. 4B, Supplementary Figure 6**). CD9 and CD63 were
299 validated as markers for these macrophage populations by assessing their staining for Alcam,
300 Trem2, and C1q. As predicted, the CD9^{hi} *Spp1*$^+$ IMs stained brighter for Alcam while the CD63^{hi}
301 *Trem2*$^+$ IMs stained brighter for Trem2 and C1q (**Fig. 4C**). We next assessed how *Mtb*-
302 susceptibility impacts macrophage differentiation by comparing differentiation in B6, *Sp140*$^{-/-}$,
303 *Nos2*$^{-/-}$, and *Acod1*$^{-/-}$ mice. Interestingly, all three susceptible mouse models displayed
304 significant reductions in the frequency of mature IMs relative to B6 control mice, in line with the
305 elevated monocyte recruitment observed in these animals following *Mtb* infection (**Fig. 1A, 4D**).

Of the mature IMs, there was a significant increase in *Spp1*$^{+}$ macrophage frequency in all three susceptible models, while *Trem2*$^{+}$ macrophage differentiation was reduced in *Nos2*$^{-/-}$ and *Acod1*$^{-/-}$ mice (**Fig. 4E, 4F**). These findings validate the scRNA-seq data and confirm that a shift from *Trem2*$^{+}$ to *Spp1*$^{+}$ IM differentiation correlates with loss of bacterial control (**Fig. 3D**).

As all three of the *Mtb*-susceptible mouse strains have increased bacterial burdens (**Fig. 2E, 2F, 2G**), we next asked whether *Mtb* infection directly drove *Spp1*$^{+}$ IM differentiation. Harboring *Mtb* correlated with an increase in *Spp1*$^{+}$ and *Trem2*$^{+}$ IMs by scRNA-seq and both populations exhibited higher rates of infection by flow cytometry when comparing *Sp140*$^{-/-}$ to B6 mice (**Fig. 4G, 4H**). However, the *Trem2*$^{+}$ IM were infected at a greater frequency than the *Spp1*$^{+}$ IM in B6 and *Sp140*$^{-/-}$ mice. Additionally, most cells of either IM subset were uninfected, suggesting direct infection is not a major driver of *Spp1*$^{+}$ IM differentiation. As differentiation into an M1 polarized state, marked by iNOS expression, or an M2 polarized state, marked by Arginase-1 (encoded by *Arg1*) expression, is a traditional view of macrophage differentiation, we tested whether *Trem2*$^{+}$ vs *Spp1*$^{+}$ differentiation mapped onto the M1 vs M2 paradigm. While Arg1 expression was largely restricted to the susceptible mouse models, iNOS and Arg1 were expressed by mature IMs, *Trem2*$^{+}$ IMs, and *Spp1*$^{+}$ IMs by scRNA-seq and flow cytometry demonstrating that *Trem2*$^{+}$ vs *Spp1*$^{+}$ differentiation is independent of canonical M1 vs M2 differentiation (**Fig. 4I, 4J**).

IL-1Ra is a conserved mediator of Mtb susceptibility

Next, we examined whether myeloid cell IL-1Ra expression plays a conserved role in amplifying *Mtb* disease. IL-1 is highly expressed in susceptible mouse strains[33], and has been hypothesized to contribute to the susceptibility of *Nos2*$^{-/-}$ mice to *Mtb*[13,33]. However, as we detected high levels of *Il1rn* expression in myeloid cells in *Sp140*$^{-/-}$, *Nos2*$^{-/-}$, and *Acod1*$^{-/-}$ mice, we hypothesized that perhaps IL-1 signaling was impaired in these mice despite the high levels of IL-1 cytokine. We hypothesized that perhaps the susceptibility of the mice was due to a functional deficiency in IL-1 signaling. In support of the inhibitory role of *Il1rn* during *Mtb* infection, global deletion of *Il1rn* in B6 mice slightly reduced lung bacterial burden (**Fig. 5A**). Neutrophils are major producers of *Il1rn* (**Fig. 3F**); however, neutrophils were not an obligatory source of *Il1rn*, as neutrophil-specific deletion of *Il1rn* using Mrp8^{Cre} *Il1rn*$^{fl/fl}$ mice had no effect on bacterial burden on the B6 genetic background (**Fig. 5B**).

We previously found that *Mtb*-infected *Sst1*^{S} mice exhibit high levels of IL-1 and yet bacterial burdens in these mice are rescued by enhancement of IL-1 signaling via deletion of *Il1rn*[17]. Likewise, we found that even heterozygous deficiency in *Il1rn* promotes bacterial control in *Sp140*$^{-/-}$ mice (**Fig. 5C**). However, as noted above (**Fig. 2**), *Sp140*$^{-/-}$ and *Sst1*^{S} mice exhibit a strong type I IFN signature that is largely absent from *Nos2*$^{-/-}$ and *Acod1*$^{-/-}$ mice. It was therefore of interest to test whether *Il1rn*-deficiency could also rescue bacterial burdens in *Nos2*$^{-/-}$ and *Acod1*$^{-/-}$ mice. We found that while deletion of one allele of *Il1rn* had no effect on *Mtb* control in *Acod1*$^{-/-}$ mice, complete deletion of *Il1rn* was sufficient to restore wild-type levels of bacterial control at day 25 post-infection (**Fig. 5D**). Interestingly, while bacterial burdens were reduced in *Acod1*$^{-/-}$ *Il1rn*$^{-/-}$ mice to levels seen in WT B6 mice, lung neutrophil numbers were still elevated in *Acod1*$^{-/-}$ *Il1rn*$^{-/-}$ mice (**Fig. 5E**). This result suggests that production of IL-Ra may be an important mechanism by which neutrophils drive *Mtb* susceptibility. However, neutrophil-specific deletion of *Il1rn* in *Acod1*$^{-/-}$ mice only slightly improved bacterial restriction, suggesting that while neutrophils may be a source of *Il1rn* during *Mtb* infection, they may not be the sole or dominant source (**Fig. 5F**). In two experiments with a higher and lower dose of *Mtb* inoculum, we also observed partial or complete rescue of bacterial burdens in *Nos2*$^{-/-}$ *Il1rn*$^{-/-}$ mice as compared to *Nos2*$^{-/-}$ mice (**Fig. 5G**). Similar to the *Acod1*$^{-/-}$ mice, no effect of *Ilr1rn* heterozygosity was observed, and the improved bacterial control in *Nos2*$^{-/-}$ *Il1rn*$^{-/-}$ mice did not coincide with a decrease in the number of lung neutrophils (**Fig. 5H**). Despite the increase in

357 neutrophils, neutrophil expression of *Il1rn* did not seem to be a major driver of the *Mtb*
358 susceptibility for *Nos2*$^{-/-}$ mice, as neutrophil-specific deletion of *Il1rn* had no effect on bacterial
359 control in these mice (**Fig. 5I**). These results demonstrate a conserved role for IL-1Ra in
360 elevating *Mtb* burdens in three different mouse models at early infection timepoints, but do not
361 rule out additional roles for IL-1Ra in suppressing immunopathology at later timepoints during
362 TB (see Discussion).
363 The limited role for neutrophil production of IL-1Ra in the *Acod1*$^{-/-}$ and *Nos2*$^{-/-}$ mice is in
364 line with prior reports which suggested that the secretion of IL-1Ra by neutrophils is relatively
365 inefficient as compared to macrophages, and specific deletion of IL-1Ra in macrophages is
366 protective during *Candida* infection[66]. Moreover, neutrophil expression of IL-1Ra is constitutive
367 (including in resistant B6 mice) whereas it is induced in IMs (**Supplementary Figure 5**). Indeed,
368 *Spp1*$^{+}$ IMs exhibited the highest expression levels of *Il1rn* among monocytes and macrophages
369 and *Spp1*$^{+}$ IMs in all three susceptible mouse models expressed elevated levels of *Il1rn* relative
370 to wild-type B6 controls (**Fig. 3F**). Additionally, macrophages localize closer to *Mtb* than
371 neutrophils in all three susceptible mouse models (**Fig. 1F**). We therefore hypothesized that
372 macrophage production of IL-1Ra could account for the conserved role of IL-1Ra in inhibiting
373 bacterial control in *Mtb*-susceptible mice. To delete *Il1rn* in macrophages, we used CD64-Cre
374 mice, which express Cre specifically in macrophages, at least in naïve animals[67]. Deletion of
375 *Il1rn* in CD64^{Cre}*Il1rn*$^{fl/fl}$ mice[67,68] was able to rescue *Mtb* susceptibility of *Sp140*$^{-/-}$ mice (**Fig. 4F**).
376 Together, these data reveal a conserved, myeloid cell role for IL-1Ra expression in
377 exacerbating *Mtb* disease.
378
379 *IL-1-enhanced cytokine and chemokine production promotes Mtb control*
380
381 Given the conserved role for IL-1Ra in exacerbating early *Mtb* infection, we aimed to better
382 define how IL-1 mediates protection against *Mtb*. We first examined IL-1R expression on
383 myeloid cells, as they are the primary reservoir of *Mtb*, and found little to no expression of IL-1R
384 in myeloid cells from naïve and *Mtb*-infected B6, *Sp140*$^{-/-}$, *Nos2*$^{-/-}$, and *Acod1*$^{-/-}$ mice
385 (**Supplementary Fig. 7**). Consistent with a previous study[23], we also demonstrated that IL-1R-
386 deficient macrophages do not exhibit a cell-intrinsic defect in bacterial control in mixed bone
387 marrow (BM) chimera mice (**Supplementary Fig. 7**). It thus appears that IL-1 mediates its
388 protective effect by signaling in bystander cells that then act non-cell autonomously to promote
389 myeloid cell *Mtb* control. We therefore sought to identify the bystander cells that express IL-1R
390 and the genes regulated by IL-1 in these cells to determine the mechanism by which IL-1 aids in
391 bacterial restriction.
392 As IL-1 signaling in either hematopoietic or non-hematopoietic cells is sufficient for *Mtb*
393 control early in infection[23,39], we sought to identify potential IL-1 responders in both
394 compartments. Due to the inhibition of IL-1 signaling by high expression of IL-1Ra in the *Mtb*-
395 susceptible mouse models, we used resistant B6 mice for examining IL-1 function. To ascertain
396 the cell autonomous effects of IL-1, we generated mixed BM chimera mice with a 1:1 mix of WT
397 and *Il1r1*$^{-/-}$ cells that were infected with *Mtb* following immune reconstitution (**Fig. 6A**). Among
398 hematopoietic cells, IL-1 promotes cytokine expression in CD4^{+} T cells[69] and innate lymphoid
399 cells (ILCs)[70,71]. In T cells, *Il1r1* was primarily expressed in T helper 17 cells (Th17) with some
400 expression in Type 1 helper cells (Th1; **Fig. 6B, 6C, Supplementary Fig. 8**). Differential
401 scRNA-seq gene expression profiling comparing WT and *Il1r1*$^{-/-}$ Th17 cells identified *Tnf*,
402 *Gzmb*, and *Ifng* as genes with at least 2-fold greater expression in WT cells that were annotated
403 as potential ligands in the NicheNet database[72] (**Fig. 6D**). Type 3 ILC (ILC3) and IL-17
404 producing natural killer T (NKT17) cells were the major *Il1r1*-expressing innate lymphoid cell
405 populations in *Mtb*-infected lungs, with differential gene expression analysis identifying *Aimp1*
406 and *Cxcl2* as potential IL-1-induced ligands produced by ILC3s; and *Tnf*, *Cxcl10*, *Itgb2*, *Il17a*,

Cxcl2, and *Rtn4* as potential IL-1-induced ligands produced by NKT17 cells (**Fig. 6E, 6F, 6G, Supplementary Fig. 8**).

Regarding potential non-hematopoietic sensors of IL-1, we first examined sensory neurons as they highly express IL-1R[73], and IL-1 signaling in neurons recruits myeloid cells[74]. As IL-1 signaling in hematopoietic cells is sufficient for early resistance to *Mtb* infection[23,39], we generated BM chimera mice that lacked hematopoietic IL-1R and either had IL-1 receptor in sensory neurons (CD45.1 and Adv$^{+/+}$ *Il1r1*$^{fl/fl}$ recipient mice) or not (Adv$^{cre/+}$ *Il1r1*$^{fl/fl}$ recipient mice). Sensory neuron-specific deletion of *Il1r1* had no effect on *Mtb* control, suggesting that other non-hematopoietic cells mediate the protective effect of IL-1 against *Mtb* (**Supplementary Fig. 7**). We thus performed scRNA-seq on BM chimera mice generated by transferring WT BM into lethally irradiated WT and *Il1r1*$^{-/-}$ hosts and then infected the chimeric mice with *Mtb* following immune reconstitution (**Fig. 6H**). Lineage markers used to annotate a scRNA-seq dataset of stromal cells in normal and hyperoxia-damaged murine lungs[75] were used to identify cell populations in our stromal cell scRNA-seq dataset (**Supplementary Fig. 8**). Based on this analysis, *Il1r1* was widely expressed in stromal cells, including in myofibroblasts, fibroblasts, and endothelial cells (**Fig. 6I, 6J**). Differential expression analysis of IL-1-regulated potential ligands, as annotated in NicheNet's database[72], identified *Icam1*, *Il6*, *Ccl2*, and *Wnt11* in myofibroblasts, *Cxcl1*, *Ccl2*, *Il6*, and *Cxcl9* in fibroblasts, and *Icam1* in endothelial cells as IL-1-induced potential ligands (**Fig. 6K**).

The most likely candidates for the protective effect of IL-1 signaling were then identified using NicheNet[72]. For this analysis, we focused on IMs as the receiver cells for the IL-1-regulated ligands, as IMs are known to harbor *Mtb* and control the infection[76]. According to the NicheNet ligand-receptor database, the receptors for IFN-γ, TNF, IL-6, CCL2, and IL-17 were expressed by IMs (**Supplementary Fig. 9**). While IFN-γ and TNF have well-established roles in *Mtb* control[3–5], the contribution of IL-17 has been appreciated more recently[77–80]. IL-22 is another cytokine important for bacterial control that is often co-produced with IL-17[81]. Thus, we tested whether IL-1-induced enhancement of IL-17/22 production was important in IL-1-mediated *Mtb* restriction. This hypothesis was tested by generating mixed BM chimera mice containing BM from *Il17*$^{-/-}$ *Il22*$^{-/-}$ and *Il1r1*$^{-/-}$ mice mixed at a 1:1 ratio as well as control mice (**Fig. 6L**). While the *Il17*$^{-/-}$ *Il22*$^{-/-}$: *Il1r1*$^{-/-}$ BM chimera mice contain cells that can respond to IL-1, as well as cells that can produce IL-17/22, no cell will be able to respond to IL-1 and express IL-17/22. Thus, these chimeras specifically eliminate the ability of IL-1 to amplify IL-17/22 production. The *Il17*$^{-/-}$ *Il22*$^{-/-}$: *Il1r1*$^{-/-}$ BM chimera mice were only slightly more susceptible than control animals, suggesting that an IL-1-mediated increase in IL-17/22 expression is not necessary for IL-1-driven protection (**Fig. 6M**). Therefore, we sought to identify which other potential ligands were the most likely drivers of IL-1-regulated *Mtb* restriction by IMs. We identified genes upregulated in activated IMs, and NicheNet[72] was then used to calculate the likelihood for each of the potential ligands to induce the transcriptional changes observed in the activated IMs. IFN-γ and TNF had the highest scores indicating they are the most likely candidates for how IL-1 protects against *Mtb*, while IL-17 had one of the lowest scores, in line with our experimental data (**Supplementary Fig. 9, Fig. 6M**). Taken together, these results suggest that IL-1-mediated protection against *Mtb* is multifactorial, involving responses by both hematopoietic and stromal cells that coordinate the activation of IMs by multiple anti-microbial cytokines.

Discussion

Mtb infection induces a chronic inflammatory state as evidenced by the induction of a type I/II IFN gene signature up to 12-18 months prior to disease diagnosis[27,64]. While aspects of this

457 inflammatory state—such as the IFN-γ response[3,4]—are vital for bacterial control, other
458 components, such as the type I IFN response, exacerbate *Mtb* disease progression[8,15,22]. Our
459 results lead us to hypothesize that the chronic inflammatory nature of *Mtb* infection may hinder
460 bacterial control by promoting immunosuppression. We further propose that an underlying state
461 of immunosuppression is conserved across susceptible mouse models, non-human primates
462 and in humans. Within the cancer field, it has long been recognized that chronic inflammation
463 supports cancer progression[82] with one major mechanism being the recruitment of so-called
464 myeloid-derived suppressor cells (MDSC)[83]. MDSCs have also been proposed to exacerbate
465 *Mtb* infection[22,84–87]. MDSCs are a heterogeneous population in mice and humans, with mouse
466 MDSCs commonly identified based on Gr-1 antibody staining, which binds Ly6C and L6G,
467 markers of monocytes and neutrophils, respectively[83]. While monocytes and neutrophils are
468 commonly viewed as proinflammatory cells, MDSCs are immunosuppressive through multiple
469 pathways, including via production of IL-10 and TGF-β[88]. During *Mtb* infection, monocytes and
470 neutrophils are also heavily recruited to the lungs and specifically to sites of bacterial replication
471 (**Fig. 1**).
472 In line with these findings, prior studies have described increased MDSCs in the blood of
473 *Mtb*-infected individuals at frequencies similar to those found in human cancer patients[89] as well
474 as increased lung MDSC frequency in non-human primates with active TB disease relative to
475 latently infected animals[90]. Multiple pathways have been proposed for MDSC-driven
476 immunosuppression of the host response against *Mtb* infection, including PD-1, IDO1, TGFβ,
477 and IL-10[91,92]. For example, IDO1^{+} PD-L1^{+} myeloid cells reside in human granulomas and PD-
478 L1 expression associates with active TB progression in humans[93]. However, the impact of
479 immune suppression by myeloid cells on *Mtb* control is unclear, as highlighted by the
480 contrasting results on the roles of PD-1 and IDO1 during *Mtb* infection. PD-1 deletion in mice
481 and PD-1 blockade in rhesus macaques exacerbates TB disease[94,95], while IDO1 deletion does
482 not change bacterial burden in mice[96] yet targeting IDO1 with a small molecular inhibitor
483 promotes *Mtb* control in non-human primates[97,98]. Factors contributing to the lack of clarity for
484 the role of immunosuppression during *Mtb* infection could be that not all immunosuppressive
485 molecules may impact *Mtb* infection similarly and their effects may differ across models. For
486 example, deletion or blockade of IL-10 has varying effects in mice depending on the genetic
487 background and infection conditions[11,99–103]. Therefore, we applied a comparative approach to
488 re-examine whether myeloid cells play an immunosuppressive role during *Mtb* infection,
489 focusing on identifying conserved features of the myeloid cell response in *Mtb*-susceptible mice.
490 We first used scRNA-seq to characterize myeloid cells from *Mtb*-infected lungs of three
491 *Mtb*-susceptible mouse strains that all exhibit neutrophil-driven disease, namely, *Sp140*$^{-/-}$,
492 *Nos2*$^{-/-}$, and *Acod1*$^{-/-}$ mice[13–15,21]. Gene signatures derived from each of these mice significantly
493 outperform wild-type B6 mice in their ability to discriminate human active *Mtb* cases from
494 healthy controls or LTBI individuals, suggesting susceptible mice better mimic human disease.
495 Due to the high predictive strength of all three models' gene signatures, it is likely that there are
496 commonalities among the mouse models that are responsible for their discriminatory ability.
497 These commonalities do not appear to be a general reflection of increased inflammation as
498 these signatures could discriminate human active *Mtb* cases from lung cancer and pneumonia
499 patients. Initially, we hypothesized that a likely candidate for a shared response to *Mtb* infection
500 was type I IFN, as viral infections and the anti-viral type I IFN response correlate with the
501 severity of *Mtb* disease in humans[8,64,104–106]. A functional role for type I IFNs in driving *Mtb*
502 disease is also observed in mice, as inducers of type I IFNs exacerbate *Mtb* infection in B6
503 mice[36,107–112] and *Ifnar1* deletion rescues bacterial control in *Sst1*^{S} and *Sp140*-deficient
504 mice[14,15,17]. To our surprise, however, a type I IFN signature was not conserved across
505 susceptible mouse strains, and type I IFN receptor deletion had little to no effect on bacterial
506 control in *Nos2*$^{-/-}$ and *Acod1*$^{-/-}$ mice (**Fig. 2**), indicating that other pathways drive their *Mtb*
507 susceptibility.

As myeloid cells contribute to disease in each of the tested *Mtb* susceptible mouse models[13,15,21], we sought to define what pathways might be suppressed by myeloid cells to hinder *Mtb* control. We found that all three tested *Mtb*-susceptible mouse models had a shift in macrophage differentiation, exhibiting a reduction in *Trem2*$^+$ macrophages in favor of alternatively activated *Spp1*$^+$ macrophages. Interestingly, *Mtb*-restrictive B6 mice largely lacked *Spp1*$^+$ macrophages, and thus, *Spp1*$^+$ macrophage differentiation correlated with *Mtb*-susceptibility (**Fig. 3**). Macrophage differentiation into the SPP1$^+$ alternatively activated state also strongly correlates with tumor progression in humans[54]. Additionally, macrophage adoption of the SPP1$^+$ differentiation state was recently identified to be enhanced in the bronchial alveolar lavage fluid of active TB patients but not LTBI individuals or healthy controls[56] , and SPP1$^+$ macrophages were found to reside near human TB granulomas[57]. A commonality between *Mtb*-susceptible mice, human *Mtb* infection, and human cancer is the induction of a strong, chronic inflammatory state, raising the possibility that continued inflammation is a key driver of *Spp1*$^+$ macrophage differentiation. This concept is supported by the recent observation that SPP1$^+$ macrophages are associated with pathogenesis in individuals recently diagnosed with idiopathic pulmonary fibrosis, a disease with a median time to diagnosis of 2 years[65]. Additionally, SPP1$^+$ macrophage differentiation correlates with active rather than in remission Rheumatoid arthritis in humans[113]. Furthermore, SPP1 plasma levels were significantly higher in individuals with severe COVID-19 than those with mild/moderate COVID-19 or pneumonia[113] and SPP1 plasma levels correlate with human active TB disease[55].

As these reports correlating heightened inflammatory states with SPP1$^+$ macrophage differentiation are from human patients, it is challenging to understand the drivers of SPP1$^+$ differentiation. We, therefore, further characterized the macrophage response to *Mtb* infection in mice to better understand the mechanism underlying *Spp1*$^+$ differentiation. As part of this work, we identified CD9 and CD63 as markers that can be used for flow cytometry to distinguish mouse *Spp1*$^+$ from *Trem2*$^+$ macrophages (**Fig. 4**). Using these markers, we recapitulated our scRNA-seq data demonstrating a shift from *Trem2*$^+$ to *Spp1*$^+$ differentiation in all three susceptible mouse models relative to B6 mice. With this flow cytometry-based assay, we were able to demonstrate that direct infection by *Mtb* is not required for *Spp1*$^+$ differentiation and in fact *Trem2*$^+$ macrophages are infected at a higher rate than *Spp1*$^+$ macrophages. Additionally, we found that *Spp1*$^+$ versus *Trem2*$^+$ differentiation does not map onto the classic M1 versus M2 paradigm with both populations expressing canonical markers of M1 and M2 differentiation (e.g. iNOS and Arg1). While we have ruled out potential drivers of *Spp1*$^+$ differentiation, such as direct *Mtb* infection, further work is needed to identify the pathway or pathways promoting *Spp1*$^+$ macrophage differentiation. Nevertheless, *Spp1*$^+$ macrophages may play a key role in the early exacerbation of *Mtb* disease as they are the dominant macrophage source of IL-1Ra in mice. This expression pattern is conserved across species as we find SPP1$^+$ macrophages are also present in *Mtb* lung granulomas in non-human primates and humans and upregulate several immunosuppressive molecules relative to TREM2$^+$ macrophages, including *IL1RN* (**Fig. 3**). It should be noted that *Spp1*$^+$ differentiation appears to occur in response to strong inflammatory environments. Therefore, *Spp1*$^+$ macrophage differentiation and their IL-1Ra production is likely not the first step in TB progression but instead part of a positive feedback loop that accelerates progression, potentially in only a subset of human patients. Indeed, we observed that elevated *IL1RN* expression was detectable ~200 days prior to clinical diagnosis of TB in the Adolescent Cohort Study (**Supplementary Fig. 5**), suggesting that *IL1RN* is an early mechanism furthering human TB disease; however, it is not the initial trigger for loss of bacterial control as type I interferon responses are detectable 12-18 months prior to diagnosis in the same cohort[64]. The correlation between *Mtb* susceptibility and elevated IL-1Ra expression by macrophages was particularly intriguing as IL-1 signaling is a critical pathway for *Mtb* control[23,36–39].

However, the role of IL-1 during *Mtb* pathogenesis has been confusing. Mice deficient in IL-1 signaling are clearly susceptible to *Mtb*[23,36–40], but at the same time, many susceptible

559 mouse models exhibit elevated levels of IL-1[17,33], leading some to propose that IL-1-driven
560 neutrophilic inflammation actually exacerbates *Mtb*[13,29]. Here we propose that the apparently
561 paradoxical effects of IL-1 can be rationalized by an appreciation that high levels of IL-1
562 cytokine do not necessarily imply high levels of IL-1 signaling. Indeed, the beneficial effects of
563 IL-1 can be counteracted by high levels of the decoys IL-1R2 or IL-1Ra[114]. In addition to *Spp1*$^{+}$
564 macrophage expression of *Il1rn* (encoding IL-1Ra), our scRNA-seq data indicated that *Il1rn* was
565 constitutively expressed by neutrophils, as has also been shown for human neutrophils[58] (**Fig.**
566 **3**). Despite strong expression of *Il1rn* by neutrophils, neutrophils secreted considerably less IL-
567 1Ra than monocytes upon stimulation and macrophage-specific deletion of *Il1rn* restored control
568 of *Candida* infection[66]. Similarly, we found that expression of IL-1Ra by CD64^{+} cells, such as
569 macrophages, is specifically required for *Mtb* control as CD64-Cre-mediated deletion of *Il1rn*
570 was sufficient to rescue the susceptibility of *Sp140*$^{-/-}$ mice. This result correlates with human
571 disease as macrophages are one of the primary IL-1Ra-expressing cell types in human *Mtb*
572 granulomas[115].
573 Given the high levels of IL-1Ra expression by IMs in the susceptible mouse models, we
574 predicted that IL-1Ra adversely affects *Mtb* control in each of the susceptible lines, which was
575 confirmed by rescuing bacterial control in all three mouse lines with global deletion of IL-1Ra.
576 Further implicating macrophages as the dominant source of IL-1Ra during *Mtb* infection,
577 neutrophil-specific deletion of *Il1rn* resulted in little to no improvement in bacterial control in
578 *Acod1*$^{-/-}$ and *Nos2*$^{-/-}$ mice. This result aligns with our imaging data, as macrophages were
579 located significantly closer to *Mtb* than neutrophils in the diseased portion of the lungs of all
580 three susceptible mouse strains. However, the finding that global *Il1rn* deletion partially rescues
581 *Nos2*$^{-/-}$ mouse susceptibility was highly unexpected given prior claims that excessive IL-1
582 signaling is detrimental during *Mtb* infection[35] , particularly following the onset of the adaptive
583 immune response in *Nos2*$^{-/-}$ mice[13,33]. Our results instead suggest that the initial lack of
584 bacterial control in highly inflamed *Mtb*-susceptible mouse models, such as *Acod1*$^{-/-}$ and *Nos2*$^{-}$
585 $^{/-}$ mice, is primarily due to insufficient rather than excessive IL-1 signaling. Our results are in line
586 with the susceptibility of mice deficient in IL-1 signaling[23,36,38,39], as well as with anecdotal
587 evidence in humans reporting *Mtb* reactivation following IL-1Ra (Anakinra) treatment[116].
588 Importantly, our study focused on assessing bacterial burdens at a relatively early
589 timepoint after infection (day 25) and do not exclude the possibility that excessive IL-1 signaling
590 at later timepoints might have additional detrimental effects[117]. In particular, while IL-1 might be
591 important for orchestrating bacterial control, it is also well-known to mediate significant
592 immunopathology. This balance is exhibited in our previous work in which deletion of *Il1rn*
593 completely rescued bacterial control in *Sst1*^{S} mice early in infection but resulted in only a minor
594 improvement in survival, while deletion of a single allele of *Il1rn* nearly phenocopied the survival
595 of *Mtb*-restrictive B6 mice[17]. It thus remains unclear whether IL-1 signaling could be manipulated
596 therapeutically during human TB. Indeed, although myeloid cell production of IL-1Ra impairs
597 bacterial control, IL-1Ra expression likely evolved to limit host pathology and therefore may be
598 beneficial in many cases. Additionally, IL-1Ra is likely just one of many molecules that dictate
599 the balance between bacterial control and host pathology during *Mtb* infection. For example, our
600 gene signatures for the *Mtb*-susceptible mouse lines (but not the *Mtb*-restrictive B6 mice)
601 contain other known immunosuppressive molecules, such as *Cd274* and *Il18bp*. Overall, our
602 results therefore suggest that host-directed therapy to *Mtb* may require a delicate balance
603 between anti-bacterial and host-tolerance mechanisms.
604 The mechanism by which IL-1 exerts its protective effects remains the subject of
605 intensive study. In line with the limited expression of *Il1r1* by infected myeloid cells in our
606 scRNA-seq dataset, IL-1 has been proposed to act on uninfected bystander cells that then
607 promote myeloid cell *Mtb* control[23,39]. IL-1 signaling in either hematopoietic or non-hematopoietic
608 bystander cells is sufficient to mediate protection during early infection[23,39]. Yet the mechanism
609 for IL-1-mediated protection is not fully established, with eicosanoid regulation and synergistic

610 interactions between IL-1 and TNF being two potential mechanisms[36,39]. Our BM chimera
611 scRNA-seq experiments suggest that a lack of a single simple mechanism is due to the complex
612 and multifactorial effects of IL-1 on multiple cell types. We identified multiple IL-1-induced
613 cytokines and chemokines as potential activators of *Mtb*-harboring IMs, with the most likely
614 being *Ifng* and *Tnf*, two cytokines known to play a key role in *Mtb* restriction[3–5]. As IL-1 signaling
615 in $CD4^+$ T cells directly promotes cytokine production[69], it is likely that IL-1 directly enhances
616 *Ifng* and *Tnf* production by T cells and ILCs throughout *Mtb* infection. We hypothesize that IL-1-
617 enhanced *Ifng* and *Tnf* production by $CD4^+$ T cells likely then act on *Mtb*-harboring IMs to
618 promote their restriction of the infection. It is also possible that IL-1, potentially by promoting *Ifng*
619 and *Tnf*, modulates hematopoiesis thereby impacting *Mtb* control. This hypothesis is supported
620 by recent work demonstrating that the heightened type I interferon response in mice deficient in
621 *Il1r1* drives a shift in their hematopoiesis as well as their enhanced *Mtb* susceptibility[9]. During
622 *Legionella pneumophila* infection, IL-1 acts on type II alveolar epithelial cells inducing their
623 expression of GM-CSF[118], another cytokine that activates macrophages with an established
624 contribution to *Mtb* control[119–121]. Our stromal scRNA-seq dataset had limited coverage of
625 epithelial cells so we were unable to observe whether IL-1 also induces GM-CSF expression in
626 type II alveolar cells during *Mtb* infection. However, it is likely that this mechanism is conserved
627 between *Legionella* and *Mtb* infections given the critical role played by GM-CSF and stromal cell
628 IL-1 signaling in both infections.
629 In summary, our data support a model in which initial loss of bacterial control, whether
630 due to a type I IFN response, *Nos2*-, or *Acod1*-deficiency, results in myeloid cell influx into *Mtb*-
631 infected lungs. The incoming monocytes differentiate into IMs that adopt the $Spp1^+$ activation
632 state in animals with heightened inflammation, which correlates with the upregulation of IL-1Ra.
633 This high level of IL-1Ra expression hinders critical IL-1 signaling in hematopoietic and non-
634 hematopoietic cells, reducing the production of *Mtb*-restrictive cytokines, such as TNF and IFN-
635 γ. The IL-1Ra-mediated blockade of IL-1 thus generates an early positive feedback loop
636 promoting bacterial replication in which *Mtb*-harboring myeloid cells are unable to restrict the
637 bacteria. Enhanced bacterial replication leads to the influx of yet more myeloid cells and further
638 increases IL-1Ra levels. While intervention abolishing this early feedback loop (e.g. IL-1Ra
639 blockade) may temporarily promote bacterial control, the long-term cost of such an intervention
640 would likely be an increased risk of immunopathology as this intervention would not address the
641 initial insult that rendered the individual susceptible to TB, such as a strong type I IFN response.
642 Our results are largely consistent with a recently proposed 'tipping-point' model of
643 tuberculosis[122], which suggests that neutrophils cause a feedforward loop exacerbating disease
644 even if they are not the initial driver of loss of *Mtb* restriction. In this study, we provide molecular
645 evidence for this model by elucidating key molecular and cellular players that orchestrate the
646 tipping point.
647
648
649 **Acknowledgments**
650
651 We thank members of the Vance, Barton, Stanley, and Cox laboratories for advice and
652 discussions; the Stanley and Cox labs, and in particular D. Fox, for the shared operation of the
653 UC Berkeley BSL-3 and ABSL-3 labs; S. Gupta and P. Khatri for advice on analysis of human
654 cohorts; B. Malissen, S. Khader, and Y. Belkaid for mice; P. Dietzen, R. Chavez, J. Morales,
655 and J. Rodriguez for technical assistance; A. Valeros, H. Nolla, and K. Heydari of the UC
656 Berkeley Cancer Research Laboratory Flow Cytometry facility for assistance with flow
657 cytometry; H. Aaron and F. Ives of the UC Berkeley Cancer Research Laboratory Molecular
658 Imaging Center (RRID:SCR_017852) for assistance with confocal microscopy (supported by the
659 Helen Wills Neuroscience Institute). Model figures were created with BioRender.com. D.I.K. is
660 supported by an NIH Postdoctoral Fellowship (F32HL158250). C.G. is supported by the Swiss

National Science Foundation (310030B_201269) and the Rheumasearch Foundation. S.S. is supported by the NIH grant R01AI175614. R.E.V. is an Investigator of the Howard Hughes Medical Institute and is supported by NIH grants AI075039, AI063302 and AI155634.

Author Contributions

Conceptualization: D.I.K. and R.E.V. Investigation: D.I.K., O.V.L., and D.X.J. Data analysis: D.I.K., O.V.L., and B.A.R. Methodology: S.S. and M.M. Resources: C.G. and D.L.J. Writing: D.I.K. and R.E.V. with input from all co-authors. Funding acquisition: D.I.K. and R.E.V. Supervision: D.I.K. and R.E.V.

Declaration of Interests

R.E.V. consults for Tempest Therapeutics and X-biotix Therapeutics.

Figure Legends

Figure 1. Neutrophils and interstitial macrophages localize to diseased tissue, with macrophages localizing closer to *Mtb*. (**A**) Number of neutrophils, monocytes, IMs, and AMs in the lungs of *Mtb*-infected *Sp140*$^{-/-}$ (n = 13), *Sp140*$^{-/-}$ *Ifnar1*$^{-/-}$ (n = 11), *Acod1*$^{+/+}$ (n = 7), *Acod1*$^{+/-}$ (n = 6), *Acod1*$^{-/-}$ (n = 12), *Nos2*$^{+/+}$ (n = 4), *Nos2*$^{+/-}$ (n = 7), and *Nos2*$^{-/-}$ (n = 8) mice. (**B**) Representative images and (**C**) image quantification of *Mtb* (*Mtb*-mCherry^{+}, red), macrophages (SIRPα^{+}, blue), and neutrophils (Ly6G^{+}, green) in diseased and healthy portions of *Mtb*-infected B6 (n = 5) and *Sp140*$^{-/-}$ lungs (n = 6). (**D**) Representative images and (**E**) image quantification of *Mtb* (*Mtb*-mCherry^{+}, purple), macrophages (SIRPα^{+}, green), CD4^{+} T cells (CD4^{+}, yellow), and neutrophils (Ly6G^{+}, red) in diseased and healthy portions of *Mtb*-infected B6 (n = 6), *Acod1*$^{-/-}$ (n = 6), and *Nos2*$^{-/-}$ lungs (n = 6). (**F**) Quantification of the distance between macrophages or neutrophils to the nearest *Mtb* in representative images of B6, *Sp140*$^{-/-}$, *Acod1*$^{-/-}$, and *Nos2*$^{-/-}$ lungs. Lungs were analyzed for the experiments depicted in (A) – (F) 24-26 days after *Mtb*-Wasabi or *Mtb*-mCherry infection. The bars in (A) represent the median. Pooled data from two independent experiments are shown in (A), (C), and (E). Statistical significance in (A) by one-way ANOVA with Tukey's multiple comparison test, in (C) and (E) by paired t test, and in (F) by two tailed t test. *p < 0.05, **p < 0.01, ***p < 0.001, ****p < 0.0001.

Figure 2. *Nos2*- and *Acod1*-deficient mice mimic human *Mtb* progression but do not exhibit type I interferon-driven susceptibility. (**A**) Visualizing lung myeloid cell populations in a scRNA-seq dataset of cells from *Mtb*-infected B6, *Nos2*$^{-/-}$, *Acod1*$^{-/-}$, and *Sp140*$^{-/-}$ mice (n = 3 per genotype). (**B**) ROC curves of the ability of genes induced by *Mtb* infection in B6, *Nos2*$^{-/-}$, *Acod1*$^{-/-}$, or *Sp140*$^{-/-}$ mice to stratify human active *Mtb* patients (n = 151) and healthy controls (n = 98) in the TANDEM cohort (analysis of GSE114192) as well as stratifying human active *Mtb* patients (n = 16) and LTBI individuals (n = 31) in the Berry South Africa cohort (analysis of GSE107992). (**C**) UMAP plot and (**D**) quantification of myeloid cells undergoing type I interferon and/or IFN-γ signaling in the lungs of naïve or *Mtb*-infected B6, *Nos2*$^{-/-}$, *Acod1*$^{-/-}$, or *Sp140*$^{-/-}$ mice (n = 3 per genotype and infection status). (**E**) Lung bacterial burden in B6 (n = 10), *Sp140*$^{-/-}$ (n = 11), and *Sp140*$^{-/-}$ *Ifnar1*$^{-/-}$ (n = 12) mice infected with *Mtb*. (**F**) Lung bacterial burden in littermate control (n = 16), *Acod1*$^{-/-}$ *Ifnar1*$^{+/-}$ (n = 12), and *Acod1*$^{-/-}$ *Ifnar1*$^{-/-}$ (n = 9) mice infected with *Mtb*. (**G**) Lung bacterial burden in *Nos2*$^{+/+}$ littermate control (n = 4), *Nos2*$^{+/-}$ littermate control (n = 9), *Nos2*$^{+/-}$ *Ifnar1*$^{-/-}$ (n = 10), *Nos2*$^{-/-}$ (n = 8), and *Nos2*$^{-/-}$ *Ifnar1*$^{-/-}$ (n = 11) mice infected with *Mtb*. Lungs were analyzed 25-27 days after *Mtb*-Wasabi infection. The bars in (E), (F), and (G) represent the median. Pooled data from two independent experiments are shown in

711 (E), (F), and (G). Statistical significance in (D), (E), (F), and (G) by one-way ANOVA with
712 Tukey's multiple comparison test. *p < 0.05, **p < 0.01, ***p < 0.001, ****p < 0.0001.
713
714 **Figure 3. *Spp1*$^{+}$ macrophage differentiation and their expression of immunosuppressive**
715 **molecules, including IL-1 receptor antagonist, correlates with *Mtb* susceptibility in mice**
716 **and is conserved between mice, *Mtb*-infected non-human primates, and *Mtb*-infected**
717 **humans.** (**A**) Lung *Mtb*-infected monocyte and macrophage expression of *Spp1, Trem2,* and
718 *Cxcl9*, (**B**) the resulting cell annotation, and (**C**) lung *Mtb*-infected monocyte and macrophage
719 populations visualized separately for B6, *Nos2*$^{-/-}$, *Acod1*$^{-/-}$, and *Sp140*$^{-/-}$ mice (n = 3 per
720 genotype). (**D**) Quantification of the frequency of *Mtb*-infected IMs, *Spp1*$^{+}$ IMs, and *Trem2*$^{+}$ IMs
721 among all IMs for B6, *Nos2*$^{-/-}$, *Acod1*$^{-/-}$, and *Sp140*$^{-/-}$ mice (n = 3 per genotype). (**E**) Volcano
722 plot of the differentially expressed genes in *Mtb*-infected *Spp1*$^{+}$ IMs relative to *Trem2*$^{+}$ IMs
723 (combined analysis of cells from B6, *Nos2*$^{-/-}$, *Acod1*$^{-/-}$, and *Sp140*$^{-/-}$ mice). (**F**) *Il1rn* expression
724 measured by scRNA-seq of *Mtb*-infected myeloid cell populations in the lungs of B6, *Nos2*$^{-/-}$,
725 *Acod1*$^{-/-}$, and *Sp140*$^{-/-}$ mice (n = 3 per genotype). (**G**) Cell clustering and (**H**) volcano plot of the
726 differentially expressed genes in SPP1^{+} IMs relative to TREM2^{+} IMs for cells from IgG control
727 antibody-treated *Mtb*-infected non-human primate granulomas (analysis of
728 https://fairdomhub.org/studies/1134). (**I**) Cell clustering and (**J**) volcano plot of differentially
729 expressed genes in SPP1^{+} IMs relative to TREM2^{+} IMs from 18F-FDG high (n = 5) and low (n =
730 6) portions of lung resections from *Mtb*-infected humans (analysis of GSE192483). (**K**) *IL1RN*
731 expression by innate immune cells in FDG high and low signal portions of *Mtb*-infected human
732 lungs as measured by scRNA-seq (analysis of GSE192483). (**L**) ROC curve depicting the
733 ability of *IL1RN* expression to stratify human active *Mtb* patients (n = 151) and healthy controls
734 (n = 98) in the TANDEM cohort (analysis of GSE114192). (**M**) ROC curve depicting the ability of
735 *IL1RN* expression to stratify human active *Mtb* patients (n = 16) and LTBI individuals (n = 31) in
736 the Berry South Africa cohort (analysis of GSE107992). Lungs were analyzed for the
737 experiments depicted in (A) – (F) 25 days after *Mtb*-Wasabi infection and 6 weeks after *Mtb*
738 infection for those depicted in (G) and (H). The bars in (D) represent the median. Statistical
739 significance in (E), (F), (H), and (J) was calculated with the Wilcoxon Rank-Sum test with
740 Bonferroni correction and in (D) by two-way ANOVA with Tukey's multiple comparison test. ****p
741 < 0.0001.
742
743 **Figure 4. *Spp1*$^{+}$ and *Trem2*$^{+}$ macrophage differentiation is identifiable by flow cytometry**
744 **and does not overlap with M1 vs M2 macrophage differentiation.** (**A**) Lung *Mtb*-infected
745 monocyte and macrophage expression of *Cd9, Cd63,* and *Itgax* plotted alongside annotated
746 myeloid cell clusters for the *Mtb*-infected lung scRNA-seq dataset (combined analysis of cells
747 from B6, *Nos2*$^{-/-}$, *Acod1*$^{-/-}$, and *Sp140*$^{-/-}$ mice, n = 3 per genotype). (**B**) Gating scheme used to
748 identify mature IMs (PD-L1^{hi} CD11c^{hi}) as well as mature *Spp1*$^{+}$ IMs (PD-L1^{hi} CD11c^{hi} CD9^{hi}
749 CD63^{low}) and mature *Trem2*$^{+}$ IMs (PD-L1^{hi} CD11c^{hi} CD9^{low} CD63^{hi}) in B6 and *Sp140*$^{-/-}$ mice. (**C**)
750 Representative histogram depicting *Spp1*$^{+}$ IM (red), *Trem2*$^{+}$ IM (blue), and IM (grey) expression
751 of Alcam, Trem2, and C1q in the lungs of *Mtb*-infected mice. (**D**) Quantification of the frequency
752 of the total mature IMs, (**E**) mature *Spp1*$^{+}$ IMs, and (**F**) mature *Trem2*$^{+}$ IMs in the lungs of *Mtb*-
753 infected B6 (n = 9), *Sp140*$^{-/-}$ (n = 16), *Nos2*$^{-/-}$ (n = 13), and *Acod1*$^{-/-}$ (n = 9) mice. (**G**) UMAP
754 visualization comparing the frequency of the monocyte and macrophage clusters for bystander
755 cells versus *Mtb*-infected cells (combined analysis of cells from B6, *Nos2*$^{-/-}$, *Acod1*$^{-/-}$, and
756 *Sp140*$^{-/-}$ mice, n = 3 per genotype). (**H**) Flow cytometric analysis of *Mtb* infection frequency
757 among IM, *Spp1*$^{+}$ IM, and *Trem*2^{+} IM in the lungs of B6 (n = 13) and *Sp140*$^{-/-}$ mice (n = 12). (**I**)
758 Frequency of iNOS^{+} and Arg1^{+} cells among IMs in *Mtb*-infected lungs from B6 (n = 9) and
759 *Sp140*$^{-/-}$ (n = 12) mice. (**J**) scRNA-seq analysis of Nos2 and Arg1 expression in monocytes and
760 macrophages from *Mtb*-infected lungs of B6, *Sp140*$^{-/-}$, *Nos2*$^{-/-}$, and *Acod1*$^{-/-}$ mice (n = 3 per
761 genotype). (**K**) Representative histogram of Arg1 and iNOS expression by mature *Trem2*$^{+}$ IM

762 (blue), mature *Spp1*$^{+}$ IM (red), mature IM (green), and monocytes (grey) from *Mtb*-infected
763 mouse lungs. Lungs were analyzed 24-28 days after *Mtb* or *Mtb*-Wasabi infection. The bars in
764 (D) – (F), (H), and (I) represent the median. Pooled data from two independent experiments are
765 shown in (D) – (F), (H), and (I). Statistical significance in (H) was calculated by one-way ANOVA
766 with Tukey's multiple comparison test and in (D) – (F) and (I) by two-tailed t test. *p < 0.05, **p <
767 0.01, ***p < 0.001, ****p < 0.0001.
768
769 **Figure 5. Macrophage-derived IL-1Ra is a conserved driver of *Mtb* susceptibility.**
770 (**A**) Lung bacterial burden in B6 (n = 10) and *Il1rn*$^{-/-}$ mice (n = 9) following *Mtb* infection. (**B**)
771 Lung bacterial burden in Mrp8^{Cre-} *Il1rn*$^{fl/fl}$ (n = 5) and Mrp8^{Cre+} *Il1rn*$^{fl/fl}$ mice (n = 6) following *Mtb*
772 infection. (**C**) Lung bacterial burden in *Sp140*$^{-/-}$ (n = 14), *Sp140*$^{-/-}$ *Il1rn* $^{+/-}$ (n = 16), *Sp140*$^{-/-}$
773 *Il1rn*$^{-/-}$ (n = 8), and *Sp140*$^{-/-}$ *Ifnar1*$^{-/-}$ mice (n = 15) following *Mtb* infection. (**D**) Lung bacterial
774 burden and (**E**) neutrophil numbers in *Acod1*$^{+/-}$ *Il1rn*$^{+/+}$ (n = 7), *Acod1*$^{-/-}$ *Il1rn*$^{+/+}$ (n = 14), *Acod1*$^{-/-}$
775 *Il1rn*$^{+/-}$ (n = 28), and *Acod1*$^{-/-}$ *Il1rn*$^{-/-}$ (n = 8) mice following *Mtb* infection. (**F**) Lung bacterial
776 burden in B6 (n = 7), *Acod1*$^{-/-}$ Mrp8^{Cre-} *Il1rn*$^{fl/fl}$ (n = 9) and *Acod1*$^{-/-}$ Mrp8^{Cre+} *Il1rn*$^{fl/fl}$ mice (n = 9)
777 following *Mtb* infection. (**G**) Lung bacterial burden and (**H**) neutrophil numbers in *Nos2*-sufficient
778 controls (n = 11), *Nos2*$^{-/-}$ *Il1rn*$^{+/+}$ (n = 8-16), *Nos2*$^{-/-}$ *Il1rn*$^{+/-}$ (n = 8-18), *Nos2*$^{-/-}$ *Il1rn*$^{-/-}$ (n = 6-19),
779 littermate control (n = 6) and B6 (n = 5) mice following *Mtb* infection. (**I**) Lung bacterial burden in
780 B6 (n = 9), *Nos2*$^{-/-}$ Mrp8^{Cre-} *Il1rn*$^{fl/fl}$ (n = 19) and *Nos2*$^{-/-}$ Mrp8^{Cre+} *Il1rn*$^{fl/fl}$ mice (n = 11) following
781 *Mtb* infection. (**J**) Lung *Mtb* burden in *Sp140*$^{+/-}$ littermate control (n = 19), *Sp140*$^{-/-}$ littermate
782 control (n = 19), and *Sp140*$^{-/-}$ *Il1rn*$^{fl/fl}$ *CD64*$^{cre+}$ (n = 24) mice. Lungs were analyzed 24-28 days
783 after *Mtb* or *Mtb*-Wasabi infection. The bars in (A) – (J) represent the median. Pooled data from
784 two independent experiments are shown in (A) – (I) and three independent experiments in (J).
785 Statistical significance in (A) and (B) was calculated with a two-tailed t test while in (C) - (J) it
786 was calculated by one-way ANOVA with Tukey's multiple comparison test. *p < 0.05, **p < 0.01,
787 ***p < 0.001, ****p < 0.0001.
788
789 **Figure 6. IL-1 enhances cytokine and chemokine expression by Th17, NKT17, and ILC3 as**
790 **well as stromal cells.** (**A**) Schematic of the BM chimera mice used in panels (B) – (G). (**B**) T
791 cell populations and (**C**) their expression of *Il1r1* in the *Mtb*-infected lungs of the BM chimera
792 mice. (**D**) Volcano plot of the differentially expressed genes in the WT Th17 cells relative to
793 *Il1r1*$^{-/-}$ Th17 cells during *Mtb* infection. (**E**) Innate lymphoid cell populations and (**F**) their
794 expression of *Il1r1* in the *Mtb*-infected lungs of the BM chimera mice. (**G**) Differentially
795 expressed genes in the WT ILC3 and NKT17 cells relative to *Il1r1*$^{-/-}$ cells during *Mtb* infection.
796 (**H**) Schematic of the BM chimera mice used in panels (I) – (K). (**I**) Non-hematopoietic cell
797 populations and (**J**) their expression of *Il1r1* in the *Mtb*-infected lungs of the BM chimera mice.
798 (**K**) Differentially expressed genes in the WT myofibroblast, fibroblast, and endothelial cells
799 relative to *Il1r1*$^{-/-}$ cells during *Mtb* infection. (**I**) Schematic of the BM chimera mice used in panel
800 (M). (**M**) Lung *Mtb* burden in BM chimera mice that received *Il1r1*$^{-/-}$: CD45.1 mixed BM (n = 8),
801 *Il1r1*$^{-/-}$: *Il17*$^{-/-}$ *Il22*$^{-/-}$ mixed BM (n = 10), or *Il1r1*$^{-/-}$ BM (n = 13). Lungs were analyzed 25 days
802 after *Mtb*-Wasabi infection. The bars in (M) represent the median. Pooled data from two
803 independent experiments are shown in (M). Statistical significance in (D), (G), and (K) was
804 calculated with the Wilcoxon Rank-Sum test with Bonferroni correction and in (M) by one-way
805 ANOVA with Tukey's multiple comparison test. *p < 0.05.
806
807
808 **Materials and Methods**
809
810 **Mice**. Following University of California Berkeley Institutional Animal Care and Use Committee
811 regulatory standards, mice were housed at 23°C with a 12-hour light-dark cycle and maintained
812 under specific pathogen-free conditions. Male and female mice were used for experiments. Mice

were age-matched with littermate controls when possible and 6-12 weeks old at the start of the infections. C57BL/6 (B6), B6.129S2-Ifnar1^{tm1Agt}/Mmjax (*Ifnar1*$^{-/-}$)[123], B6.SJL-*Ptprc*^{a} *Pepc*^{b}/BoyJ (CD45.1)[124], B6.129S7-*Il1r1*^{tm1Imx}/J (*Il1r1*$^{-/-}$)[125], B6.129(Cg)-*Il1r1*$^{tm1.1Rbl}$/J (*Il1r1*$^{fl/fl}$)[126], B6.129P2-*Avil*$^{tm2(cre)Fawa}$/J (Adv^{Cre})[127], B6.129P2-*Nos2*^{tm1Lau}/J (*Nos2*$^{-/-}$)[128], and C57BL/6NJ-*Acod1*$^{em1(IMPC)J}$/J (*Acod1*$^{-/-}$) mice were purchased from Jackson Laboratories. B6-Fcgr1^{tm2Ciphe} (CD64^{Cre})[67] mice were a gift from B. Malissen at Centre d'Immunologie de Marseille Luminy and were provided by Y. Belkaid at the National Institutes of Health. BM from *Il17*$^{-/-}$*Il22*$^{-/-}$ mice was a gift from S. Khader at the University of Chicago. Il1rn$^{tm1.1Cga}$ (*Il1rn*^{fl})[68] were generated by Cem Gabay at the University of Geneva and were provided by A. Luster at Massachusetts General Hospital. *Sp140*$^{-/-}$ mice were previously generated in-house[14]. *Sp140*$^{-/-}$ *Ifnar1*$^{-/-}$, *Acod1*$^{-/-}$ *Ifnar1*$^{-/-}$, and *Nos2*$^{-/-}$ *Ifnar1*$^{-/-}$ mice were generated by crossing *Sp140*$^{-/-}$, *Acod1*$^{-/-}$, and *Nos2*$^{-/-}$ mice with *Ifnar1*$^{-/-}$ mice in-house, respectively. *Sp140*$^{-/-}$, *Acod1*$^{-/-}$, and *Nos2*$^{-/-}$ mice were crossed in-house with *Il1rn*$^{-/-}$ mice to generate *Sp140*$^{-/-}$ *Il1rn*$^{-/-}$, *Acod1*$^{-/-}$ *Il1rn*$^{-/-}$, and *Nos2*$^{-/-}$ *Il1rn*$^{-/-}$ mice. *Sp140*$^{-/-}$ *Il1rn*$^{fl/fl}$ CD64^{Cre} mice were generated by crossing *Sp140*$^{-/-}$ mice with *Il1rn*$^{fl/fl}$ and CD64^{Cre} mice in-house. *Acod1*$^{-/-}$ *Il1rn*$^{fl/fl}$ Mrp8^{Cre} mice and *Nos2*$^{-/-}$ *Il1rn*$^{fl/fl}$ Mrp8^{Cre} mice were generated by crossing *Acod1*$^{-/-}$ or *Nos2*$^{-/-}$ mice with *Il1rn*$^{fl/fl}$ and Mrp8^{Cre} mice in-house. Adv^{Cre} *Il1r1*$^{fl/fl}$ and CD64^{Cre} *Il1r1*$^{fl/fl}$ mice were generated by crossing Adv^{Cre} and CD64^{Cre} mice with *Il1r1*$^{fl/fl}$ mice in-house.

Bone marrow chimera mice. Adult mice were lethally irradiated with a Precision X-Rad320 X-Ray irradiator (North Branford, CT) using a split dose of 500 rads each round with irradiation occurring 4-12 hours apart. Bone marrow (BM) from donor mice indicated in the figures was prepared by mashing femurs with a mortar and pestle to generate a single cell suspension. Red blood cells were then lysed with ACK lysis buffer (Thermo Fisher Scientific). The cells were then diluted in PBS and 1×10^7 cells (either all one genotype or a 1 : 1 mix of two genotypes for mixed BM chimera mice) were retro-orbitally injected into each recipient mouse. Mice were housed for at least 8 weeks post-injection to permit hematopoietic reconstitution prior to their use in experiments.

***Mtb* infections**. *Mtb* expressing Wasabi (*Mtb*-Wasabi) and *Mtb*-mCherry were generated using *Mtb* Erdman, a gift from S. A. Stanley, that had been passaged 2 or fewer times *in vitro*. *Mtb* was transformed with the pTEC15 plasmid (a gift from Lalita Ramakrishnan; Addgene plasmid # 30174)[129] or the pMSP12::mCherry plasmid (a gift from Lalita Ramakrishnan; Addgene plasmid # 30167) to generate *Mtb*-Wasabi and *Mtb*-mCherry, respectively. For the transformation, *Mtb* was cultured in Middlebrook 7H9 liquid medium supplemented with 10% albumin-dextrose-saline, 0.4% glycerol, and 0.05% Tween-80 for 5 days at 37°C then washed in 10% glycerol to remove salts. Washed *Mtb* was electroporated with 1 µg DNA using a 2 mm electroporation cuvette and the following settings: 2500 volts, 1000 Ohms, 25 µF. Electroporated *Mtb* was grown on 7H11 plates supplemented with 10% oleic acid, albumin, dextrose, and catalase, 0.5% glycerol, and either 200 µg / mL Hygromycin for *Mtb*-Wasabi or 50 µg / mL Kanamycin for *Mtb*-mCherry for 3-4 weeks at 37°C. Colonies were picked and cultured in 10 mL inkwell flasks for 7 days at 37°C and then expanded into a 100 mL culture for 4-5 days at 37°C using 7H9 medium supplemented with 10% albumin-dextrose-saline, 0.4% glycerol, 0.05% Tween-80, and either Hygromycin for *Mtb*-Wasabi or Kanamycin for *Mtb*-mCherry. At log phase, the Mtb was filtered through a 5 µm syringe filter and frozen in 1 mL aliquots in 10% glycerol. Frozen cultures were diluted in distilled water to an O.D. of 0.0017 and then aerosolized with an inhalation exposure system (Glas-Col, Terre Haute, IN) thereby delivering ~10-100 *Mtb* per mouse as determined by plating lungs day 1 post-infection to assess bacterial burden.

Tissue Processing for CFU and Flow cytometry. Mice were harvested at 24-28 days following *Mtb* infection. Lungs were collected in gentleMACS C tube (Miltenyi Biotec) containing

3 mL of RPMI media with 70 µg / mL of Liberase TM (Roche) and 30 µg / mL of DNase I (Roche) and then processed into chunks using the lung_01 setting on a gentleMACS (Miltenyi Biotec). Samples were then digested at 37°C for 30 minutes before being homogenized with the lung_02 setting on the gentleMACS. 2 mL of PBS with 20% Newborn Calf Serum (Thermo Fisher Scientific) were added to each sample to quench the digest before samples were filtered through 70 µm SmartStrainers (Miltenyi Biotec).

Measuring Bacterial Burden. *Mtb* burden was assessed by serial dilution of the lung single cell suspension in phosphate-buffered saline (PBS) with 0.05% Tween-80. The dilutions were plated on 7H11 plates supplemented with 10% oleic acid, albumin, dextrose, and catalase and 0.5% glycerol and colonies were counted ~3 weeks after plating.

Flow Cytometry. Flow cytometry was performed by staining 100 µLs of lung single cell suspension with antibodies in PBS with 2% Newborn Calf Serum and 0.05% Sodium azide. A fixable viability dye (Ghost Dye Violet 510 or 540 or Red 780; Tonbo Biosciences), Super Bright Complete Staining Buffer (Thermo Fisher Scientific), and True-Stain Monocyte Blocker (BioLegend) were also added to every sample during surface antibody staining. Surface stains were incubated for 30-60 minutes at room temperature using a selection of the following antibodies: TruStain FcX PLUS (S17011E, BioLegend), BUV496-labeled CD45 (30-F11, BD Biosciences), BUV395-labeled CD11b (M1/70, BD Biosciences), BUV737-labeled CD11c (HL3, BD Biosciences), APC-R700-labeled Siglec F (E50-2440, BD Biosciences), PE-labeled MerTK (DS5MMER, Thermo Fisher Scientific), Super Bright 645-labeled MHC II (M5/114.15.2, Thermo Fisher Scientific), BV421-labeled PD-L1 (MIH5, BD Biosciences), BV711-labeled Ly6C (HK1.4 , BioLegend), PE-Cy7-labeled MerTK (DS5MMER, Thermo Fisher Scientific), APC-labeled CD64 (X54-5/7.1, BioLegend), BUV563-labeled Ly6G (1A8, BD Biosciences), BV605-labeled MHC II (M5/114.15.2, BioLegend), Percp-Cy5.5-labeled CD9 (MZ3, BioLegend), eFluor 450-labeled Ly6D (49-H4, Thermo Fisher Scientific), BV480-labeled Fcer1a (MAR-1, BD Biosciences), BV650-labeled CD8α (53-6.7, BioLegend), BV785-labeled CD16.2 (9E9, BioLegend), AF594-labeled TREM2 (237920, R&D systems), AF647-labeled XCR1 (ZET, XCR1), APC-Fire 750-labeled CD19 (6D5, BioLegend), APC-Fire 750-labeled CD90.2 (30-H12, BioLegend), BUV615-labeled SIRPα (P84, BD Biosciences), BUV661-labeled B220 (RA3-6B2, BD Biosciences), PE-labeled Alcam (eBioALC48, Thermo Fisher Scientific), RB744-labeled CD9 (KMC8, BD Biosciences), BUV805-labeled PD-L1 (MIH5, BD Biosciences), and BUV805-labeled CD26 (H194-112, BD Biosciences). Following surface staining, samples were washed with PBS with 2% Newborn Calf Serum and 0.05% Sodium azide and then fixed for 20 minutes at room temperature with cytofix/cytoperm (BD biosciences) prior to removal from the BSL3. If intracellular staining was performed, samples were incubated overnight at 4°C with combinations of the following antibodies: PE-Cy7-labeled CD63 (NVG-2, BioLegend), FITC-labeled C1q (JL-1, Thermo Fisher Scientific), AF700-labeled CD63 (NVG-2, BioLegend), eFluor 450-labeled Arg1 (A1exF5, Thermo Fisher Scientific), AF532-labeled iNOS (CXNFT, Thermo Fisher Scientific), and Percp-eFluor 710-labeled iNOS (CXNFT, Thermo Fisher Scientific). After washing out the intracellular stain, each sample received AccuCheck Counting Beads (Invitrogen) and was then analyzed on an Aurora (Cytek) flow cytometer. Data were analyzed with Flowjo version 10 (BD Biosciences).

Confocal microscopy. A Zeiss LSM 880 laser scanning confocal microscope with 405, 458, 488, 514, 561, 594, and 633 lasers, with two photomultiplier detectors, a 34-channel GaASP spectral detector system, and a 2-channel AiryScan detector was used for microscopy. 20 µm sections were prepared from paraformaldehyde-fixed lungs from *Mtb*-mCherry-infected B6 and *Sp140*$^{-/-}$ mice. The sections were stained overnight at 4°C with the following antibodies: BV421-labeled SIRPα (P84, BD Biosciences), Pacific Blue–labeled B220 (RA3-6B2, BioLegend),

915 eF506-labeled CD4 (RM4-5, BioLegend), and AF647-labeled Ly6G (1A8, BioLegend). Diseased
916 and healthy lesions were identified in stained sections with a 5× air objective and then imaged
917 as a 20 µm z-stack acquired at a 1.5 µm step size with a 63× oil immersion objective lens with a
918 numerical aperture of 1.4. The 63× oil immersion objective lens with a numerical aperture of 1.4
919 was also used to image single color-stained Ultracomp eBeads Plus (Thermo Fisher Scientific)
920 for generating a compensation matrix.
921
922 **Image processing and histo-cytometry analysis**. The Generate Compensations Matrix
923 script[130] was used in ImageJ to create a compensation matrix based on the single color-stained
924 control images of the Ultracomp eBeads Plus (Thermo Fisher Scientific). The resulting
925 compensation matrix was used for spectral unmixing of the lung images using Chrysalis
926 software[130], which was also used to rescale the data and generate new channels based on
927 mathematical operations performed on existing channels. Imaris 9.9.1 (Bitplane) was used on
928 the processed lung images to digitally identify cells based on protein expression using the
929 surface creation tool and to measure the distance between *Mtb* and the nearest macrophage or
930 neutrophil[131]. Statistics for the identified cells were exported from Imaris and then imported into
931 FlowJo version 10 (BD Biosciences) for quantitative image analysis.
932
933 **Sorting Immune Cells for scRNA-seq analysis**. For the myeloid dataset, lungs from 3 *Mtb*-
934 Wasabi-infected as well as from 3 naïve *Acod1*$^{-/-}$ and 3 naïve *Nos2*$^{-/-}$ mice were processed as
935 described for CFU and flow cytometry analysis 25 days after infection with the following slight
936 modification: 3 minutes before harvesting, 0.25 µg of TotalSeq-A-labeled CD45.2 (104,
937 BioLegend) was intravenously injected into each mouse to label cells in the vasculature[132].
938 Surface staining of lung single cell suspensions was performed in PBS with 2% Newborn Calf
939 Serum on ice for 30 minutes with the following antibodies: TruStain FcX PLUS (S17011E,
940 BioLegend), APC-labeled Ly6G (1A8, BioLegend), APC-labeled CD64 (X54-5/7.1, BioLegend),
941 and TotalSeq-A-labeled Ly6G (1A8, BioLegend). Magnetic enrichment was then performed with
942 the EasySep APC Positive Selection Kit II (StemCell Technologies) and MojoSort Magnets
943 (BioLegend) to increase the frequency of myeloid cells within the sample prior to sorting.
944 Following enrichment, samples were stained on ice for 45 minutes in PBS with 2% Newborn
945 Calf Serum and True-Stain Monocyte Blocker (BioLegend) using a combination of the following
946 antibodies: TotalSeq-A-labeled Ly6C (HK1.4, BioLegend), TotalSeq-A-labeled CD44 (IM7,
947 BioLegend), TotalSeq-A-labeled CD274 (MIH6 , BioLegend), TotalSeq-A-labeled Siglec F
948 (S17007L, BioLegend), TotalSeq-A-labeled CSF1R (AFS98, BioLegend), TotalSeq-A-labeled
949 CD11b (M1/70, BioLegend), TotalSeq-A-labeled CD86 (GL-1, BioLegend), TotalSeq-A-labeled
950 MHC II (M5/114.15.2, BioLegend), TotalSeq-A-labeled CX3CR1 (SA011F11, BioLegend),
951 TotalSeq-A-labeled CD11c (N418, BioLegend), TotalSeq-A-labeled CCR2 (SA203G11,
952 BioLegend), TotalSeq-A-labeled CD62L (MEL-14, BioLegend), anti-mouse TotalSeq-A Hashtag
953 antibody (1-6; BioLegend), PE-labeled Siglec F (S17007L, BioLegend), Pacific Blue-labeled
954 B220 (RA3-6B2, BioLegend), and Pacific Blue-labeled CD90.2 (53-2.1, BioLegend). The
955 TotalSeq-A-labeled antibodies detect protein expression in the scRNA-seq dataset, while the
956 Hashtag antibodies allow several samples to be multiplexed together in a single lane on a 10X
957 Genomics Chromium Next GEM Chip[133]. After staining, the samples were incubated with Sytox
958 Blue Dead Cell Stain (Thermo Fisher Scientific) and sort purified using a 100 µm sorting chip in
959 a 4 laser SH-800 cell sorter (Sony) on the purity setting. For *Mtb*-infected mice, *Mtb*-infected
960 cells and bystander myeloid cells were individually purified, while samples from naïve lungs
961 were sorted as macrophages and a mixture of neutrophils and monocytes that were then
962 combined at a 1:2 ratio for greater representation of macrophages in the scRNA-seq dataset.
963 The stromal cell dataset was generated by infecting BM chimera mice made by
964 transferring CD45.1 BM into lethally irradiated B6 or *Il1r1*$^{-/-}$ hosts with *Mtb* 8 weeks post-
965 reconstitution. Lungs from the infected animals as well as naïve chimera mice were harvested

966 and processed as described for CFU and flow cytometry analysis. ACK lysing buffer (Thermo
967 Fisher Scientific) was used to lyse the red blood cells in the samples, which were then stained
968 for 30 minutes on ice with TruStain FcX PLUS (S17011E, BioLegend) and PE-Cy7-labeled
969 CD45 (30-F11, BioLegend) antibody. The EasySep PE Positive Selection Kit II (StemCell
970 Technologies) and MojoSort Magnets (BioLegend) were used to perform negative selection to
971 enrich the $CD45^{-}$ non-hematopoietic cells. The enriched cells were incubated with Sytox Green
972 Dead Cell Stain (Thermo Fisher Scientific) and live $CD45^{-}$ were sort purified using a 130 µm
973 sorting chip in a 4 laser SH-800 cell sorter (Sony) on the purity setting.
974 The T cell and ILC datasets were generated by *Mtb* infection of mixed BM chimera mice
975 generated by transferring WT CD45.1/2 and *Il1r1*$^{-/-}$ BM into lethally irradiated CD45.1 mice.
976 Lungs were harvested 25 days post-infection and processed as described for measuring CFU
977 and performing flow cytometry. Three mice were used for the T cell dataset, while the rarity of
978 the ILCs required pooling lungs into 3 samples (2 samples containing 5 lungs and 1 sample
979 containing 6 lungs). The T cell samples were treated with ACK lysing buffer (Thermo Fisher
980 Scientific) to lyse the red blood cells and then stained on ice for 30 minutes with the following
981 antibodies: BV421-labeled CD45.1 (A20, BioLegend), BV785-labeled CD45.2 (104, BioLegend),
982 PE-labeled CD3e (17A2, BioLegend), APC-labeled CD11b (M1/70, Cytek), APC-labeled CD11c
983 (N418, Cytek), APC-labeled CD19 (1D3, Cytek), TotalSeq-A-labeled Ly6C (HK1.4, BioLegend),
984 TotalSeq-A-labeled CD44 (IM7, BioLegend), TotalSeq-A-labeled CD274 (MIH6 , BioLegend),
985 TotalSeq-A-labeled CX3CR1 (SA011F11, BioLegend), TotalSeq-A-labeled CD62L (MEL-14,
986 BioLegend), TotalSeq-A-labeled TCRβ (H57-597, BioLegend), TotalSeq-A-labeled CD49a (,
987 BioLegend), TotalSeq-A-labeled CD49a (HMα1, BioLegend), TotalSeq-A-labeled NKp46
988 (29A1.4, BioLegend), TotalSeq-A-labeled CD4 (RM4-5, BioLegend), TotalSeq-A-labeled ST2
989 (DIH9, BioLegend), TotalSeq-A-labeled CD25 (PC61, BioLegend), TotalSeq-A-labeled CD45.1
990 (A20, BioLegend), TotalSeq-A-labeled CD45.2 (104, BioLegend), TotalSeq-A-labeled CD8a (53-
991 6.7, BioLegend), TotalSeq-A-labeled CXCR5 (L138D7, BioLegend), TotalSeq-A-labeled CCR6
992 (29-2L17, BioLegend), and anti-mouse TotalSeq-A Hashtag antibody (1-3; BioLegend). The
993 stained T cell samples were then incubated with Sytox Green Dead Cell Stain (Thermo Fisher
994 Scientific) and T cells (Live $CD3e^{+}$ $CD11b^{-}$ $CD11c^{-}$ $CD19^{-}$ $CD45.1^{+}$ or $CD45.2^{+}$ cells) were sort
995 purified using a 100 µm sorting chip in a 4 laser SH-800 cell sorter (Sony) on the purity setting.
996 The ILC samples treated with ACK lysing buffer (Thermo Fisher Scientific) were stained
997 on ice for 25 minutes with the following panel of lineage-specific antibodies: Biotin-labeled TER-
998 119 (TER-119, BioLegend), Biotin-labeled GR-1 (RB6-8C5, BioLegend), Biotin-labeled CD3e
999 (145-2C11, BioLegend), Biotin-labeled CD11b (M1/70, BioLegend), Biotin-labeled B220 (RA3-
1000 6B2, BioLegend), and Biotin-labeled TCRγ/δ (GL3, BioLegend). $Lineage^{-}$ cells were enriched by
1001 negative selection using the EasySep Streptavidin RapidSpheres Isolation Kit (StemCell
1002 Technologies) and MojoSort Magnets (BioLegend). Enriched samples were then stained on ice
1003 for 30 minutes with the following antibodies: BV421-labeled CD45.1 (A20, BioLegend), BV785-
1004 labeled CD45.2 (104, BioLegend), PE-labeled CD127 (A7R34, BioLegend), Alexa Fluor 700-
1005 labeled CD127 (30-H12, BioLegend), Biotin-labeled CD5 (53-7.3, BioLegend), Biotin-labeled
1006 TCRβ (H57-597, BioLegend), TotalSeq-A-labeled Ly6C (HK1.4, BioLegend), TotalSeq-A-
1007 labeled CD44 (IM7, BioLegend), TotalSeq-A-labeled CD274 (MIH6 , BioLegend), TotalSeq-A-
1008 labeled CX3CR1 (SA011F11, BioLegend), TotalSeq-A-labeled CD62L (MEL-14, BioLegend),
1009 TotalSeq-A-labeled TCRβ (H57-597, BioLegend), TotalSeq-A-labeled CD49a (, BioLegend),
1010 TotalSeq-A-labeled CD49a (HMα1, BioLegend), TotalSeq-A-labeled NKp46 (29A1.4,
1011 BioLegend), TotalSeq-A-labeled CD4 (RM4-5, BioLegend), TotalSeq-A-labeled ST2 (DIH9,
1012 BioLegend), TotalSeq-A-labeled CD25 (PC61, BioLegend), TotalSeq-A-labeled CD45.1 (A20,
1013 BioLegend), TotalSeq-A-labeled CD45.2 (104, BioLegend), TotalSeq-A-labeled CD8a (53-6.7,
1014 BioLegend), TotalSeq-A-labeled CXCR5 (L138D7, BioLegend), TotalSeq-A-labeled CCR6 (29-
1015 2L17, BioLegend), and anti-mouse TotalSeq-A Hashtag antibody (4-6; BioLegend). The
1016 enriched samples were then stained with APC-labeled Streptavidin (BioLegend) for 15 minutes

on ice before being stained with Sytox Green Dead Cell Stain (Thermo Fisher Scientific). ILCs (Lineage$^-$ IL-7Ra$^+$ CD90.2$^+$ CD45.1$^+$ or CD45.2$^+$ cells) were sort purified using a 100 µm sorting chip in a 4 laser SH-800 cell sorter (Sony) on the purity setting.

Single cell RNA: Library generation and sequencing. The v3.1 chemistry Chromium Single Cell 3' Reagent Kit (10X Genomics) was used to generate scRNA-seq libraries using the CITE-seq protocol[48] modifications for the myeloid, T, and innate lymphoid cell libraries and the standard 10X protocol for the stromal cell library. The myeloid cell dataset required three lanes of a Chromium Next GEM Chip, with lane 1 containing naïve cells, lane 2 containing *Mtb*-infected cells, and lane 3 containing the bystander cells from the 3 *Acod1*$^{-/-}$ and 3 *Nos2*$^{-/-}$ mice. Each lane was super-loaded with ~34,000 cells for a target of 17,000 single cells per lane at a multiplet rate of 3%[133]. The stromal cell dataset used 4 lanes of a Chromium Next GEM Chip, with lane 1 containing *Il1r1*$^{-/-}$ stromal cells from *Mtb*-infected mice, lane 2 containing *Il1r1*$^{-/-}$ stromal cells from naïve mice, lane 3 containing wild-type stromal cells from *Mtb*-infected mice, and lane 4 containing wild-type stromal cells from naïve mice. Each lane was loaded with 12,500 cells for an expected yield of 7,000 single cells at a multiplet rate of 5%. The T cell and ILC libraries were generated using the same Chromium Next GEM Chip, with lane 1 containing T cells and lane 2 containing ILCs from *Mtb*-infected mixed BM chimera mice. 25,000 cells were super-loaded into each lane with a target capture of 13,200 cells at a multiplet rate of 4%[133]. For the CITE-seq libraries, 0.5 U/µL RNaseOUT Recombinant Ribonuclease Inhibitor (Invitrogen) was added to single cell RT master mix during the loading step and 1 µL of ADT and HTO additive primers (0.2 µM stock) were added during the cDNA amplification. All samples were decontaminated by 2 rounds of centrifugation through 0.2 µM filter microcentrifuge tubes following cDNA, ADT, and HTO purification and then removed from the BSL3. The CITE-seq protocol was used to complete the ADT and HTO libraries while the 10X Genomics protocol was followed for the cDNA library. Quality control of the libraries was performed with a Fragment Analyzer (Agilent). Libraries were pooled and then sequenced on a NovaSeq 6000 (Illumina) using an S1 flow cell and the following cycles read 1 (28 cycles), i7 index (10 cycles), i5 index (10 cycles), read 2 (90 cycles).

ScRNA-seq: data processing. Sequencing reads of the mRNA libraries were mapped to the mouse genome with CellRanger version 6.0.0 (10X Genomics), while the raw count matrices for the ADT and HTO libraries were generated with CITE-Seq-Count version 1.4.3[134]. The count matrices were analyzed with Seurat v4.3.0[47] using default settings for normalizing the data, finding variable features, and scaling the data. For CITE-seq datasets, multiplets were excluded through HTO demultiplexing using the HTODemux function. The myeloid cell dataset was filtered to include cells with between 200 and 4500 genes and less than 5% mitochondrial reads. The T cell, ILC, and stromal cell datasets were filtered to only include cells that have between 200 and 2500 genes and less than 5% mitochondrial reads. The resulting myeloid dataset as well as our previously published scRNA-seq datasets for myeloid cells in *Mtb*-infected and naïve B6 and *Sp140*$^{-/-}$ mice (GSE216023) were integrated together and then clustered with a resolution of 1.5. The T cell and ILC datasets were analyzed with the default Seurat workflow using weighted nearest neighbor multimodal analysis to cluster cells based on mRNA and protein expression at a resolution of 1. The stromal cell dataset was also analyzed with Seurat using integration to combine the *Mtb*-infected and naïve WT and *Il1r1*$^{-/-}$ datasets and then clustering the cells based on mRNA expression using a resolution of 1.5.

Bulk RNA-seq, Gene signature and ROC curve analysis. Our previously published signatures for type I IFN and IFN-γ[15] were applied to our myeloid cell scRNA-seq dataset to score cells based on their gene expression using the UCell package[135]. Signatures for the B6, *Nos2*$^{-/-}$, *Acod1*$^{-/-}$, and *Sp140*$^{-/-}$ mice were generated in R[136] by identifying genes induced at

least 8-fold in the myeloid cells from *Mtb*-infected mice relative to naïve animals for each genotype. A corresponding human signature was produced using the convert_mouse_to_human_symbols from the NichetNetr package[72]. The hacksig package using the singscore statistical method[137] was applied to calculate a signature score based on each signature's expression in the TANDEM cohort PBMC RNA-seq data[49], Berry South Africa RNA-seq data[50], or the Bloom et al. microarray data[51]. The pROC package[138] was used to generate the ROC curves and calculate the area under the curve to quantify the ability of each signature to discriminate between the active *Mtb* cases and healthy controls in the TANDEM cohort, between active *Mtb* cases and LTBI individuals in the Berry South Africa dataset, and between active *Mtb* cases and lung cancer or pneumonia in the Bloom et al. dataset. The hacksig and pROC packages were also used to test the predictive ability of a gene signature consisting of known immunosuppressive genes (*IL1RN*, *IL18BP*, *CD274*, *TGFB1*, *IDO1*, *IL10*, and *ARG1*) on the TANDEM cohort. The pROC package was also used to determine the ability of *IL1RN* expression to identify active *Mtb* cases in the TANDEM cohort and the Berry South Africa dataset. The DESeq2 package[139] was used to analyze *IL1RN* expression in human PBMCs from *Mtb*-infected or healthy control individuals in the TANDEM cohort as well as to analyze *IL1RN* expression relative to time prior to TB diagnosis in the progressor portion of the Adolescent Cohort Study[63].

NicheNet analysis of IL-1-regulated signaling. IL-1-regulated genes were defined as genes expressed at least 2-fold higher in WT than *Il1r1*$^{-/-}$ cells in the T cell, innate lymphoid cell, and stromal cell scRNA-seq datasets. These IL-1-regulated genes were used as the potential ligands for NicheNet analysis[72]. The receiver cells were defined as IMs, *Trem2*$^{+}$ IMs, and *Spp1*$^{+}$ IMs from the myeloid cell scRNA-seq dataset. The expressed receptors on the receiver cells were identified using the get_expressed_genes function from NicheNet with a 10% cutoff for expression and then filtering the NicheNet receptor database to those genes expressed in the IM populations. Ligand activity in the receiver cells was calculated by identifying genes upregulated in *Trem2*$^{+}$ or *Spp1*$^{+}$ IMs relative to the IM cell population via the FindMarkers function from the Seurat package[47], focusing on genes upregulated at least 2-fold and with an adjusted p value less than 0.05, as calculated by the Wilcoxon Rank-Sum test with Bonferroni correction. The ability of each IL-1-regulated ligand to induce the genes upregulated in *Trem2*$^{+}$ or *Spp1*$^{+}$ IMs was determined by NicheNet's predict_ligand_activities function.

Statistical analysis. Statistical significance was determined using Prism (GraphPad) software for unpaired or paired two-tailed Student t test when comparing two populations, or one-way ANOVA tests with Tukey's multiple comparisons test when comparing multiple groups. ROC curves and their AUC were calculated in R using the pROC package.

Data availability. Raw and processed single cell RNA-sequencing data is deposited at NCBI Gene Expression Omnibus: GSE255213, GSE254983, and GSE254926.

Code availability. Code for scRNA-sequencing analysis is available on Github: https://github.com/dmitrikotov/IL-1Ra-TB.

Supplementary Figure Legends

Supplementary Figure 1. Classifying myeloid scRNA-seq clusters and comparing myeloid cells from naïve *Sp140*-, *Nos2*-, and *Acod1*-deficient mouse lungs. Dot plot of lineage of markers used to (**A**) identify myeloid cell clusters and (**B**) define neutrophil cluster heterogeneity. (**C**) The myeloid populations in the naïve lungs of B6, *Nos2*$^{-/-}$, *Acod1*$^{-/-}$, and

1119 *Sp140*$^{-/-}$ mice (n = 3 per genotype). (**D**) Number of shared and unique genes differentially
1120 expressed (2-fold change and adjusted p value < 0.05) between by neutrophils, alveolar
1121 macrophages, monocytes, and interstitial macrophages in *Nos2*$^{-/-}$, *Acod1*$^{-/-}$, and *Sp140*$^{-/-}$
1122 relative to those from B6 mice. Statistical significance in (D) was calculated with the Wilcoxon
1123 Rank-Sum test with Bonferroni correction.
1124
1125 **Supplementary Figure 2. Mouse gene signatures consisting of genes upregulated in**
1126 **myeloid cells following *Mtb* infection of B6, *Sp140*$^{-/-}$, *Acod1*$^{-/-}$, or *Nos2*$^{-/-}$ mice**
1127 **discriminate active *Mtb* infection from Cancer and Pneumonia in humans.** (**A**) A heatmap
1128 depicting the $\log_2$ fold change of gene upregulation following *Mtb* infection relative to the gene's
1129 expression in myeloid cells from naïve lungs. The heatmap compares gene expression for
1130 signature genes between B6, *Nos2*$^{-/-}$, *Acod1*$^{-/-}$, and *Sp140*$^{-/-}$ mice (n = 3 per genotype). Grey
1131 boxes indicate genes not present in the gene signature of a given mouse genotype. Genes in
1132 blue indicate those with known immunosuppressive function. (**B**) ROC curves of the ability of
1133 genes induced by *Mtb* infection in B6, *Nos2*$^{-/-}$, *Acod1*$^{-/-}$, or *Sp140*$^{-/-}$ mice to stratify human
1134 active *Mtb* patients (n = 35) and individuals with lung cancer (n = 16) or Pneumonia (n = 19) in
1135 the Bloom et al. cohort (analysis of GSE42834).
1136
1137 **Supplementary Figure 3. Classifying scRNA-seq clusters for *Mtb*-infected non-human**
1138 **primate and human lung datasets.** Dot plot of lineage of markers used to identify cell clusters
1139 in (**A**) *Mtb*-infected non-human primate and (**B**) human lungs.
1140
1141 **Supplementary Figure 4. Conservation of genes preferentially expressed by *Spp1*$^{+}$ IMs**
1142 **relative to *Trem2*$^{+}$ IMs in *Mtb*-infected susceptible mice and humans.** (**A**) Venn diagram
1143 depicting the number of genes preferentially expressed (2-fold change and adjusted p value <
1144 0.05) by *Spp1*$^{+}$ IMs relative to *Trem2*$^{+}$ IMs in *Mtb*-infected B6, *Nos2*$^{-/-}$, *Acod1*$^{-/-}$, and *Sp140*$^{-/-}$
1145 mouse lungs (n = 3 per genotype) and human lungs (analysis of GSE192483). (**B**) Core gene
1146 signature for genes commonly expressed by *Spp1*$^{+}$ IMs in all three susceptible mouse models
1147 as well as those expressed by the three susceptible mouse models and humans.
1148
1149 **Supplementary Figure 5. IL-1Ra expression in mice and humans.** (**A**) Myeloid cell
1150 expression of *Il1r2* and *Il1rn* in naïve and *Mtb*-infected lungs from B6, *Nos2*$^{-/-}$, *Acod1*$^{-/-}$, and
1151 *Sp140*$^{-/-}$ mice (n = 3 mice per genotype for naïve lungs and 3 mice per genotype for *Mtb*-
1152 infected lungs) as measured by scRNA-seq. (**B**) *Il1rn* expression in myeloid cells from the lungs
1153 of B6, *Nos2*$^{-/-}$, *Acod1*$^{-/-}$, and *Sp140*$^{-/-}$ mice (n = 3 mice per genotype for naïve lungs and 3 mice
1154 per genotype for *Mtb*-infected lungs). (**C**) Normalized *IL1RN* expression in *Mtb*-infected (n =
1155 151) and healthy individuals (n = 98) from the TANDEM cohort (analysis of GSE114192). (**D**)
1156 ROC curve of the predictive ability of an immunosuppressive gene signature applied to the
1157 TANDEM cohort. (**E**) *IL1RN* expression plotted relative to time before clinical diagnosis of *Mtb*
1158 infection in the progressor population of the Adolescent Cohort Study (n = 74) with the blue line
1159 indicating local polynomial regression fitting using the loess method and grey indicating the
1160 confidence interval. Day 200 prior to diagnosis (red line) indicates the timepoint *IL1RN*
1161 expression started to increase in patients as they approached diagnosis (analysis of
1162 GSE79362). Statistical significance in (C) was calculated using the Wald test and corrected for
1163 multiple testing using the Benjamini and Hochberg method.
1164
1165 **Supplementary Figure 6. Flow cytometric identification of monocyte and monocyte-**
1166 **derived macrophage subsets identified by scRNA-seq.** (**A**) Overview of monocyte and
1167 interstitial macrophage subsets and (**B**) their expression of subset identifying markers as
1168 measured by scRNA-seq of *Mtb*-infected lungs from B6, *Nos2*$^{-/-}$, *Acod1*$^{-/-}$, and *Sp140*$^{-/-}$ mice (n

= 3 mice per genotype). (**C**) Myeloid cell flow cytometry gating strategy. (**D**) Frequency of *Mtb*-infected cells among the major myeloid cell populations.

Supplementary Figure 7. Myeloid cells express very little IL-1 receptor and IM as well as neuronal expression of IL-1 receptor does not impact bacterial control in a cell-intrinsic manner. (**A**) The myeloid populations identified by scRNA-seq and (**B**) *Il1r1* expression in myeloid cells from the lungs of B6, *Nos2*$^{-/-}$, *Acod1*$^{-/-}$, and *Sp140*$^{-/-}$ mice (n = 3 mice per genotype for naïve lungs and 3 mice per genotype for *Mtb*-infected lungs). (**C**) Mixed BM chimera schematic, (**D**) representative flow plot, and (**E**) quantification of the frequency of *Mtb* infection among lung wild-type CD45.1^{+} and *Il1r1*$^{-/-}$ CD45.1^{-} IMs (n = 8) 25 days post-infection. (**F**) Experimental setup and (**G**) lung bacterial burden of bone marrow chimera mice with wild-type neurons (CD45.1 host, n = 13), littermate control neurons (Adv$^{+/+}$ Il1r1$^{fl/fl}$ host, n = 9), and IL-1 receptor-deficient neurons (Adv$^{Cre/+}$ Il1r1$^{fl/fl}$ host, n = 14) 25 days after *Mtb* infection. Pooled data from two independent experiments is shown in (E) and (G). Statistical significance in (E) was calculated with a paired t test and in (G) with a one-way ANOVA with Tukey's multiple comparison test.

Supplementary Figure 8. Classifying T cell, ILC, and stromal cell scRNA-seq clusters. Dot plot of lineage of markers used to annotate the clusters in our (**A**) T cell dataset, (**B**) ILC dataset, and (**C**) stromal cell dataset**.**

Supplementary Figure 9. NicheNet analysis of IL-1 regulated ligands that could activate interstitial macrophages. (**A**) List of IL-1 regulated potential ligands identified in stromal and hematopoietic cells. (**B**) Receptor expression on interstitial macrophages for the IL-1-regulated ligands. (**C**) Predicted ligand activity based on genes differently expressed by the activated interstitial macrophage subsets.

References

1. WHO. Global Tuberculosis Report 2024. https://www.who.int/teams/global-tuberculosis-programme/tb-reports/global-tuberculosis-report-2024.
2. Davenne, T. & McShane, H. Why don't we have an effective tuberculosis vaccine yet? *Expert Rev Vaccines* **15**, 1009–1013 (2016).
3. Cooper, A. M. *et al.* Disseminated tuberculosis in interferon gamma gene-disrupted mice. *J Exp Med* **178**, 2243–2247 (1993).
4. Flynn, J. L. *et al.* An essential role for interferon gamma in resistance to Mycobacterium tuberculosis infection. *J Exp Med* **178**, 2249–2254 (1993).
5. Flynn, J. L. *et al.* Tumor necrosis factor-alpha is required in the protective immune response against Mycobacterium tuberculosis in mice. *Immunity* **2**, 561–572 (1995).
6. Cohen, S. B., Gern, B. H. & Urdahl, K. B. The Tuberculous Granuloma and Preexisting Immunity. *Annual Review of Immunology* **40**, 589–614 (2022).
7. Russell, D. G., Barry, C. E. & Flynn, J. L. Tuberculosis: What We Don't Know Can, and Does, Hurt Us. *Science* **328**, 852–856 (2010).
8. Berry, M. P. R. *et al.* An interferon-inducible neutrophil-driven blood transcriptional signature in human tuberculosis. *Nature* **466**, 973–977 (2010).
9. Saqib, M. *et al.* Hematopoietic dysregulation caused by neutrophils underlies impaired T-cell response and enhanced susceptibility to tuberculosis. Preprint at https://doi.org/10.21203/rs.3.rs-2921835/v1 (2023).

1218 10. McNab, F. W. *et al.* TPL-2-ERK1/2 signaling promotes host resistance against
1219 intracellular bacterial infection by negative regulation of type I IFN production. *J Immunol*
1220 **191**, 1732–1743 (2013).
1221 11. Moreira-Teixeira, L. *et al.* T Cell-Derived IL-10 Impairs Host Resistance to
1222 Mycobacterium tuberculosis Infection. *J Immunol* **199**, 613–623 (2017).
1223 12. Stanley, S. A., Johndrow, J. E., Manzanillo, P. & Cox, J. S. The Type I IFN response to
1224 infection with Mycobacterium tuberculosis requires ESX-1-mediated secretion and
1225 contributes to pathogenesis. *J Immunol* **178**, 3143–3152 (2007).
1226 13. Mishra, B. B. *et al.* Nitric oxide prevents a pathogen permissive granulocytic
1227 inflammation during tuberculosis. *Nat Microbiol* **2**, 17072 (2017).
1228 14. Ji, D. X. *et al.* Role of the transcriptional regulator SP140 in resistance to bacterial
1229 infections via repression of type I interferons. *eLife* **10**, e67290 (2021).
1230 15. Kotov, D. I. *et al.* Early cellular mechanisms of type I interferon-driven susceptibility to
1231 tuberculosis. *Cell* **186**, 5536-5553.e22 (2023).
1232 16. Witt, K. C. *et al.* The SP140-RESIST pathway regulates interferon mRNA stability and
1233 antiviral immunity. 2024.08.28.610186 Preprint at https://doi.org/10.1101/2024.08.28.610186
1234 (2024).
1235 17. Ji, D. X. *et al.* Type I interferon-driven susceptibility to Mycobacterium tuberculosis is
1236 mediated by interleukin-1 receptor antagonist IL-1Ra. *Nat Microbiol* **4**, 2128–2135 (2019).
1237 18. Pichugin, A. V., Yan, B.-S., Sloutsky, A., Kobzik, L. & Kramnik, I. Dominant role of the
1238 sst1 locus in pathogenesis of necrotizing lung granulomas during chronic tuberculosis
1239 infection and reactivation in genetically resistant hosts. *Am J Pathol* **174**, 2190–2201 (2009).
1240 19. Pan, H. *et al.* Ipr1 gene mediates innate immunity to tuberculosis. *Nature* **434**, 767–772
1241 (2005).
1242 20. MacMicking, J. D. *et al.* Identification of nitric oxide synthase as a protective locus
1243 against tuberculosis. *Proc Natl Acad Sci U S A* **94**, 5243–5248 (1997).
1244 21. Nair, S. *et al.* Irg1 expression in myeloid cells prevents immunopathology during M.
1245 tuberculosis infection. *Journal of Experimental Medicine* **215**, 1035–1045 (2018).
1246 22. Moreira-Teixeira, L. *et al.* Type I IFN exacerbates disease in tuberculosis-susceptible
1247 mice by inducing neutrophil-mediated lung inflammation and NETosis. *Nat Commun* **11**,
1248 5566 (2020).
1249 23. Bohrer, A. C., Tocheny, C., Assmann, M., Ganusov, V. V. & Mayer-Barber, K. D.
1250 Cutting Edge: IL-1R1 Mediates Host Resistance to Mycobacterium tuberculosis by Trans-
1251 Protection of Infected Cells. *J Immunol* **201**, 1645–1650 (2018).
1252 24. Eruslanov, E. B. *et al.* Neutrophil Responses to Mycobacterium tuberculosis Infection in
1253 Genetically Susceptible and Resistant Mice. *Infect Immun* **73**, 1744–1753 (2005).
1254 25. Mattila, J. T., Maiello, P., Sun, T., Via, L. E. & Flynn, J. L. Granzyme B-expressing
1255 neutrophils correlate with bacterial load in granulomas from Mycobacterium tuberculosis-
1256 infected cynomolgus macaques. *Cell Microbiol* **17**, 1085–1097 (2015).
1257 26. Gideon, H. P., Phuah, J., Junecko, B. A. & Mattila, J. T. Neutrophils express pro- and
1258 anti-inflammatory cytokines in granulomas from Mycobacterium tuberculosis-infected
1259 cynomolgus macaques. *Mucosal Immunol* **12**, 1370–1381 (2019).
1260 27. Meier, S. *et al.* Neutrophil degranulation, NETosis and platelet degranulation pathway
1261 genes are co-induced in whole blood up to six months before tuberculosis diagnosis. *PLoS*
1262 *One* **17**, e0278295 (2022).

1263 28. Eum, S.-Y. *et al.* Neutrophils are the predominant infected phagocytic cells in the
1264 airways of patients with active pulmonary TB. *Chest* **137**, 122–128 (2010).
1265 29. Lovewell, R. R., Baer, C. E., Mishra, B. B., Smith, C. M. & Sassetti, C. M. Granulocytes
1266 act as a niche for Mycobacterium tuberculosis growth. *Mucosal Immunol* **14**, 229–241 (2021).
1267 30. Dallenga, T. *et al.* M. tuberculosis-Induced Necrosis of Infected Neutrophils Promotes
1268 Bacterial Growth Following Phagocytosis by Macrophages. *Cell Host Microbe* **22**, 519-
1269 530.e3 (2017).
1270 31. Chowdhury, C. S. *et al.* Type I IFN signaling mediates NET release to promote
1271 Mycobacterium tuberculosis replication and granuloma caseation. 2022.11.29.518376 Preprint
1272 at https://doi.org/10.1101/2022.11.29.518376 (2022).
1273 32. Herrero-Cervera, A., Soehnlein, O. & Kenne, E. Neutrophils in chronic inflammatory
1274 diseases. *Cell Mol Immunol* **19**, 177–191 (2022).
1275 33. Mishra, B. B. *et al.* Nitric oxide controls the immunopathology of tuberculosis by
1276 inhibiting NLRP3 inflammasome-dependent processing of IL-1β. *Nat Immunol* **14**, 52–60
1277 (2013).
1278 34. Law, K. *et al.* Increased release of interleukin-1 beta, interleukin-6, and tumor necrosis
1279 factor-alpha by bronchoalveolar cells lavaged from involved sites in pulmonary tuberculosis.
1280 *Am J Respir Crit Care Med* **153**, 799–804 (1996).
1281 35. Zhang, G. *et al.* Allele-specific induction of IL-1β expression by C/EBPβ and PU.1
1282 contributes to increased tuberculosis susceptibility. *PLoS Pathog* **10**, e1004426 (2014).
1283 36. Mayer-Barber, K. D. *et al.* Host-directed therapy of tuberculosis based on interleukin-1
1284 and type I interferon crosstalk. *Nature* **511**, 99–103 (2014).
1285 37. Mayer-Barber, K. D. *et al.* Cutting Edge: Caspase-1 Independent IL-1β Production Is
1286 Critical for Host Resistance to Mycobacterium tuberculosis and Does Not Require TLR
1287 Signaling In Vivo. *J Immunol* **184**, 3326–3330 (2010).
1288 38. Mayer-Barber, K. D. *et al.* Innate and Adaptive Interferons Suppress IL-1α and IL-1β
1289 Production by Distinct Pulmonary Myeloid Subsets during Mycobacterium tuberculosis
1290 Infection. *Immunity* **35**, 1023–1034 (2011).
1291 39. Di Paolo, N. C. *et al.* Interdependence between interleukin-1 and tumor necrosis factor
1292 controls TNF-dependent effector functions during Mycobacterium tuberculosis infection.
1293 *Immunity* **43**, 1125–1136 (2015).
1294 40. Juffermans, N. P. *et al.* Interleukin-1 Signaling Is Essential for Host Defense during
1295 Murine Pulmonary Tuberculosis. *The Journal of Infectious Diseases* **182**, 902–908 (2000).
1296 41. Bloom, C. I. *et al.* Detectable Changes in The Blood Transcriptome Are Present after
1297 Two Weeks of Antituberculosis Therapy. *PLOS ONE* **7**, e46191 (2012).
1298 42. Blankley, S. *et al.* A 380-gene meta-signature of active tuberculosis compared with
1299 healthy controls. *European Respiratory Journal* **47**, 1873–1876 (2016).
1300 43. Kwan, P. K. W. *et al.* A blood RNA transcript signature for TB exposure in household
1301 contacts. *BMC Infectious Diseases* **20**, 403 (2020).
1302 44. Kimmey, J. M. *et al.* Unique role for ATG5 in PMN-mediated immunopathology during
1303 M. tuberculosis infection. *Nature* **528**, 565–569 (2015).
1304 45. Yeremeev, V., Linge, I., Kondratieva, T. & Apt, A. Neutrophils exacerbate tuberculosis
1305 infection in genetically susceptible mice. *Tuberculosis (Edinb)* **95**, 447–451 (2015).
1306 46. Huynh, J. P. *et al.* Bhlhe40 is an essential repressor of IL-10 during Mycobacterium
1307 tuberculosis infection. *Journal of Experimental Medicine* **215**, 1823–1838 (2018).

1308 47. Hao, Y. *et al.* Integrated analysis of multimodal single-cell data. *Cell* **184**, 3573-3587.e29
1309 (2021).
1310 48. Stoeckius, M. *et al.* Simultaneous epitope and transcriptome measurement in single cells.
1311 *Nat Methods* **14**, 865–868 (2017).
1312 49. Eckold, C. *et al.* Impact of Intermediate Hyperglycemia and Diabetes on Immune
1313 Dysfunction in Tuberculosis. *Clin Infect Dis* **72**, 69–78 (2020).
1314 50. Singhania, A. *et al.* A modular transcriptional signature identifies phenotypic
1315 heterogeneity of human tuberculosis infection. *Nat Commun* **9**, 2308 (2018).
1316 51. Bloom, C. I. *et al.* Transcriptional Blood Signatures Distinguish Pulmonary Tuberculosis,
1317 Pulmonary Sarcoidosis, Pneumonias and Lung Cancers. *PLOS ONE* **8**, e70630 (2013).
1318 52. Marcovecchio, P. M., Thomas, G. & Salek-Ardakani, S. CXCL9-expressing tumor-
1319 associated macrophages: new players in the fight against cancer. *J Immunother Cancer* **9**,
1320 e002045 (2021).
1321 53. Matsubara, E. *et al.* SPP1 Derived from Macrophages Is Associated with a Worse
1322 Clinical Course and Chemo-Resistance in Lung Adenocarcinoma. *Cancers (Basel)* **14**, 4374
1323 (2022).
1324 54. Bill, R. *et al.* CXCL9:SPP1 macrophage polarity identifies a network of cellular
1325 programs that control human cancers. *Science* **381**, 515–524 (2023).
1326 55. Wang, D. *et al.* The association between osteopontin and tuberculosis: A systematic
1327 review and meta-analysis. *PLoS One* **15**, e0242702 (2020).
1328 56. Yang, Q. *et al.* The interaction of macrophages and CD8 T cells in bronchoalveolar
1329 lavage fluid is associated with latent tuberculosis infection. *Emerging Microbes & Infections*
1330 **12**, 2239940 (2023).
1331 57. Katano, H., Hebisawa, A., Sato, Y. & Hoshino, Y. Identification of SPP1-positive
1332 macrophages by single-cell spatial analysis in human lung tissues with mycobacterial
1333 infection. 2024.09.12.612778 Preprint at https://doi.org/10.1101/2024.09.12.612778 (2025).
1334 58. McColl, S. R., Paquin, R., Ménard, C. & Beaulieu, A. D. Human neutrophils produce
1335 high levels of the interleukin 1 receptor antagonist in response to granulocyte/macrophage
1336 colony-stimulating factor and tumor necrosis factor alpha. *Journal of Experimental Medicine*
1337 **176**, 593–598 (1992).
1338 59. Winchell, C. G. *et al.* CD8+ lymphocytes are critical for early control of tuberculosis in
1339 macaques. *Journal of Experimental Medicine* **220**, e20230707 (2023).
1340 60. Zhou, T. *et al.* IL-18BP is a secreted immune checkpoint and barrier to IL-18
1341 immunotherapy. *Nature* **583**, 609–614 (2020).
1342 61. Jiang, X. *et al.* Role of the tumor microenvironment in PD-L1/PD-1-mediated tumor
1343 immune escape. *Molecular Cancer* **18**, 10 (2019).
1344 62. Mittal, S. K., Cho, K.-J., Ishido, S. & Roche, P. A. Interleukin 10 (IL-10)-mediated
1345 Immunosuppression. *J Biol Chem* **290**, 27158–27167 (2015).
1346 63. Zak, D. E. *et al.* A blood RNA signature for tuberculosis disease risk: a prospective
1347 cohort study. *The Lancet* **387**, 2312–2322 (2016).
1348 64. Scriba, T. J. *et al.* Sequential inflammatory processes define human progression from M.
1349 tuberculosis infection to tuberculosis disease. *PLOS Pathogens* **13**, e1006687 (2017).
1350 65. Yu, J. *et al.* Early-stage idiopathic pulmonary fibrosis is characterized by bronchoalveolar
1351 accumulation of SPP1+ macrophages. 2023.12.06.569201 Preprint at
1352 https://doi.org/10.1101/2023.12.06.569201 (2023).

1353 66. Gander-Bui, H. T. T. *et al.* Targeted removal of macrophage-secreted interleukin-1
1354 receptor antagonist protects against lethal Candida albicans sepsis. *Immunity* **56**, 1743-
1355 1760.e9 (2023).
1356 67. Scott, C. L. *et al.* The Transcription Factor ZEB2 Is Required to Maintain the Tissue-
1357 Specific Identities of Macrophages. *Immunity* **49**, 312-325.e5 (2018).
1358 68. Lamacchia, C., Palmer, G., Seemayer, C. A., Talabot-Ayer, D. & Gabay, C. Enhanced
1359 Th1 and Th17 responses and arthritis severity in mice with a deficiency of myeloid cell–
1360 specific interleukin-1 receptor antagonist. *Arthritis & Rheumatism* **62**, 452–462 (2010).
1361 69. Jain, A., Song, R., Wakeland, E. K. & Pasare, C. T cell-intrinsic IL-1R signaling licenses
1362 effector cytokine production by memory CD4 T cells. *Nat Commun* **9**, 3185 (2018).
1363 70. Ohne, Y. *et al.* IL-1 is a critical regulator of group 2 innate lymphoid cell function and
1364 plasticity. *Nat Immunol* **17**, 646–655 (2016).
1365 71. Zhou, L. *et al.* Innate lymphoid cells support regulatory T cells in the intestine through
1366 interleukin-2. *Nature* **568**, 405–409 (2019).
1367 72. Browaeys, R., Saelens, W. & Saeys, Y. NicheNet: modeling intercellular communication
1368 by linking ligands to target genes. *Nat Methods* **17**, 159–162 (2020).
1369 73. Mailhot, B. *et al.* Neuronal interleukin-1 receptors mediate pain in chronic inflammatory
1370 diseases. *J Exp Med* **217**, e20191430 (2020).
1371 74. Liu, X. *et al.* Cell-Type-Specific Interleukin 1Receptor 1 Signaling in the Brain
1372 Regulates Distinct Neuroimmune Activities. *Immunity* **50**, 317-333.e6 (2019).
1373 75. Hurskainen, M. *et al.* Single cell transcriptomic analysis of murine lung development on
1374 hyperoxia-induced damage. *Nat Commun* **12**, 1565 (2021).
1375 76. Huang, L., Nazarova, E. V., Tan, S., Liu, Y. & Russell, D. G. Growth of Mycobacterium
1376 tuberculosis in vivo segregates with host macrophage metabolism and ontogeny. *Journal of*
1377 *Experimental Medicine* **215**, 1135–1152 (2018).
1378 77. Ardain, A. *et al.* Group 3 innate lymphoid cells mediate early protective immunity
1379 against tuberculosis. *Nature* **570**, 528–532 (2019).
1380 78. Gopal, R. *et al.* Unexpected Role for IL-17 in Protective Immunity against Hypervirulent
1381 Mycobacterium tuberculosis HN878 Infection. *PLOS Pathogens* **10**, e1004099 (2014).
1382 79. Van Dis, E. *et al.* STING-Activating Adjuvants Elicit a Th17 Immune Response and
1383 Protect against Mycobacterium tuberculosis Infection. *Cell Rep* **23**, 1435–1447 (2018).
1384 80. Jong, R. M. *et al.* Mucosal Vaccination with Cyclic Dinucleotide Adjuvants Induces
1385 Effective T Cell Homing and IL-17-Dependent Protection against Mycobacterium
1386 tuberculosis Infection. *J Immunol* **208**, 407–419 (2022).
1387 81. Alcorn, J. F. IL-22 Plays a Critical Role in Maintaining Epithelial Integrity During
1388 Pulmonary Infection. *Front Immunol* **11**, 1160 (2020).
1389 82. Coussens, L. M. & Werb, Z. Inflammation and cancer. *Nature* **420**, 860–867 (2002).
1390 83. Ostrand-Rosenberg, S. & Sinha, P. Myeloid-Derived Suppressor Cells: Linking
1391 Inflammation and Cancer. *J Immunol* **182**, 4499–4506 (2009).
1392 84. Barbosa Bomfim, C. C. *et al.* Harmful Effects of Granulocytic Myeloid-Derived
1393 Suppressor Cells on Tuberculosis Caused by Hypervirulent Mycobacteria. *J Infect Dis* **223**,
1394 494–507 (2021).
1395 85. Tsiganov, E. N. *et al.* Gr-1dimCD11b+ immature myeloid-derived suppressor cells but
1396 not neutrophils are markers of lethal tuberculosis infection in mice. *J Immunol* **192**, 4718–
1397 4727 (2014).

1398 86. La Manna, M. P. *et al.* Mycobacterium tuberculosis Drives Expansion of Low-Density
1399 Neutrophils Equipped With Regulatory Activities. *Front Immunol* **10**, 2761 (2019).
1400 87. Knaul, J. K. *et al.* Lung-residing myeloid-derived suppressors display dual functionality
1401 in murine pulmonary tuberculosis. *Am J Respir Crit Care Med* **190**, 1053–1066 (2014).
1402 88. Huang, B. *et al.* Gr-1+CD115+ immature myeloid suppressor cells mediate the
1403 development of tumor-induced T regulatory cells and T-cell anergy in tumor-bearing host.
1404 *Cancer Res* **66**, 1123–1131 (2006).
1405 89. du Plessis, N. *et al.* Increased frequency of myeloid-derived suppressor cells during
1406 active tuberculosis and after recent mycobacterium tuberculosis infection suppresses T-cell
1407 function. *Am J Respir Crit Care Med* **188**, 724–732 (2013).
1408 90. Singh, B. *et al.* Myeloid-Derived Suppressor Cells Mediate T Cell Dysfunction in
1409 Nonhuman Primate TB Granulomas. *mBio* **12**, e0318921 (2021).
1410 91. Ashenafi, S. & Brighenti, S. Reinventing the human tuberculosis (TB) granuloma:
1411 Learning from the cancer field. *Front Immunol* **13**, 1059725 (2022).
1412 92. Gern, B. H. *et al.* TGFβ restricts expansion, survival, and function of T cells within the
1413 tuberculous granuloma. *Cell Host & Microbe* **29**, 594-606.e6 (2021).
1414 93. McCaffrey, E. F. *et al.* The immunoregulatory landscape of human tuberculosis
1415 granulomas. *Nat Immunol* **23**, 318–329 (2022).
1416 94. Barber, D. L., Mayer-Barber, K. D., Feng, C. G., Sharpe, A. H. & Sher, A. CD4 T cells
1417 promote rather than control tuberculosis in the absence of PD-1-mediated inhibition. *J*
1418 *Immunol* **186**, 1598–1607 (2011).
1419 95. Kauffman, K. D. *et al.* PD-1 blockade exacerbates Mycobacterium tuberculosis infection
1420 in rhesus macaques. *Sci Immunol* **6**, eabf3861 (2021).
1421 96. Blumenthal, A. *et al.* M. tuberculosis Induces Potent Activation of IDO-1, but This Is Not
1422 Essential for the Immunological Control of Infection. *PLoS One* **7**, e37314 (2012).
1423 97. Gautam, U. S. *et al.* In vivo inhibition of tryptophan catabolism reorganizes the
1424 tuberculoma and augments immune-mediated control of Mycobacterium tuberculosis.
1425 *Proceedings of the National Academy of Sciences* **115**, E62–E71 (2018).
1426 98. Singh, B. *et al.* Inhibition of indoleamine dioxygenase leads to better control of
1427 tuberculosis adjunctive to chemotherapy. *JCI Insight* **8**, e163101.
1428 99. Jung, Y.-J., Ryan, L., LaCourse, R. & North, R. J. Increased interleukin-10 expression is
1429 not responsible for failure of T helper 1 immunity to resolve airborne Mycobacterium
1430 tuberculosis infection in mice. *Immunology* **109**, 295–299 (2003).
1431 100. North, R. J. Mice incapable of making IL-4 or IL-10 display normal resistance to
1432 infection with Mycobacterium tuberculosis. *Clinical and Experimental Immunology* **113**, 55–
1433 58 (1998).
1434 101. Higgins, D. M. *et al.* Lack of IL-10 alters inflammatory and immune responses during
1435 pulmonary Mycobacterium tuberculosis infection. *Tuberculosis* **89**, 149–157 (2009).
1436 102. Beamer, G. L. *et al.* Interleukin-10 Promotes Mycobacterium tuberculosis Disease
1437 Progression in CBA/J Mice1. *The Journal of Immunology* **181**, 5545–5550 (2008).
1438 103. Redford, P. S. *et al.* Enhanced protection to Mycobacterium tuberculosis infection in IL-
1439 10-deficient mice is accompanied by early and enhanced Th1 responses in the lung. *European*
1440 *Journal of Immunology* **40**, 2200–2210 (2010).
1441 104. Martinez, L. *et al.* Cytomegalovirus acquisition in infancy and the risk of tuberculosis
1442 disease in childhood: a longitudinal birth cohort study in Cape Town, South Africa. *The*
1443 *Lancet Global Health* **9**, e1740–e1749 (2021).

1444 105. Müller, J. *et al.* Cytomegalovirus infection is a risk factor for tuberculosis disease in
1445 infants. *JCI Insight* **4**, 130090 (2019).
1446 106. Walaza, S. *et al.* Influenza virus infection is associated with increased risk of death
1447 amongst patients hospitalized with confirmed pulmonary tuberculosis in South Africa, 2010–
1448 2011. *BMC Infectious Diseases* **15**, 26 (2015).
1449 107. Antonelli, L. R. V. *et al.* Intranasal Poly-IC treatment exacerbates tuberculosis in mice
1450 through the pulmonary recruitment of a pathogen-permissive monocyte/macrophage
1451 population. *J Clin Invest* **120**, 1674–1682 (2010).
1452 108. Kang, T. G. *et al.* Viral coinfection promotes tuberculosis immunopathogenesis by type I
1453 IFN signaling-dependent impediment of Th1 cell pulmonary influx. *Nat Commun* **13**, 3155
1454 (2022).
1455 109. Redford, P. S. *et al.* Influenza A Virus Impairs Control of Mycobacterium tuberculosis
1456 Coinfection Through a Type I Interferon Receptor–Dependent Pathway. *J Infect Dis* **209**,
1457 270–274 (2014).
1458 110. Volkert, M., Pierce, C., Horsfall, F. L. & Dubos, R. J. THE ENHANCING EFFECT OF
1459 CONCURRENT INFECTION WITH PNEUMOTROPIC VIRUSES ON PULMONARY
1460 TUBERCULOSIS IN MICE. *J Exp Med* **86**, 203–214 (1947).
1461 111. Xu, W. *et al.* Early innate and adaptive immune perturbations determine long-term
1462 severity of chronic virus and Mycobacterium tuberculosis coinfection. *Immunity* **54**, 526-
1463 541.e7 (2021).
1464 112. Ring, S. *et al.* Blocking IL-10 receptor signaling ameliorates Mycobacterium tuberculosis
1465 infection during influenza-induced exacerbation. *JCI Insight* **5**, e126533, 126533 (2019).
1466 113. MacDonald, L. *et al.* COVID-19 and RA share an SPP1 myeloid pathway that drives PD-
1467 L1+ neutrophils and CD14+ monocytes. *JCI Insight* **6**, e147413.
1468 114. Dinarello, C. A. Overview of the IL-1 family in innate inflammation and acquired
1469 immunity. *Immunol Rev* **281**, 8–27 (2018).
1470 115. Chensue, S. W., Warmington, K. S., Berger, A. E. & Tracey, D. E. Immunohistochemical
1471 demonstration of interleukin-1 receptor antagonist protein and interleukin-1 in human
1472 lymphoid tissue and granulomas. *Am J Pathol* **140**, 269–275 (1992).
1473 116. Settas, L. D., Tsimirikas, G., Vosvotekas, G., Triantafyllidou, E. & Nicolaides, P.
1474 Reactivation of pulmonary tuberculosis in a patient with rheumatoid arthritis during treatment
1475 with IL-1 receptor antagonists (anakinra). *J Clin Rheumatol* **13**, 219–220 (2007).
1476 117. Winchell, C. G. *et al.* Evaluation of IL-1 Blockade as an Adjunct to Linezolid Therapy
1477 for Tuberculosis in Mice and Macaques. *Frontiers in Immunology* **11**, (2020).
1478 118. Liu, X., Boyer, M. A., Holmgren, A. M. & Shin, S. Legionella-Infected Macrophages
1479 Engage the Alveolar Epithelium to Metabolically Reprogram Myeloid Cells and Promote
1480 Antibacterial Inflammation. *Cell Host Microbe* **28**, 683-698.e6 (2020).
1481 119. Rothchild, A. C. *et al.* Role of Granulocyte-Macrophage Colony-Stimulating Factor
1482 Production by T Cells during Mycobacterium tuberculosis Infection. *mBio* **8**,
1483 10.1128/mbio.01514-17 (2017).
1484 120. Gonzalez-Juarrero, M. *et al.* Disruption of granulocyte macrophage-colony stimulating
1485 factor production in the lungs severely affects the ability of mice to control Mycobacterium
1486 tuberculosis infection. *J Leukoc Biol* **77**, 914–922 (2005).
1487 121. Dis, E. V. *et al.* IFN-γ-independent control of M. tuberculosis requires CD4 T cell-
1488 derived GM-CSF and activation of HIF-1α. *PLOS Pathogens* **18**, e1010721 (2022).

1489 122. Mayer-Barber, K. D. Granulocytes subsets and their divergent functions in host resistance
1490 to Mycobacterium tuberculosis - a 'tipping-point' model of disease exacerbation. *Curr Opin*
1491 *Immunol* **84**, 102365 (2023).
1492 123. Müller, U. *et al.* Functional role of type I and type II interferons in antiviral defense.
1493 *Science* **264**, 1918–1921 (1994).
1494 124. Shen, F. W. *et al.* Cloning of Ly-5 cDNA. *Proc Natl Acad Sci U S A* **82**, 7360–7363
1495 (1985).
1496 125. Glaccum, M. B. *et al.* Phenotypic and functional characterization of mice that lack the
1497 type I receptor for IL-1. *J Immunol* **159**, 3364–3371 (1997).
1498 126. Robson, M. J. *et al.* Generation and Characterization of Mice Expressing a Conditional
1499 Allele of the Interleukin-1 Receptor Type 1. *PLoS One* **11**, e0150068 (2016).
1500 127. Zhou, X. *et al.* Deletion of PIK3C3/Vps34 in sensory neurons causes rapid
1501 neurodegeneration by disrupting the endosomal but not the autophagic pathway. *Proc Natl*
1502 *Acad Sci U S A* **107**, 9424–9429 (2010).
1503 128. Laubach, V. E., Shesely, E. G., Smithies, O. & Sherman, P. A. Mice lacking inducible
1504 nitric oxide synthase are not resistant to lipopolysaccharide-induced death. *Proc Natl Acad Sci*
1505 *U S A* **92**, 10688–10692 (1995).
1506 129. Takaki, K., Davis, J. M., Winglee, K. & Ramakrishnan, L. Evaluation of the pathogenesis
1507 and treatment of Mycobacterium marinum infection in zebrafish. *Nat Protoc* **8**, 1114–1124
1508 (2013).
1509 130. Kotov, D. I., Pengo, T., Mitchell, J. S., Gastinger, M. J. & Jenkins, M. K. Chrysalis: A
1510 New Method for High-Throughput Histo-Cytometry Analysis of Images and Movies. *The*
1511 *Journal of Immunology* **202**, 300–308 (2019).
1512 131. Gerner, M. Y., Kastenmuller, W., Ifrim, I., Kabat, J. & Germain, R. N. Histo-cytometry:
1513 a method for highly multiplex quantitative tissue imaging analysis applied to dendritic cell
1514 subset microanatomy in lymph nodes. *Immunity* **37**, 364–376 (2012).
1515 132. Anderson, K. G. *et al.* Intravascular staining for discrimination of vascular and tissue
1516 leukocytes. *Nat Protoc* **9**, 209–222 (2014).
1517 133. Stoeckius, M. *et al.* Cell Hashing with barcoded antibodies enables multiplexing and
1518 doublet detection for single cell genomics. *Genome Biology* **19**, 224 (2018).
1519 134. Roelli, P., bbimber, Flynn, B., santiagorevale & Gui, G. Hoohm/CITE-seq-Count: 1.4.2.
1520 Zenodo https://doi.org/10.5281/zenodo.2590196 (2019).
1521 135. Andreatta, M. & Carmona, S. J. UCell: Robust and scalable single-cell gene signature
1522 scoring. *Comput Struct Biotechnol J* **19**, 3796–3798 (2021).
1523 136. R Core Team. R: A language and environment for statistical computing. R Foundation
1524 for Statistical Computing (2021).
1525 137. Foroutan, M. *et al.* Single sample scoring of molecular phenotypes. *BMC Bioinformatics*
1526 **19**, 404 (2018).
1527 138. Robin, X. *et al.* pROC: an open-source package for R and S+ to analyze and compare
1528 ROC curves. *BMC Bioinformatics* **12**, 77 (2011).
1529 139. Love, M. I., Huber, W. & Anders, S. Moderated estimation of fold change and dispersion
1530 for RNA-seq data with DESeq2. *Genome Biol* **15**, 550 (2014).
1531

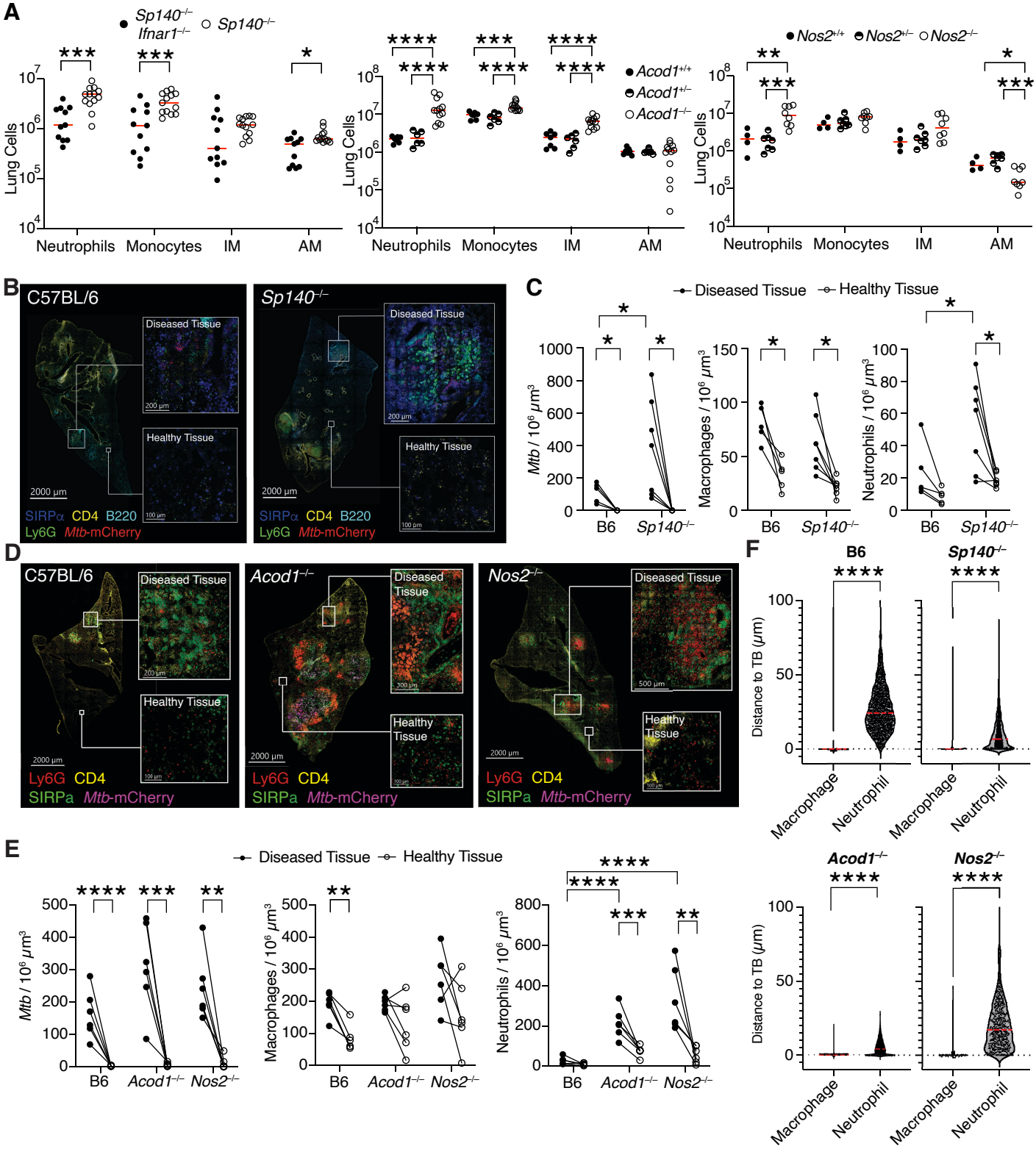
A
Sp140−/− Ifnar1−/−
Sp140−/−
Lung Cells
Neutrophils
Monocytes
IM
AM
Acod1+/+
Acod1+/−
Acod1−/−
Nos2+/+
Nos2+/−
Nos2−/−
B
C57BL/6
Sp140−/−
Diseased Tissue
Healthy Tissue
2000 µm
SIRPα CD4 B220
Ly6G Mtb-mCherry
C
Diseased Tissue
Healthy Tissue
Mtb / 10^6 µm^3
Macrophages / 10^6 µm^3
Neutrophils / 10^6 µm^3
B6
Sp140−/−
D
C57BL/6
Acod1−/−
Nos2−/−
Ly6G CD4
SIRPa Mtb-mCherry
E
Diseased Tissue
Healthy Tissue
Mtb / 10^6 µm^3
Macrophages / 10^6 µm^3
Neutrophils / 10^6 µm^3
B6
Acod1−/−
Nos2−/−
F
B6
Sp140−/−
Acod1−/−
Nos2−/−
Distance to TB (µm)
Macrophage
Neutrophil

Figure 1.

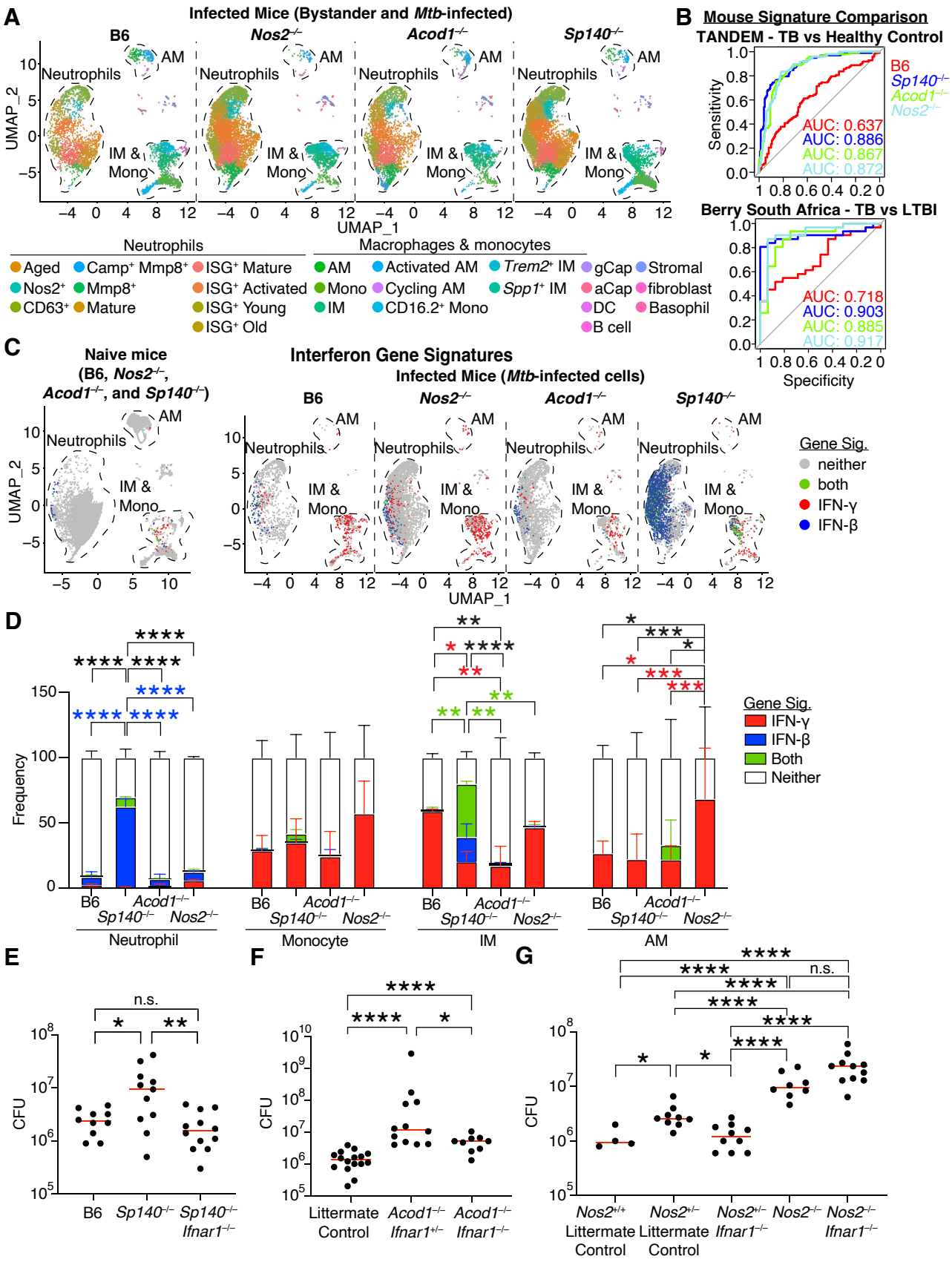
A
Infected Mice (Bystander and Mtb-infected)
B6
Nos2-/-
Acod1-/-
Sp140-/-
AM
Neutrophils
IM & Mono
UMAP_2
UMAP_1
Neutrophils
Aged
Camp+ Mmp8+
ISG+ Mature
Nos2+
Mmp8+
ISG+ Activated
CD63+
Mature
ISG+ Young
ISG+ Old
Macrophages & monocytes
AM
Activated AM
Trem2+ IM
Mono
Cycling AM
Spp1+ IM
IM
CD16.2+ Mono
gCap
Stromal
aCap
fibroblast
DC
Basophil
B cell
B
Mouse Signature Comparison
TANDEM - TB vs Healthy Control
Sensitivity
B6
Sp140-/-
Acod1-/-
Nos2-/-
AUC: 0.637
AUC: 0.886
AUC: 0.867
AUC: 0.872
Berry South Africa - TB vs LTBI
AUC: 0.718
AUC: 0.903
AUC: 0.885
AUC: 0.917
Specificity
C
Naive mice
(B6, Nos2-/-,
Acod1-/-, and Sp140-/-)
Interferon Gene Signatures
Infected Mice (Mtb-infected cells)
Gene Sig.
neither
both
IFN-γ
IFN-β
D
Frequency
Gene Sig.
IFN-γ
IFN-β
Both
Neither
Neutrophil
Monocyte
IM
AM
E
CFU
n.s.
B6
Sp140-/-
Sp140-/-
Ifnar1-/-
F
Littermate
Control
Acod1-/-
Ifnar1+/-
Acod1-/-
Ifnar1-/-
G
Nos2+/+
Littermate
Control
Nos2+/-
Littermate
Control
Nos2+/-
Ifnar1-/-
Nos2-/-
Nos2-/-
Ifnar1-/-

Figure 2.

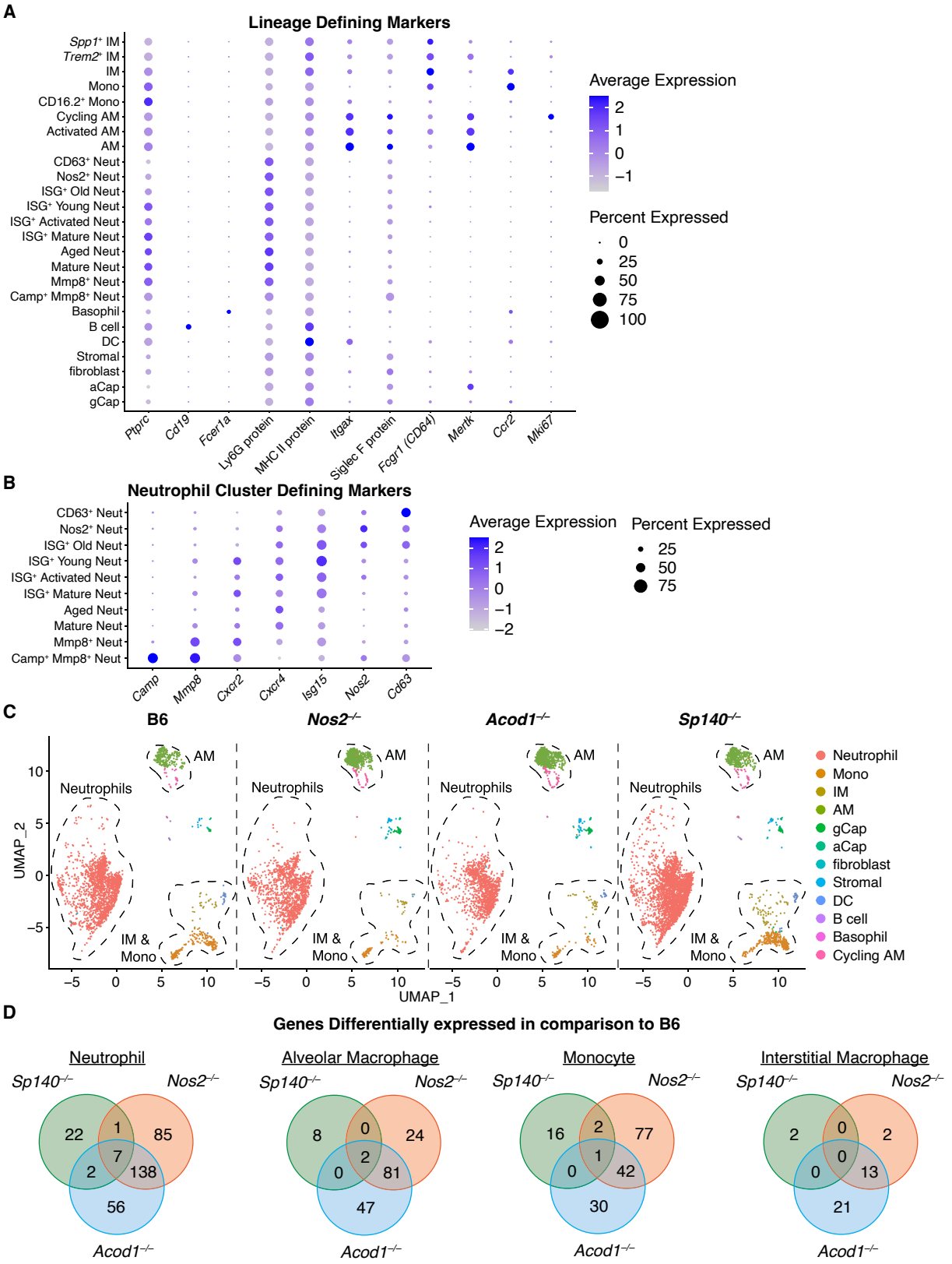

Supplementary Figure 1.

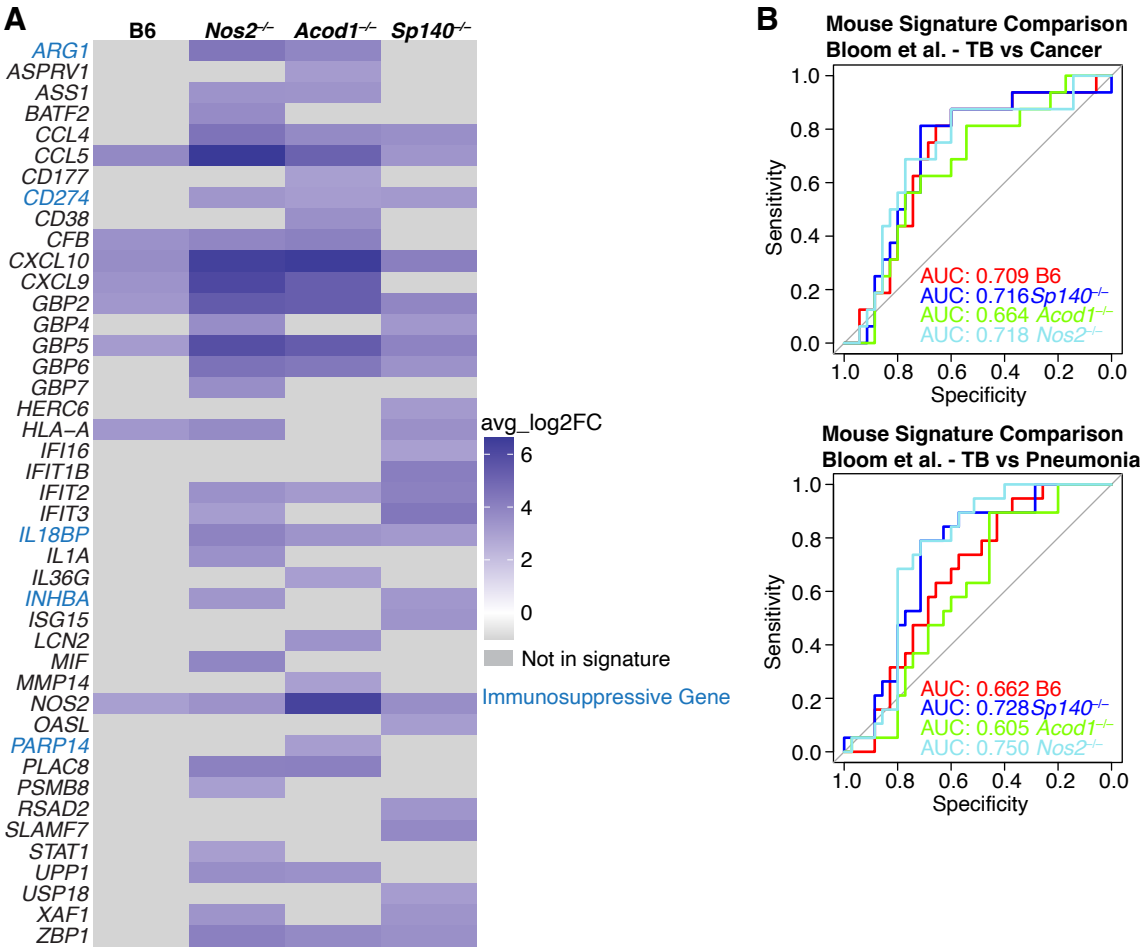

Supplementary Figure 2.

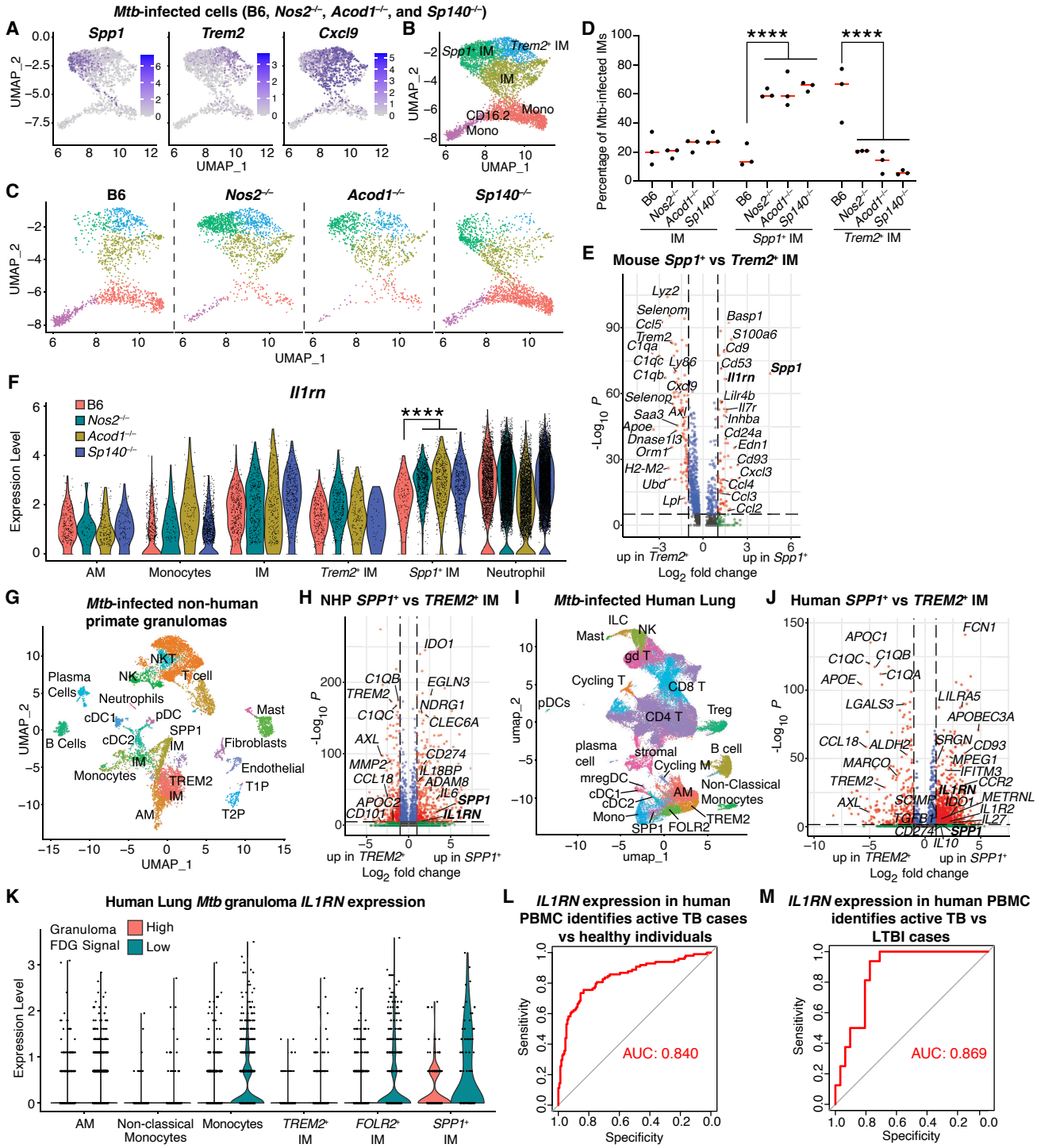
Mtb-infected cells (B6, Nos2-/-, Acod1-/-, and Sp140-/-)
A
Spp1
Trem2
Cxcl9
UMAP_2
UMAP_1
B
Spp1+ IM
Trem2+ IM
IM
Mono
CD16.2 Mono
C
B6
Nos2-/-
Acod1-/-
Sp140-/-
D
Percentage of Mtb-infected IMs
****
IM
Spp1+ IM
Trem2+ IM
E
Mouse Spp1+ vs Trem2+ IM
up in Trem2+
up in Spp1+
Log2 fold change
F
Il1rn
Expression Level
AM
Monocytes
IM
Trem2+ IM
Spp1+ IM
Neutrophil
G
Mtb-infected non-human primate granulomas
Plasma Cells
NK
NKT
T cell
Neutrophils
cDC1
pDC
B Cells
cDC2
SPP1 IM
Mast
Fibroblasts
Endothelial
Monocytes
TREM2 IM
T1P
AM
T2P
H
NHP SPP1+ vs TREM2+ IM
IDO1
C1QB
TREM2
C1QC
AXL
MMP2
CCL18
APOC2
CD101
EGLN3
NDRG1
CLEC6A
CD274
IL18BP
ADAM8
IL6
SPP1
IL1RN
I
Mtb-infected Human Lung
ILC
Mast
NK
gd T
Cycling T
CD8 T
pDCs
CD4 T
Treg
plasma cell
stromal
B cell
Cycling M
mregDC
cDC1
cDC2
Mono
AM
Non-Classical Monocytes
TREM2
SPP1 FOLR2
umap_1
umap_2
J
Human SPP1+ vs TREM2+ IM
FCN1
APOC1
C1QC
C1QB
C1QA
APOE
LILRA5
LGALS3
APOBEC3A
CCL18
ALDH2
SRGN
CD93
MARCO
MPEG1
IFITM3
TREM2
CCR2
IL1RN
METRNL
AXL
SCIMP
IDO1
IL1R2
TGFB1
IL27
CD274
SPP1
IL10
K
Human Lung Mtb granuloma IL1RN expression
Granuloma FDG Signal
High
Low
Expression Level
AM
Non-classical Monocytes
Monocytes
TREM2+ IM
FOLR2+ IM
SPP1+ IM
L
IL1RN expression in human PBMC identifies active TB cases vs healthy individuals
Sensitivity
Specificity
AUC: 0.840
M
IL1RN expression in human PBMC identifies active TB vs LTBI cases
AUC: 0.869

Figure 3.

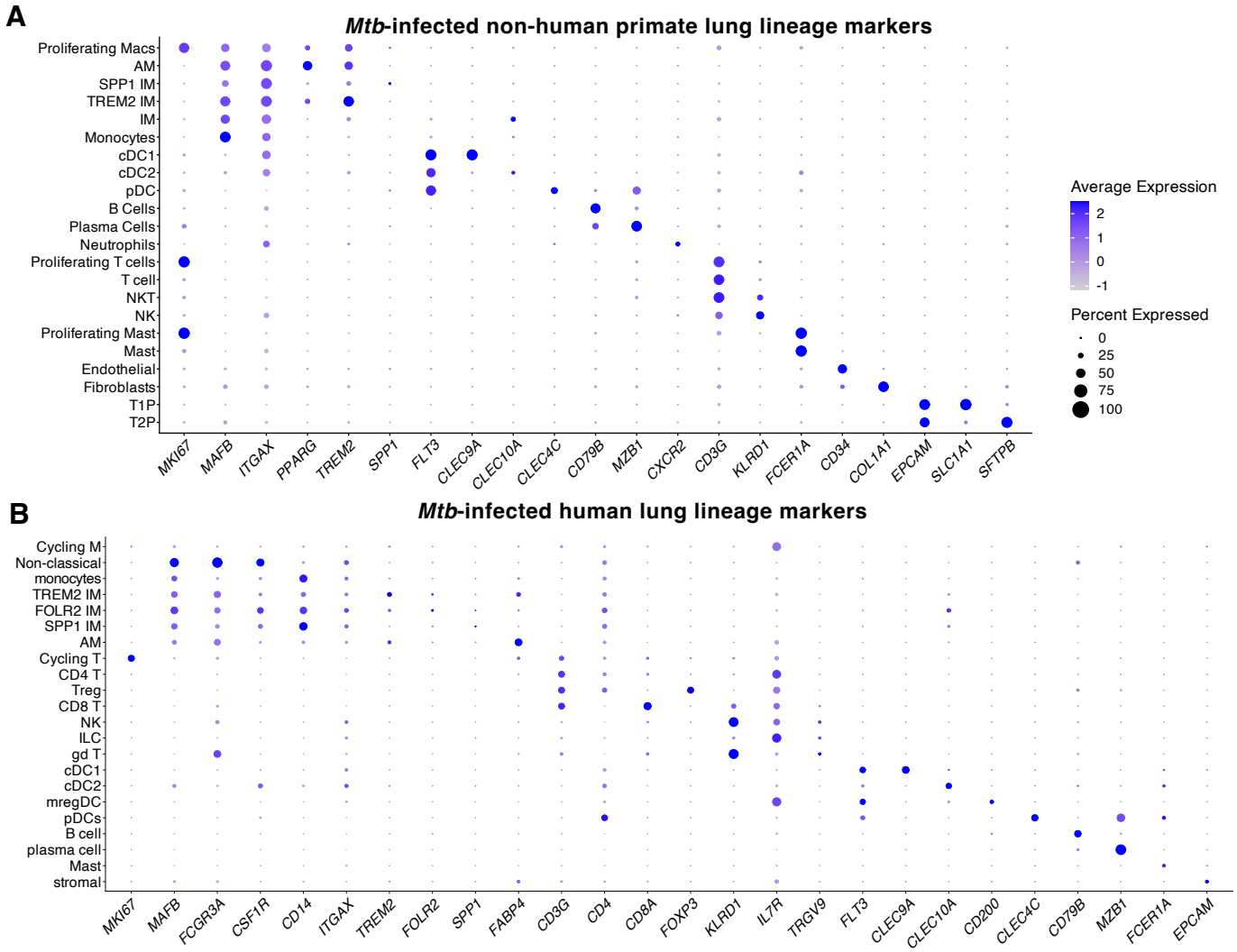

Supplementary Figure 3.

A

Mouse genes upregulated by *Spp1*⁺ IM relative to *Trem2*⁺ IM

Upregulated genes conserved between mouse and human

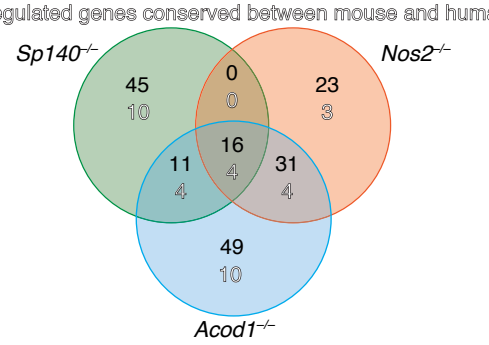

	Sp140⁻/⁻	*Nos2*⁻/⁻	*Acod1*⁻/⁻
Mouse genes:	72	70	107
Overlap with human SPP1⁺ IMs (genes):	18 (25%)	11 (16%)	22 (21%)

B

Core *Spp1*⁺ IM genes	
Upp1	Conserved across 3 mouse genotypes
S100a6	
Inhba	
Cd9	
AA467197	
Anxa2	
Fam129b	
Hilpda	
Cd24a	
Lilrb4	
Basp1	
Spp1	
Il1rn	Conserved across 3 mouse genotypes and humans
Srgn	
Metrnl	
Scimp	

Supplementary Figure 4.

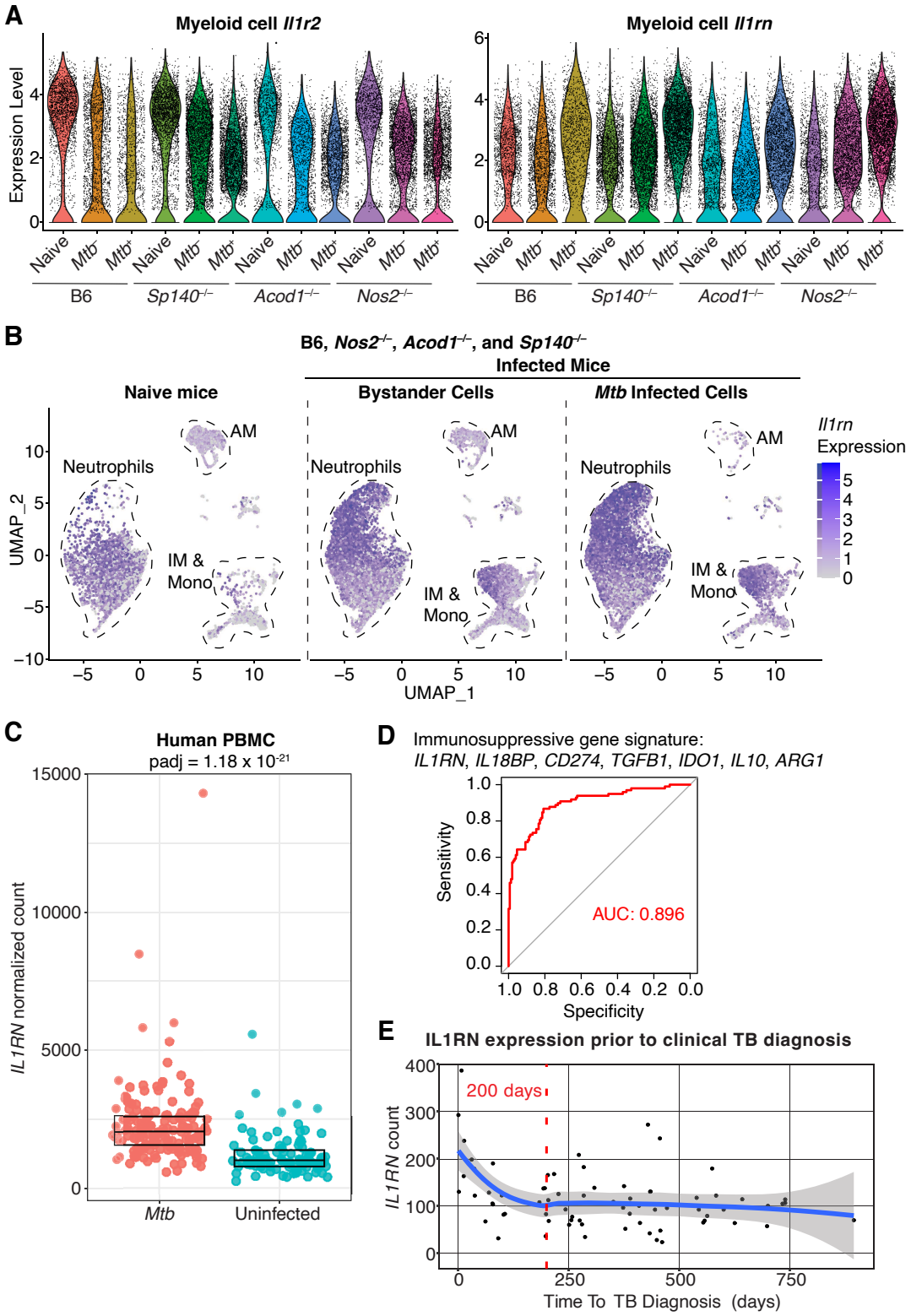

Supplementary Figure 5.

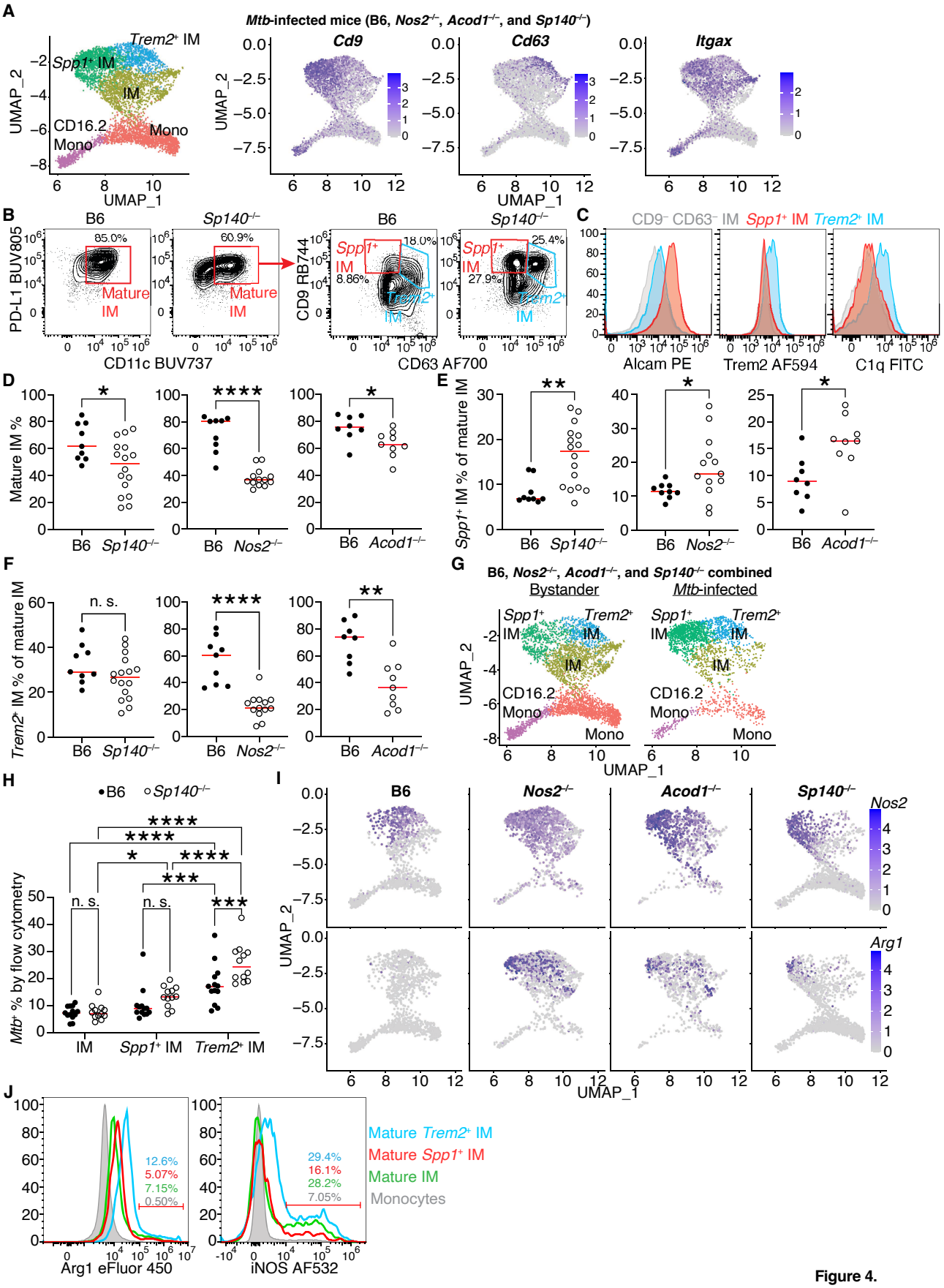
A
Mtb-infected mice (B6, Nos2-/-, Acod1-/-, and Sp140-/-)
Trem2+ IM
Spp1+ IM
IM
CD16.2 Mono
Mono
UMAP_2
UMAP_1
Cd9
Cd63
Itgax
B
B6
Sp140-/-
PD-L1 BUV805
CD11c BUV737
85.0%
60.9%
Mature IM
CD9 RB744
CD63 AF700
18.0%
8.86%
25.4%
27.9%
C
CD9- CD63- IM
Spp1+ IM
Trem2+ IM
Alcam PE
Trem2 AF594
C1q FITC
D
Mature IM %
B6
Sp140-/-
Nos2-/-
Acod1-/-
E
Spp1+ IM % of mature IM
F
Trem2+ IM % of mature IM
n. s.
G
B6, Nos2-/-, Acod1-/-, and Sp140-/- combined
Bystander
Mtb-infected
H
Mtb+ % by flow cytometry
IM
Spp1+ IM
Trem2+ IM
I
Nos2
Arg1
J
Arg1 eFluor 450
iNOS AF532
12.6%
5.07%
7.15%
0.50%
29.4%
16.1%
28.2%
7.05%
Mature Trem2+ IM
Mature Spp1+ IM
Mature IM
Monocytes

Figure 4.

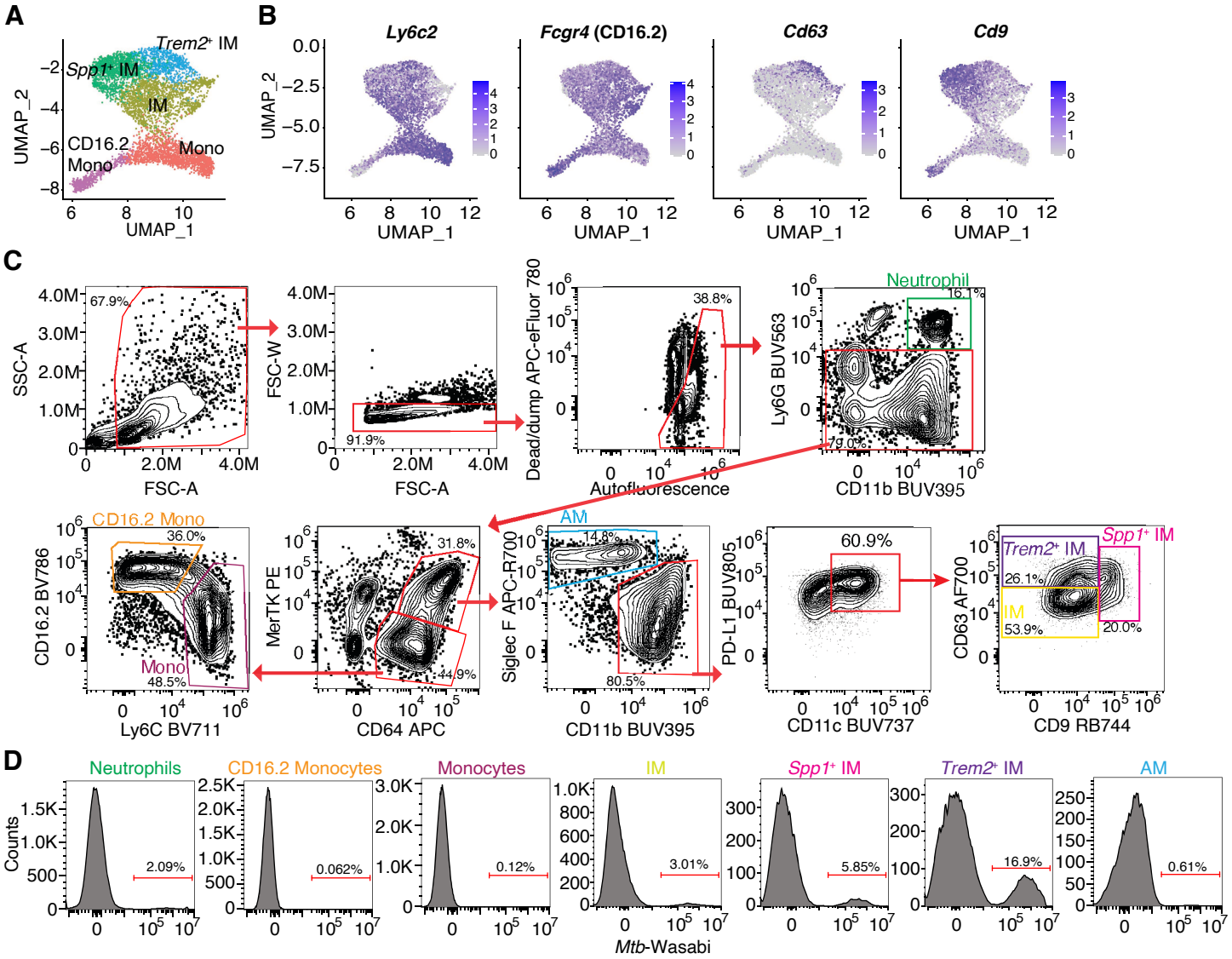

Supplementary Figure 6.

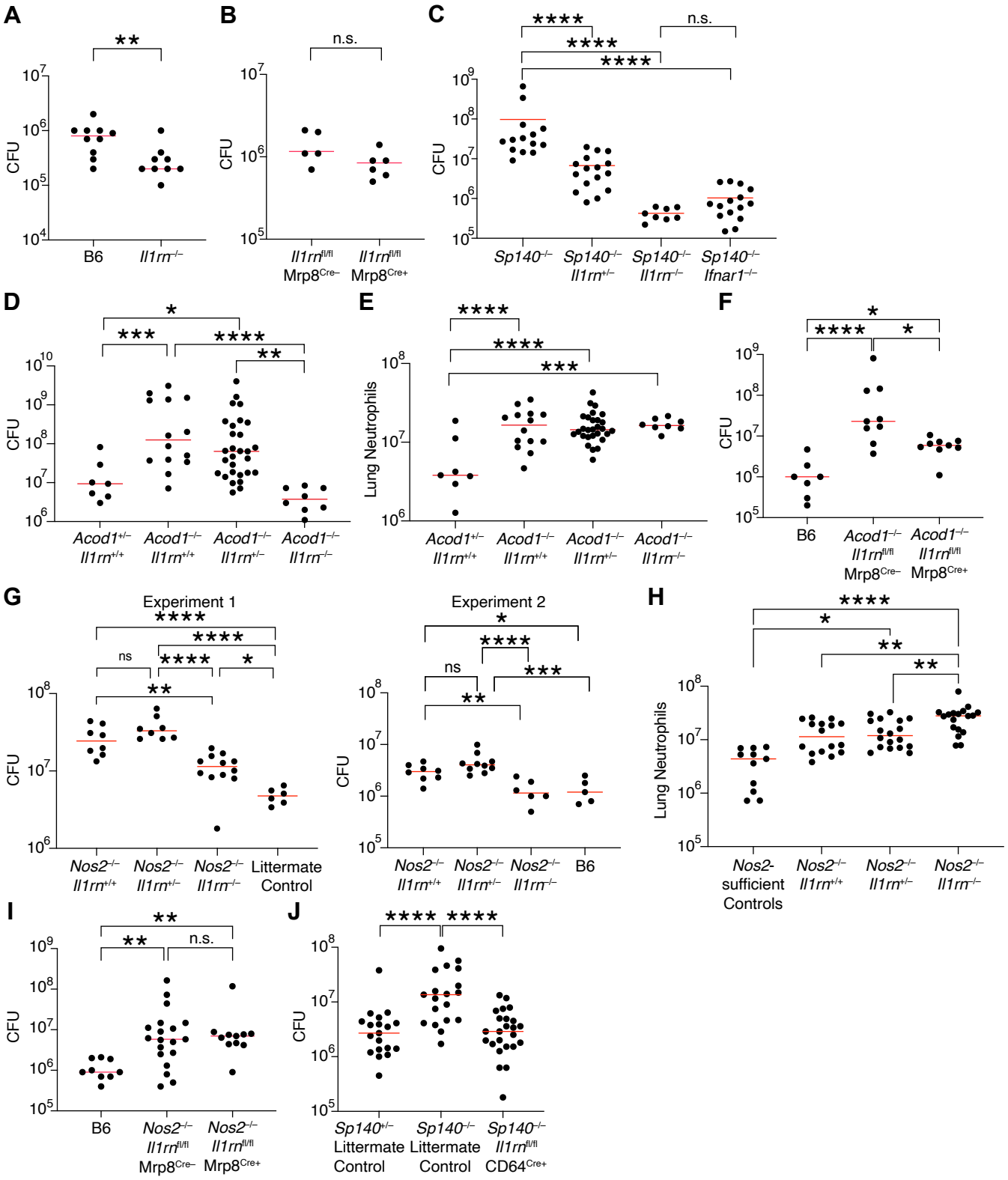
A
B
C
D
E
F
G
H
I
J
CFU
Lung Neutrophils
B6
Il1rn−/−
Il1rnfl/fl Mrp8Cre−
Il1rnfl/fl Mrp8Cre+
Sp140−/−
Sp140−/− Il1rn+/−
Sp140−/− Il1rn−/−
Sp140−/− Ifnar1−/−
Acod1+/− Il1rn+/+
Acod1−/− Il1rn+/+
Acod1−/− Il1rn+/−
Acod1−/− Il1rn−/−
Experiment 1
Experiment 2
Nos2−/− Il1rn+/+
Nos2−/− Il1rn+/−
Nos2−/− Il1rn−/−
Littermate Control
Nos2-sufficient Controls
Sp140+/− Littermate Control
Sp140−/− Littermate Control
Sp140−/− Il1rnfl/fl CD64Cre+
n.s.
ns

Figure 5.

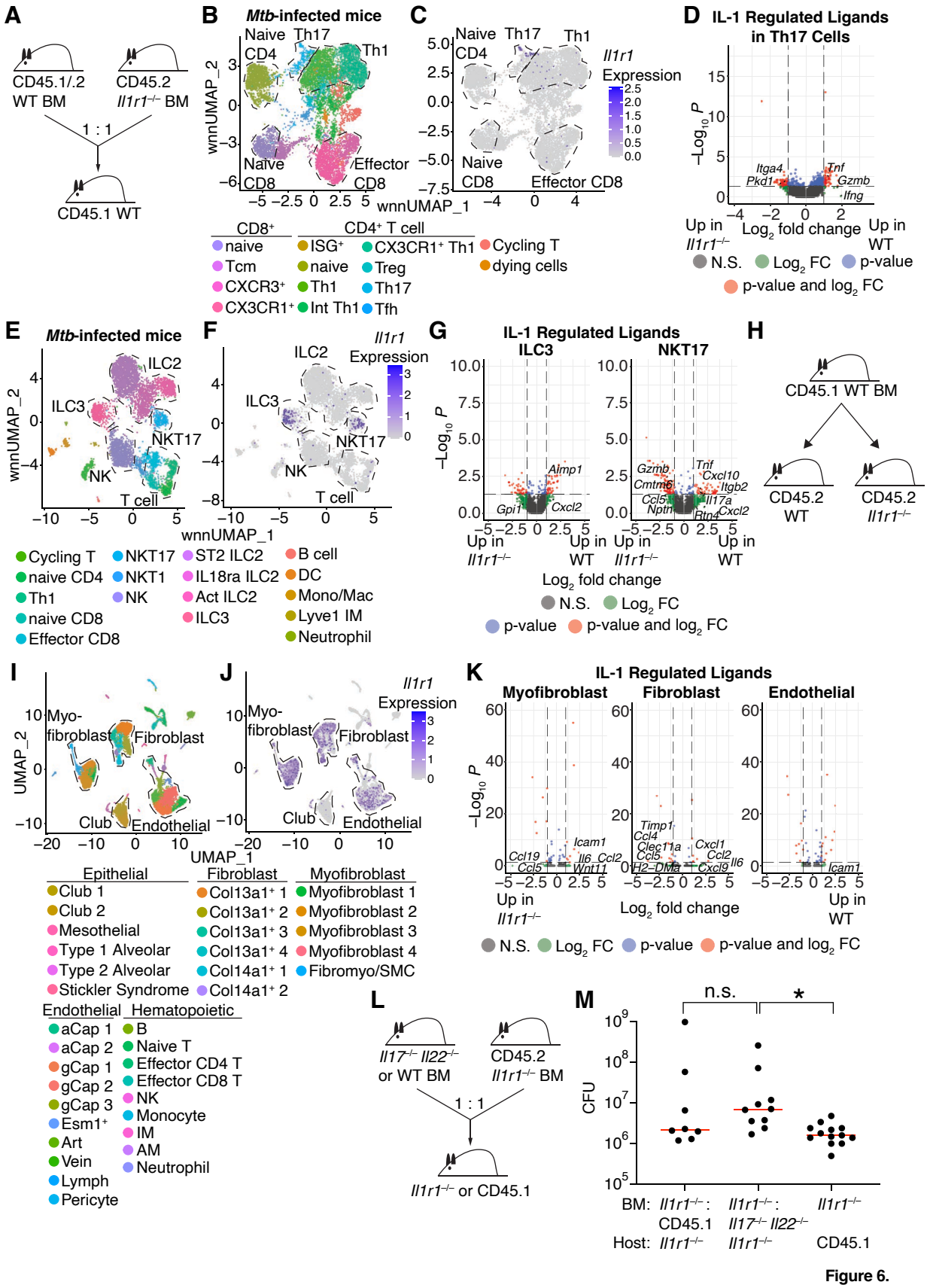
A
CD45.1/.2
WT BM
CD45.2
Il1r1−/− BM
1 : 1
CD45.1 WT
B
Mtb-infected mice
Naive CD4
Th17
Th1
Naive CD8
Effector CD8
wnnUMAP_2
wnnUMAP_1
C
Il1r1 Expression
Naive CD4
Th17
Th1
Naive CD8
Effector CD8
wnnUMAP_1
CD8+
naive
Tcm
CXCR3+
CX3CR1+
CD4+ T cell
ISG+
naive
Th1
Int Th1
CX3CR1+ Th1
Treg
Th17
Tfh
Cycling T
dying cells
D
IL-1 Regulated Ligands in Th17 Cells
−Log10 P
Itga4
Pkd1
Tnf
Gzmb
Ifng
Up in Il1r1−/−
Log2 fold change
Up in WT
N.S.
Log2 FC
p-value
p-value and log2 FC
E
Mtb-infected mice
ILC2
ILC3
NKT17
NK
T cell
wnnUMAP_2
F
Il1r1 Expression
ILC2
ILC3
NKT17
NK
T cell
wnnUMAP_1
Cycling T
naive CD4
Th1
naive CD8
Effector CD8
NKT17
NKT1
NK
ST2 ILC2
IL18ra ILC2
Act ILC2
ILC3
B cell
DC
Mono/Mac
Lyve1 IM
Neutrophil
G
IL-1 Regulated Ligands
ILC3
NKT17
−Log10 P
Almp1
Gpi1
Cxcl2
Gzmb
Cmtm6
Ccl5
Nptn
Tnf
Cxcl10
Itgb2
Il17a
Btn4
Cxcl2
Up in Il1r1−/−
Up in WT
Log2 fold change
N.S.
Log2 FC
p-value
p-value and log2 FC
H
CD45.1 WT BM
CD45.2 WT
CD45.2 Il1r1−/−
I
UMAP_2
Myo-fibroblast
Fibroblast
Club
Endothelial
UMAP_1
J
Il1r1 Expression
Myo-fibroblast
Fibroblast
Club
Endothelial
Epithelial
Club 1
Club 2
Mesothelial
Type 1 Alveolar
Type 2 Alveolar
Stickler Syndrome
Fibroblast
Col13a1+ 1
Col13a1+ 2
Col13a1+ 3
Col13a1+ 4
Col14a1+ 1
Col14a1+ 2
Myofibroblast
Myofibroblast 1
Myofibroblast 2
Myofibroblast 3
Myofibroblast 4
Fibromyo/SMC
Endothelial
aCap 1
aCap 2
gCap 1
gCap 2
gCap 3
Esm1+
Art
Vein
Lymph
Pericyte
Hematopoietic
B
Naive T
Effector CD4 T
Effector CD8 T
NK
Monocyte
IM
AM
Neutrophil
K
IL-1 Regulated Ligands
Myofibroblast
Fibroblast
Endothelial
−Log10 P
Ccl19
Ccl5
Icam1
Il6
Ccl2
Wnt11
Timp1
Ccl4
Clec11a
Ccl5
H2-DMa
Cxcl1
Ccl2
Cxcl9
Il6
Icam1
Up in Il1r1−/−
Log2 fold change
Up in WT
N.S.
Log2 FC
p-value
p-value and log2 FC
L
Il17−/− Il22−/− or WT BM
CD45.2 Il1r1−/− BM
1 : 1
Il1r1−/− or CD45.1
M
n.s.
*
CFU
BM: Il1r1−/− : CD45.1
Host: Il1r1−/−
Il1r1−/− : Il17−/− Il22−/−
Il1r1−/−
Il1r1−/−
CD45.1

Figure 6.

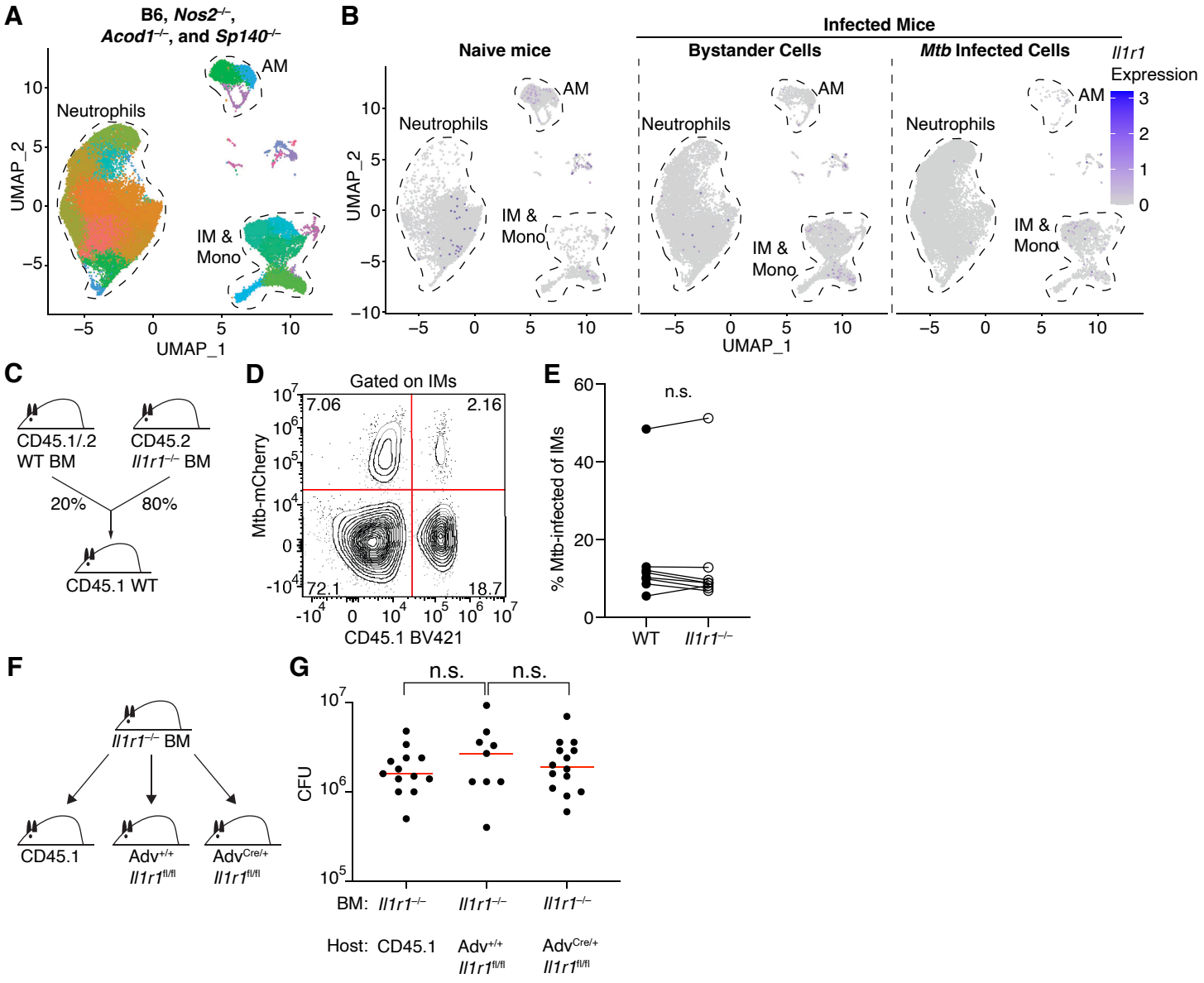

Supplementary Figure 7.

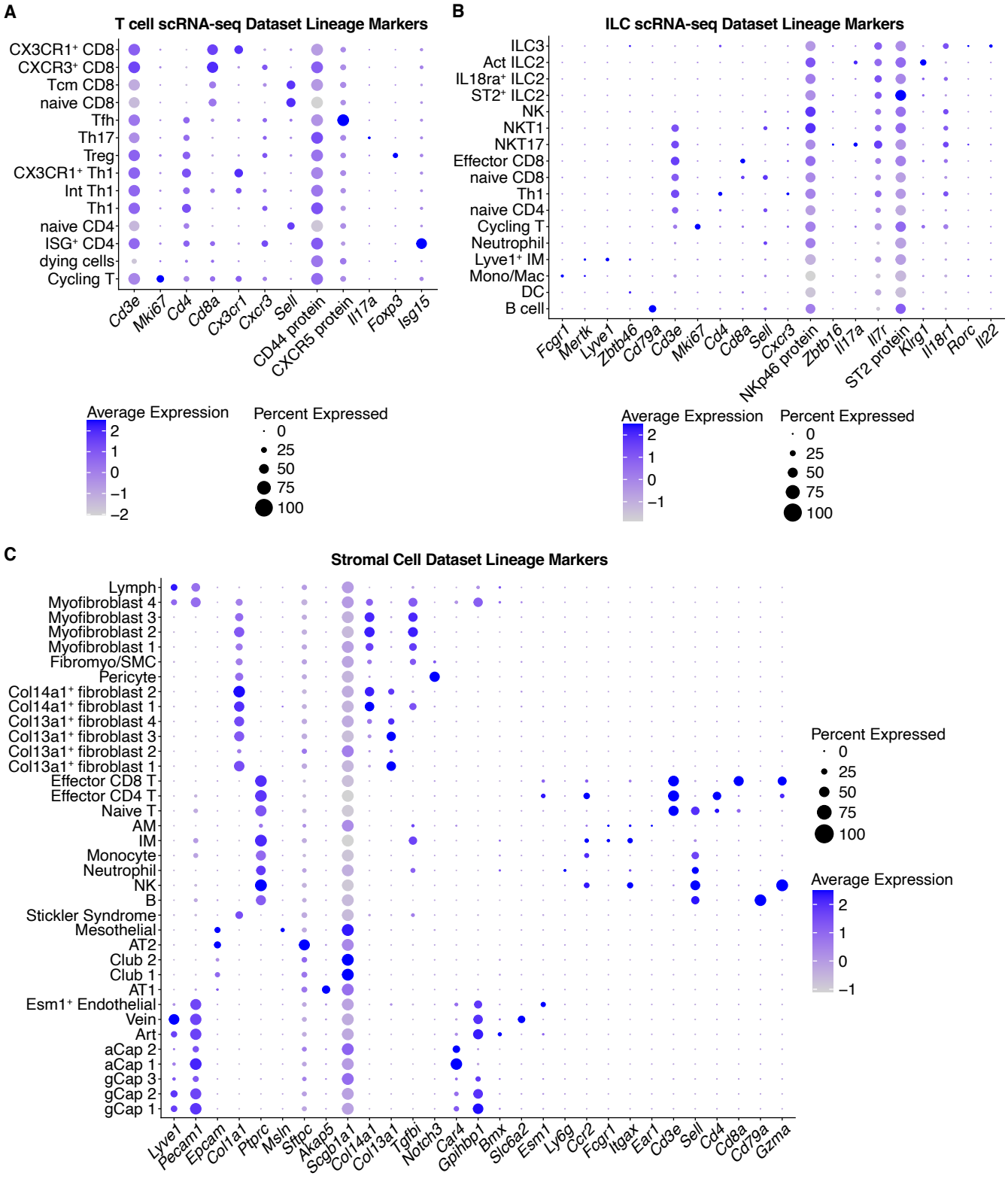

Supplementary Figure 8.

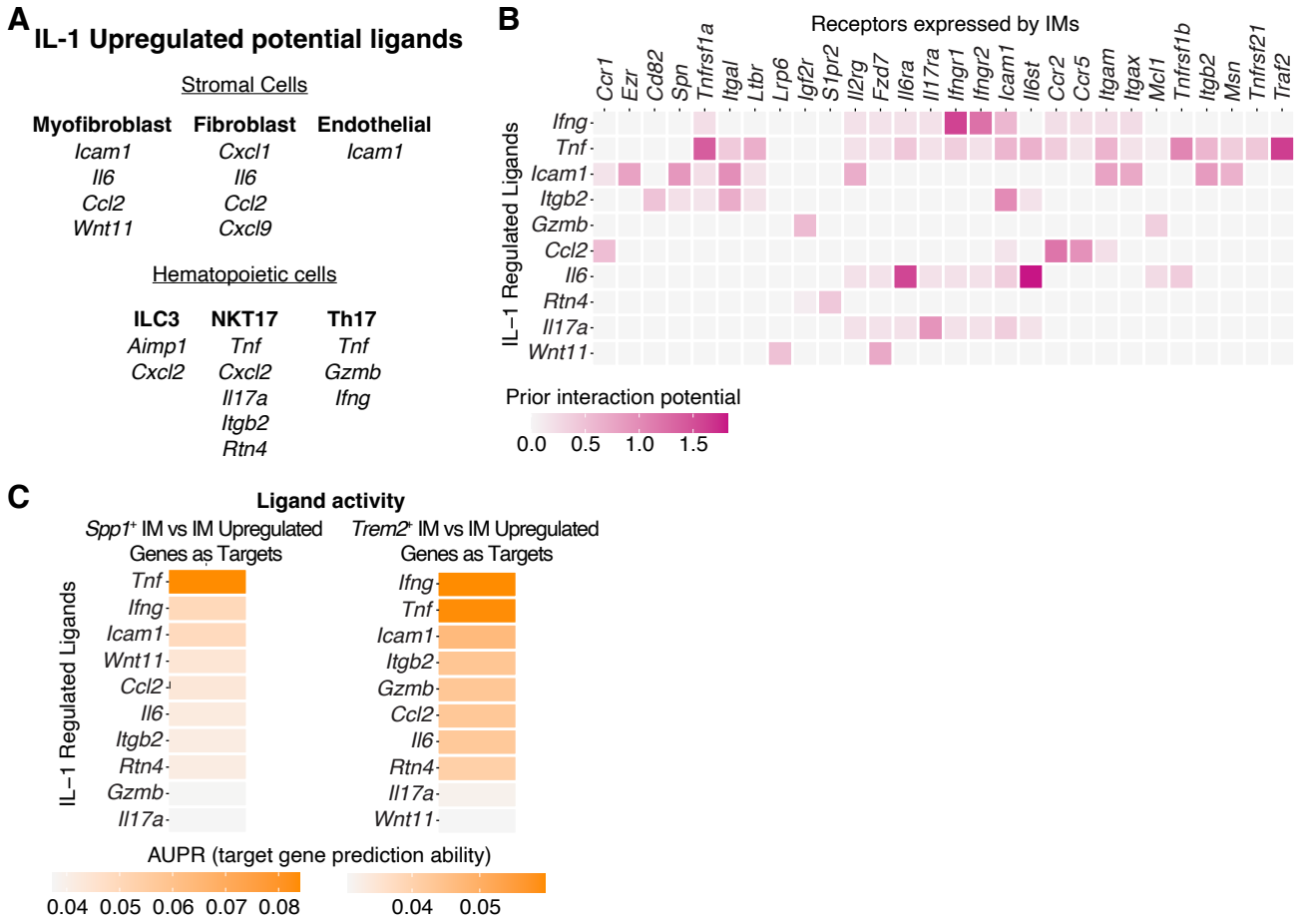

Supplementary Figure 9.